

ALMA MATER STUDIORUM - UNIVERSITÀ DI BOLOGNA

ENGINEERING AND ARCHITECTURE

*DEPARTMENT OF CIVIL, CHEMICAL, ENVIRONMENTAL AND MATERIALS
ENGINEERING*

EARTH RESOURCES ENGINEERING

MASTER THESIS

in

ENGINEERING GEOLOGY

**Detection of water seepage in river embankments: a case study along the Secchia
River (Modena, Italy)**

CANDIDATE
Federico Orcali

SUPERVISOR:
Prof. Lisa Borgatti

CO-SUPERVISOR
Gabriele Bitelli
Emanuele Mandanici
Davide Martinucci
Federica Pellegrini
Roberta Zambrini

Academic year 2017/2018
Session III

Contents

CONTENTS	I
LIST OF FIGURES	III
LIST OF TABLES	VI
ABBREVIATION	VII
SOMMARIO	VIII
ABSTRACT	IX
1. INTRODUCTION AND OBJECTIVE	1
1.1. INTRODUCTION	1
1.2. OBJECTIVE.....	2
2. GENERAL CHARACTERISTICS OF THE SECCHIA BASIN	3
2.1. GEOMORPHOLOGICAL DESCRIPTION OF THE PO PLAIN	3
2.2. HISTORICAL PROFILE OF THE RIGHT TRIBUTARIES OF THE PO RIVER	4
2.3. HYDROLOGICAL AND HYDROGEOLOGICAL FEATURES OF THE SECCHIA RIVER.....	9
2.4. GEOMORPHOLOGICAL FEATURES OF THE PROVINCE OF MODENA AND OVERVIEW OF THE SECCHIA RIVER	11
3. LEVEES: ROLE, COMPONENTS AND MECHANISMS OF FAILURE	16
4. CHARACTERISTICS AND PROBLEMS OF THE STUDIED EMBANKMENT	19
4.1. MORPHOLOGY OF THE AREA	19
4.2. WATER PIPING DURING 2014	20
4.3. GEOGNOSTIC INVESTIGATIONS	21
4.4. WATERPROOFING INTERVENTION	25
5. EXPERIMENTAL MONITORING PROJECT	27
5.1. OBJECTIVE OF THE PROJECT	27
5.2. ARCHITECTURE OF THE PROJECT	27
5.3. UPSTREAM SECTION	29
5.4. MEDIAN SECTION	30
5.5. DOWNSTREAM SECTION.....	31
6. ANALYSIS OF THE PIEZOMETRIC DATA	35
6.1. 2017 DATA	36
6.2. 2018 DATA	38
6.3. GEOLOGICAL CROSS SECTIONS.....	39
7. MULTISPECTRAL SURVEY	43
7.1. INTRODUCTION TO REMOTE SENSING TECHNOLOGY.....	43
7.2. INTERACTIONS BETWEEN OBJECTS AND ELECTROMAGNETIC ENERGY.....	44
7.3. MULTISPECTRAL TECHNOLOGY	46

7.4.	DESCRIPTION OF THE SURVEYS AND METHODOLOGY USED	47
8.	PHOTOGRAMMETRIC RECONSTRUCTION OF THE SURVEY.....	50
8.1.	INTRODUCTION TO PHOTOGRAMMETRY	50
8.2.	ORIENTATION OF THE PHOTOGRAPH	51
8.3.	AERIAL TRIANGULATION	53
8.4.	PHOTOGRAMMETRIC RESTITUTION OF THE SURVEYS	53
8.4.1.	<i>Import and alignment of the photos.....</i>	<i>53</i>
8.4.2.	<i>Dense Cloud</i>	<i>56</i>
8.4.3.	<i>Mesh and Texture.....</i>	<i>57</i>
8.4.4.	<i>DEM and Orthophoto.....</i>	<i>58</i>
8.4.5.	<i>Results of the photogrammetric models.....</i>	<i>59</i>
9.	REVIEW ON THE SPECTRAL INDEXES USED	64
9.1.	NORMALIZED DIFFERENCE VEGETATION INDEX	65
9.2.	NORMALIZED DIFFERENCE VEGETATION INDEX WITH RED EDGE	65
9.3.	MODIFIED SIMPLE RATION AND MODIFIED SIMPLE RATIO WITH RED EDGE.....	66
9.4.	GREEN DIFFERENCE INDEX	67
9.5.	GREEN AND RED-EDGE CHLOROPHYLL INDEX	67
9.6.	NORMALIZED DIFFERENCE WATER INDEX	68
9.7.	SOIL ADJUSTED VEGETATION INDEX	69
10.	RESULTS OF THE SPECTRAL INDEXES.....	71
10.1.	ANALYSIS OF THE SPRING SEASON CONDITIONS: MAY 2017 COMPARED WITH APRIL 2018	92
11.	NDVI FROM SATELLITE SENTINEL-2	94
11.1.	OVERVIEW OF THE SENTINEL-2 SATELLITE	94
11.2.	NDVI MAPS OF THE EXTENDED AREA	95
11.3.	RESULTS AND ANALYSIS OF THE SATELLITE MAPS.....	99
12.	DISCUSSION	100
13.	CONCLUSIONS.....	103
	BIBLIOGRAPHY	105
	SITOGRAPHY.....	109

List of Figures

Figure 1.1. Linear trends for different worldwide natural catastrophehy. 1980-2016.Source: Easac.	1
Figure 2.1. Tectonic scheme of the southern Po plain.....	4
Figure 2.2. Excerpt of geomorphologic map of the Secchia river, taken from AiPo's GeoPortale.....	6
Figure 2.3. Ancient riverbeds chart of the rivers Po, Panaro, Reno and Secchia. Legend: 1) ancient riverbeds active before the VII century a.D.; 2) ancient riverbeds active between the VIII and the XII centuries a.D.; 3) ancient riverbeds active between the XII century a.D. and the XV century a.D.; 4) ancient riverbeds active after XVcentury a.D.; 5) main fluvial deviations with age indication; 6) main fluvial cut with age indications; 7) Panaro and Reno River alluvial fans; 8) Apennine hills formations. ..	7
Figure 2.4. Geology and geomorphology of the studied area. It is highlighted the part of the embankment with seepage problems and the ancient riverbed (yellow triangles) detaching from it. Source: Engeo Technical report.	8
Figure 2.5. Excerpt from the idro-stratigraphic Section n.26. Source: website of Servizio geologico, Sismico e dei Suoli of the Emilia-Romagna Region.....	11
Figure 2.6. Type of soils.....	14
Figure 2.7. Secchia river and its tributaries.	15
Figure 3.1. Components of a levee.....	16
Figure 3.2. Main failure modes. Source: Schierek (1998), TAW report.	18
Figure 3.3. Breach of the right levee of the Secchia river, San Matteo (MO). Image from Protezione Civile Modena - Aeroclub Marzaglia.....	18
Figure 4.1. Geographical position of the studied area. The red line indicates the cross section of the following figure.	19
Figure 4.2. Cross section of the levee of the Secchia river in Via Bozzala (MO). Measures in meters and m a.s.l. for the height, from the DSM of the area.	20
Figure 4.3. Hydrometric levels of Ponte Bacchello from 20/12/2013 to 20/03/2014.....	20
Figure 4.4. Concentrated seepage near the civic 10 of Bozzala street.....	21
Figure 4.5. Embankment made of sandbags, made in date 08/02/2014.	21
Figure 4.6. Geognostic tests performed along the embankment.....	22
Figure 4.7. Lithological and hydrogeological section A-A' (longitudinal section). Scale factor 1:2'000.	23
Figure 4.8. Lithological and hydrogeological section B-B' (cross-section). Scale factor 1:200.....	24
Figure 4.9. Planimetry of the sheet pile. In yellow the concrete mantle, in pink the sheet piles, in orange the crown of the embankment.....	25
Figure 4.10. Sheet piles and embankment cross-section.	26
Figure 5.1. Installation scheme of the humidity sensors.	28
Figure 5.2. Installation scheme of the multiparametric chain.....	29
Figure 5.3. Installation scheme of the upstream section.	30

Figure 5.4. Installation scheme of the median section.	31
Figure 5.5. Installation scheme for the downstream section – multiparametric chain INP1 and Casagrande piezometer P4.	32
Figure 5.6. Installation scheme for the downstream section – humidity sensors U1a, U1b, U1c.	33
Figure 5.7. Disposition of the three sections of the monitoring network.	34
Figure 6.1. Hydrometric level and piezometric level from 03/2017 to 07/2017.	37
Figure 6.2. Hydrometric levels of Ponte Motta and Ponte Bacchello.	37
Figure 6.3. Hydrometric and piezometric levels from December 2017 to June 2018.	39
Figure 6.4. Map of the area with the three cross sections in red.	40
Figure 6.5. Upstream cross section.	40
Figure 6.6. Median cross section.	41
Figure 6.7. Piezometric and hydrometric height variations during a flood event.	41
Figure 6.8. Downstream cross section.	42
Figure 7.1. Description of an electromagnetic wave. Where E is the sinusoidal electric wave, and M is the magnetic wave. Both are normal to the direction of propagation.	43
Figure 7.2. Electromagnetic spectrum.	44
Figure 7.3. Typologies of reflection.	45
Figure 7.4. Average reflectance spectrum of three different objects with different spectral characteristics: dry bare soil, green vegetation and clear water. Source: Lillesand et al. (1994).	46
Figure 7.5. Acquisition bands of three different passive remote sensing technologies.	47
Figure 7.6. Specifics on the spectral bands detected by the MicaSense RedEdge™ 3 camera.	48
Figure 7.7. Representation of the RPV's flight plan.	49
Figure 8.1. Geometry of a stereoscopic model in aerial photogrammetry.	50
Figure 8.2. Interior orientation of a camera.	52
Figure 8.3. Example of valid (blue line) and invalid (red line) match points in two different images.	54
Figure 8.4. The GCP (T121) is manually moved to the center of the panel where the coordinates of the GCP were taken.	55
Figure 8.5. Workspace from Photoscan Professional Pro representing the sparse cloud of point with GCP.	55
Figure 8.6. Workspace from Photoscan Professional Pro representing the dense cloud of point with GCPs.	56
Figure 8.7. Workspace from Photoscan Professional Pro representing a part of the polygonal mesh with GCPs.	57
Figure 8.8. Workspace from Photoscan Professional Pro representing a part of the textured polygonal mesh with GCP.	57
Figure 8.9. Orthophoto of the 26/05/2017 survey, with GCPs.	58
Figure 8.10. Digital Elevation Model of the 26/05/2017 survey, in Ellipsoidal height. With GCPs.	58

Figure 9.1. Spectrum of reflectance of a fresh soy leaf (Hosgood et al. 1995), with red-edge zone highlighted in red.....	66
Figure 9.2. Scatter plots indicating the relationship between various reflectance indices and total chlorophyll content. Source: Gitelson et al. (2003).....	68
Figure 10.1. Map of the survey in the visible spectrum, with geognostic interventions and piezometers position.	72
Figure 10.2. Map of the surveyed area along with the ancient riverbed mask (in violet).....	72
Figure 10.3. Maps and histograms of the four surveys expressed with CI.....	73
Figure 10.4. Maps and histograms of the four surveys expressed with CI, ancient riverbed.....	74
Figure 10.5. Maps and histograms of the four surveys expressed with CI-RE.	75
Figure 10.6. Maps and histograms of the four surveys expressed with CI-RE, ancient riverbed.	76
Figure 10.7. Maps and histograms of the four surveys expressed with GDI. Values in W/m^2	77
Figure 10.8. Maps and histograms of the four surveys expressed with GDI, ancient-riverbed. Values in W/m^2	78
Figure 10.9. Maps and histograms of the four surveys expressed with MSR.....	79
Figure 10.10. Maps and histograms of the four surveys expressed with MSR, ancient riverbed.	80
Figure 10.11. Maps and histograms of the four surveys expressed with MSR-RE.....	81
Figure 10.12. Maps and histograms of the four surveys expressed with MSR-RE, ancient riverbed.	82
Figure 10.13. Maps and histograms of the four surveys expressed with NDVI.	83
Figure 10.14. Maps and histograms of the four surveys expressed with NDVI, ancient riverbed.....	84
Figure 10.15. Maps and histograms of the four surveys expressed with NDVI-RE.....	85
Figure 10.16. Maps and histograms of the four surveys expressed with NDVI-RE, ancient riverbed.	86
.....	
Figure 10.17. Maps and histograms of the four surveys expressed with NDWI.....	87
Figure 10.18. Maps and histograms of the four surveys expressed with NDWI, ancient riverbed....	88
Figure 10.19. Detail of the GDI map of April 2018. Values in W/m^2	90
Figure 10.20. Excerpt from the NDVI-RE map of April 2018.....	91
Figure 10.21. Complete NDVI map of the multispectral survey of April 2018.....	93
Figure 10.22. Superposition of NDVI values above 0.65 of the maps of May 2017 (blues) and April 2018 (greens).....	93
Figure 11.1. Characteristics of the spectral bands acquired by Sentinel-2.....	94
Figure 11.2. Mean NDVI trend from satellite images.....	96
Figure 11.3. NDVI maps and histograms of the Sentinel-2 satellite images.....	98
Figure 12.1. Linear correlation graphs between NDVI values and piezometric levels.....	102

List of Tables

Table 1. Average camera location error. X – Longitude, Y – Latitude, Z – Altitude.....	59
Table 2. Survey of 26/05/2017. Ground control points mean root square error*. X – Longitude, Y – Latitude, Z – Altitude.....	59
Table 3. Features of the reconstruction parameters of the survey of 26/05/2017.....	60
Table 4. Survey of 18/07/2017. Ground control points mean root square error. X – Longitude, Y – Latitude, Z – Altitude.....	60
Table 5. Features of the reconstruction parameters of the survey of 18/07/2017.....	60
Table 6. Survey of 19/07/2017. Ground control points mean root square error. X – Longitude, Y – Latitude, Z – Altitude.....	61
Table 7. Features of the reconstruction parameters of the survey of 19/07/2017.....	61
Table 8. Survey of 06/04/2018. Ground control points mean root square error. X – Longitude, Y – Latitude, Z – Altitude.....	62
Table 9. Features of the reconstruction parameters of the survey of 06/04/2018.....	62
Table 10. Definition and sources of the VIs used.....	64
Table 11. Mean values of the spectral maps.....	91
Table 12. Mean NDVI values of each month, calculated from the year 2017 to 2019.....	95
Table 13. Mean piezometric and hydrometric levels over two weeks.....	100
Table 14. Weighted NDVI average.....	100

Abbreviation

AIPo	Agenzia Interregionale per il fiume Po
Chl	Chlorophyll
CI	Chlorophyll Index
CPTU	Piezometric Cone Penetration Test
EASAC	European Academies' Science Advisory Council
GCP	Ground Control Point
GDI	Green Difference Index
GIS	Geographic Information System
GSM	Global System for Mobile communications
IGM	Istituto Geografico Militare
IR	Infrared
LWIR	Long Wave Infrared
MIR	Mid-infrared Spectroscopy
MSI	Multispectral Image
MSRI	Modified Simple Ratio Index
NDVI	Normalized Difference Vegetation Index
NDWI	Normalized Difference Water Index
NRTK	Network Real Time Kinematic
RE	Red Edge
RGB	Red Green Blu
RMSE	Root Mean Square Error
RPV	Remotely Piloted Vehicle
RTK	Real Time Kinematic
RVI	Ratio Vegetation Index
SAVI	Soil Adjusted Vegetation Index
SWIR	Short Wave Infrared
UTM	Universal Transverse Mercator
VI	Vegetation Index
WGS	World Geodetic System
WSN	Wireless Sensor Network

Sommario

La tecnologia multispettrale viene ampiamente utilizzata da diversi decenni nella mappatura di zone con scarsa vigoria vegetativa. In particolare vengono valutate porzioni di coltivazioni più secche di quelle circostanti, e quindi con una minore rendita economica. Oppure aree estese in crisi idrica che possono rappresentare un pericolo, a causa di possibili incendi (Gong et al., 2006).

Questa tesi nasce con l'intento di utilizzare questa stessa tecnologia, ma con lo scopo opposto: analizzare aree con una vigoria vegetativa maggiore, la quale può essere indicativa di disponibilità di acque sotterranee relativamente più elevata come conseguenza di fenomeni di filtrazioni. Il problema delle filtrazioni d'acqua in contesti naturali e costruiti è stato analizzato con diverse tecnologie, tecniche radar, geofoni, georadar, specialmente per determinare filtrazioni da tubature d'acqua.

Ad esempio, Hadjimitsis et al. (2013) hanno studiato il problema delle filtrazioni d'acqua da tubature, sia attraverso la tecnologia iperspettrale, montata su pallone aerostatico, che quella multispettrale presente sui satelliti, e quindi con una bassa risoluzione, ottenendo risultati interessanti.

In questo lavoro, invece, ci si propone di analizzare i fenomeni di filtrazione al di sotto o attraverso un corpo arginale, la cui causa dipende presumibilmente dalla presenza di un paleoalveo, che funge da via preferenziale per l'acqua quando il livello idrometrico cresce a seguito di eventi di piena.

Lo studio viene affrontato da tre prospettive diverse: analisi di dati di pressione interstiziale dei pori lungo il tratto arginale registrata da piezometri installati in diverse posizioni ed a differenti profondità, analisi di dati multispettrali di precisione acquisiti durante tre indagini (maggio e luglio 2017, aprile 2018) e di immagini multispettrali da satellite tramite indici vegetativi.

I dati vengono quindi esaminati congiuntamente per ottenere una visione completa del fenomeno e per cercare correlazioni tra di essi. In particolare, è stata trovata una relazione tra zone con alti valori di indici vegetativi, tipici di una vegetazione vigorosa, e dunque di porzioni di suolo con maggiore contenuto idrico, con le pressioni interstiziali misurate dai piezometri a seguito di eventi di piena del fiume adiacente all'area in esame.

Abstract

Multispectral technology has been widely used for several decades in the mapping of areas with low vegetative vigor. In particular, the purpose is to detect drier crop areas which will have a lower economic yield, or to identify extended areas in water crisis that can be hazardous due to possible fires (Gong et al., 2006).

This thesis is born with the intent to use this same technology, but with the opposite purpose: to analyze areas with a higher vegetative vigor, which can be indicative of the availability of higher groundwater content as a consequence of seepage phenomena. The problem of water seepage in natural and constructed contexts has been analyzed with different technologies, radar techniques, geophones, georadar, especially to determine seepages from water pipes.

For example, Hadjimitsis et al. (2013) studied the problem of water seepage from pipes, both through hyperspectral technology, mounted on an aerostatic balloon, and the multispectral one present on satellites, and therefore with a low resolution, obtaining interesting results.

In this work, instead, we propose to analyze the seepage phenomena below or through a levee, whose cause presumably depends on the presence of an ancient riverbed, which acts as a preferential path for water when the hydrometric level rises as consequence of flood events.

The study is tackled by three different perspectives: analysis of pore pressure data along the embankment measured by piezometers in different positions and installed at different depths, analysis of multispectral precision data acquired during three surveys (May and July 2017, April 2018) and multispectral satellite images through Vegetation Indexes (VIs).

The data are then examined jointly to obtain a complete view of the phenomenon and to find correlations between them. In particular, a relationship was found between areas with high values of vegetative indices, typical of vigorous vegetation, and therefore of portions of soil with higher moisture content, with the interstitial pressures measured by piezometers following flood events.

1. Introduction and Objective

1.1. Introduction

In the last decades, the increase of severe flood events has become a worldwide issue that must be face up to. A report of the EASAC (European Academies' Science Advisory Council) of the 2013, confirmed by its update of the 2018, showed up that flood events increased by the 300-400% from the 1980, as stated in [Figure 1.1](#). Floods and the other events related to the climate change have a severe impact of society, both in economic and social terms. This means that the society must adapt to this climate variability.

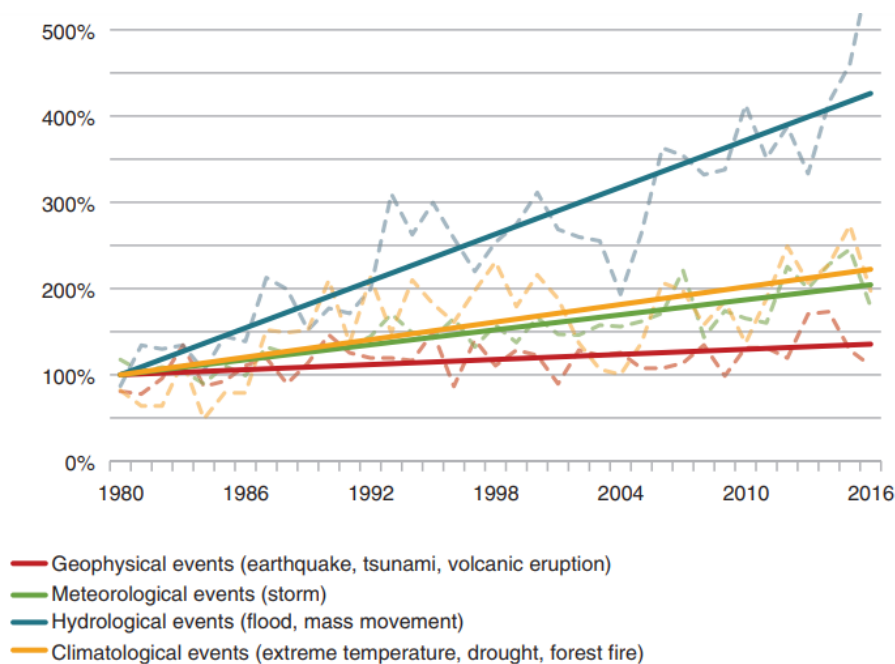


Figure 1.1. Linear trends for different worldwide natural catastrophes. 1980-2016. Source: Easac¹.

An important step of this adaptation should be the monitoring of the critical areas in the territory. This study in fact focuses on a possible monitoring procedure tested over the levee system of the Secchia river, which experienced a breach in the 2014 in San Matteo (MO), and in particular over a trait of a levee that has had water seepage issues. This monitoring procedure should consist in a periodical survey over the levees with a drone equipped with a multispectral camera, to detect area with possible seepage problems. Once detected the areas of interest, more detailed surveys should be performed and in situ monitoring system should be deployed. The traditional way of inspection consists in the direct visual examination of the levee by some designed officer, ideally on foot, who evaluates the quality of the grass cover, the presence of dead vegetation or absence of it, that could be related to erosion, seepage or animal

¹ EASAC (2018). Trends in extreme weather events in Europe. Preparing for climate change adaptation: an update on EASAC's 2013 study.

burrows for example. This method requires a lot of time, thus the new approach proposed here would save personnel and time, that could be allocated to solve or monitor other problems.

Together with the monitoring of the territory, this methodology could be adopted for the inspection of possible water leakages in water pipes (Hadjimitsis et al 2013).

1.2. *Objective*

The data used in this study are part of a program carried out by AIPo (Agenzia Interregionale per il Fiume Po) in collaboration with Esplora, which consists in finding effective and time saving methods for the detection of problems in the embankments of the rivers included in the Po basin.

Initially the multispectral survey was tested in different sectors of the embankments to detect possible animal burrows, which have been found to be the cause of the collapse of the embankment of the Secchia river at San Matteo (MO) in 2014 (D'Alpaos et al., 2014). The burrows should be identifiable by a “hole” in the Vegetation Indexes (VIs), caused by the animals (badger, porcupine and fox mainly) which remove the grass cover.

This study, thus, using the multispectral surveys already available and integrating them with the data obtained by the piezometers and with the raw data from the satellite Sentinel 2, is aimed at:

- Analyzing the multispectral images (MSIs) with different Vegetation Indexes (VIs) to detect areas with a higher vegetative vigor, as proxy of seepage path;
- Analyzing the data from the piezometers installed along the embankment to understand the groundwater flow during flood events and during stable or low flow periods;
- Search for a possible correlation between the increase of pore water pressure values in the piezometers and the values of the VIs.

2. General characteristics of the Secchia basin

In this section, the geological, geomorphological and hydrological features of the studied area will be described, with a preliminary part focusing on the Po plain in general, on the history of the riverbeds and finally describing the province of Modena and in particular the area where the studied embankment is located.

2.1. *Geomorphological description of the Po plain*

The area considered belongs to the Apennine sector of the Po Valley. There, outcrop Holocene alluvial deposits with granulometry varying from clay to sands and deposits of the rivers Reno, Panaro and Secchia.

The area in question ([Figure 2.1](#)) falls to the center of the area characterized by the "Ferrara folds", that have affected both the distribution of deeper deposits and the hydrographic evolution in this area of the Po Valley.

As it is known, the Ferrara folds are constituted by a series of fault folds which created a positive structure strongly raised in relation to the surrounding area. The Ferrara folds represent the continuation of the Apennine structures in the area of the Po plain. The thickness of the Plio-Quaternary marine deposits is very varied, being naturally conditioned by the geometry of the aforesaid structures. In particular, concerning the area under examination, their thickness has a depocenter in the area of San Giovanni in Persiceto (8500 m) in correspondence with the axial sector of the Bologna - Bomporto - Reggio Emilia. Proceeding to the north, the thickness gradually decreases up to 5500 m of Cento.

Between Cento and S. Agostino, the Plio-Quaternary deposits are notably disturbed even by disjunctive and faulted structures; their thickness varies between 750 and 2500 m. In the area of S. Agostino, they reach locally a maximum thickness of 3500 m, which is reduced by proceeding towards the area of Finale Emilia (2500 m); beyond Finale Emilia there is once again a rather complex sector on whose axial culminations the power of the plio-quaternary sediments is reduced to only 250 m (Bondeno and Ferrara area).

Proceeding from the northern extremity of the pede-apenninic conoids up to the height of the Cento - Crevalcore alignment, the continental deposits reach here the maximum thickness (about 400 m), with brackish or lagoon episodes; this area falls in correspondence with the Bologna - Bomporto - Reggio Emilia syncline. In this sector, there are frequent sands of both Apennine and Alpine origin (the latter more frequent at greater depths). Between the aforementioned alignment and that of Finale Emilia - Vigarano Mainarda, we have in the first 50 m rows and clays with low permeable levels consisting exclusively of silty sands of Apennine origin; at higher depths, more powerful and more granulometric sand levels appear, due to the natural digging of the Po River.

To the north of the Finale Emilia - Vigarano Mainarda route one enters the lowland sector characterized almost exclusively by the Po floods, which constitute regular sedimentary bodies stretched in the W - E direction at least up to 100 m deep.

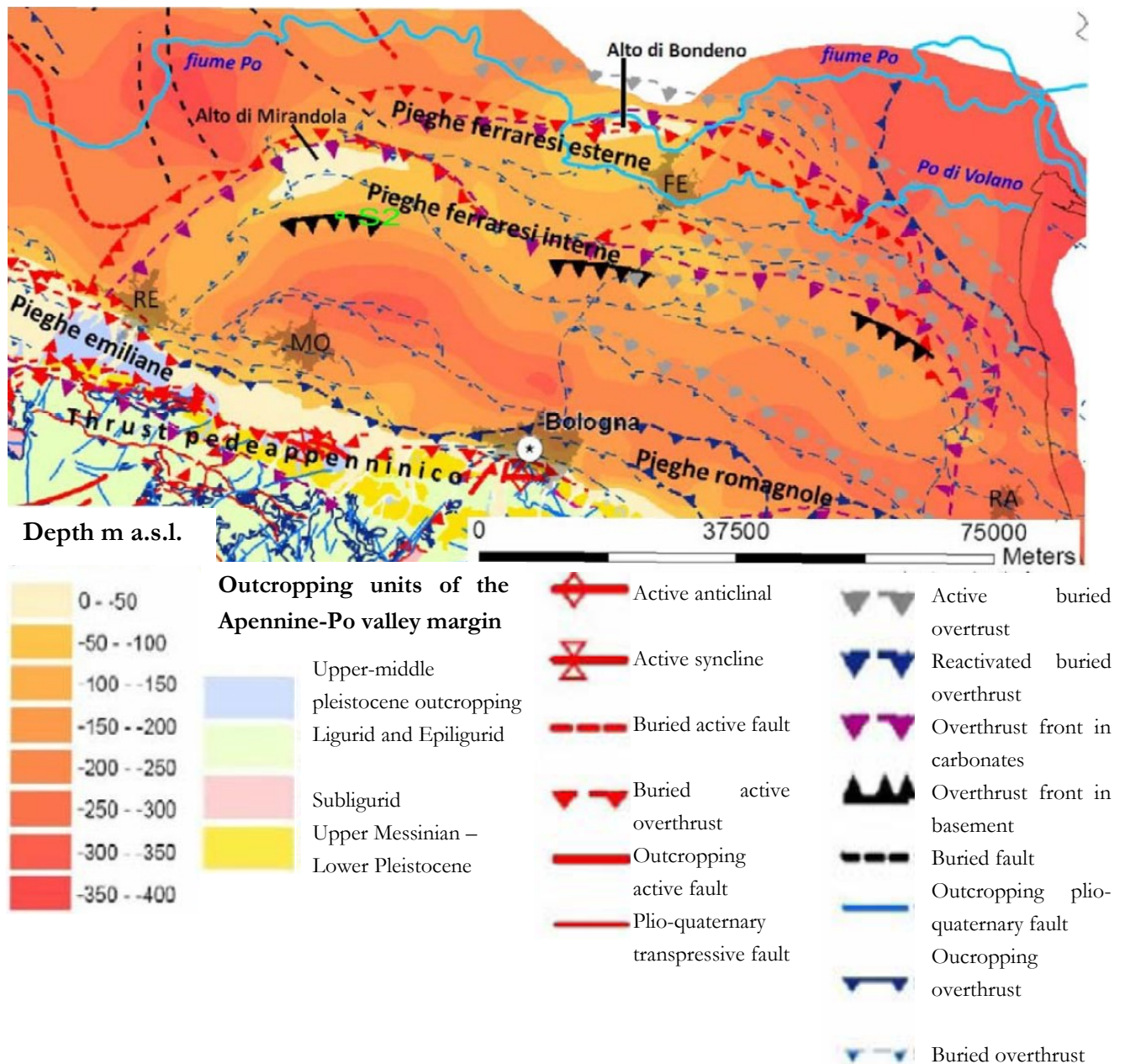


Figure 2.1. Tectonic scheme of the southern Po plain.

2.2. Historical profile of the right tributaries of the Po river

Near the Po river and south of it, the river system has developed according to the typical sedimentary model of an alluvial plain, which involves a selective sedimentation of material from the foothills to the outfall, with gradual decrease in grain size. The resulting morphological structure is that of a high plain sector consisting of mainly gravelly conoids and of a medium and low plain sector characterized by higher areas. It is characterized by sandy granulometries at present and extinct (ancient) riverbeds and by depressed interfluvial areas (valleys) with silt-clay texture.

Castaldini (1989) described that the disposition of the ancient riverbeds of the right tributaries of the Po, represented in Figure 2.3, shows that in the terminal stretch they travelled parallel to the Po for a

long part before flowing into it. Only the hydraulic regulation of the last three centuries has lost this feature.

In the Pleistocene, after the emergence of the Po Valley, the Po, east of Guastalla, developed along the line joining the current localities of Carpi, Nonantola and San Giovanni in Persiceto, which is a path much further south than it is today; this trend is documented by sediments of the Po, that can be found at depths greater than 100 m compared to the current campaign plan.

Around the first millennium b. C. the Po forked between Brescello and Guastalla or east of Casalmaggiore to give rise to a main branch (Po di Adria) and to one (Po di Spina) or more minor branches sub-parallel to it, along a strip limited to the south by the current localities of Poviglio, Concordia sulla Secchia, Bondeno and Ferrara. Traces of these more southern courses are represented, for example, by the buried meanders found south of San Martino Spino.

For what it concerns the Apennine tributaries, to the south of the Po it is possible to outline the following palaeographic picture ([Figure 2.3](#)). The river Secchia, from the Apennine margin, reached approximately in Cavezzo, with a more western route and sub-parallel than today's one, along the Rubiera-Carpi route which is characterized by an alignment of bumps.

Starting from Cavezzo, the Secchia took a west-east direction and, touching the current villages of San Felice sul Panaro, Finale Emilia, Casumaro and Vigaro Mainarda, entered the Po di Spina near Ferrara after receiving the waters of Panaro and of Reno.

The course of the Secchia in the VIII-IX century a. D. was impounded in the area of Cittanova and it came out more downstream with more courses that headed north. Downstream of Cavezzo, the Secchia retraced the Roman route. In this period, the Crostolo and Secchia streams converged, between Rolo and Mirandola, in a single paleo-river with outflow towards the east (corresponding to the current dowel of the Gavello), which ended in the Po near Bondeno. A little further south of this there is another longitudinal route, mainly made up of the Panaro and the Reno, but where also the paleo river of the Secchia converged. These ancient streams probably meet the Po near Ferrara.

The Secchia, which in the upstream stretch corresponded roughly to the current route, abandoned the riverbed of Cavezzo, moving northwest towards San Martino Spino and Bondeno ([Figure 2.2](#) and [Figure 2.4](#)). In this locality, it joined the Panaro, with which it headed north to merge into Po near Ficarolo. In the XIV-XV century a. D. the Secchia, at height of Concordia, turned north and before assuming today's structure, i.e. flowing into the Po to the west of Quingentole.

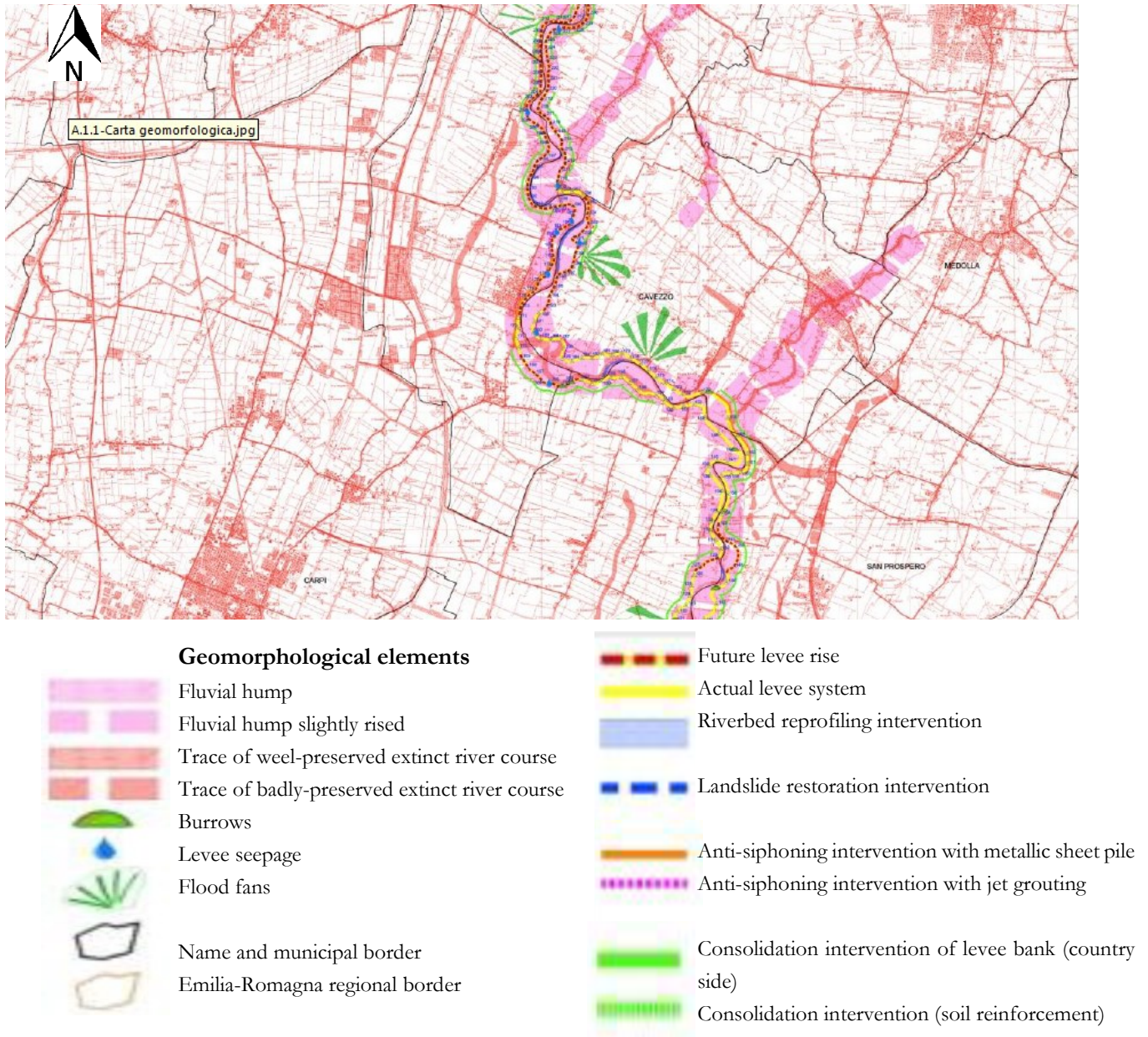


Figure 2.2. Excerpt of geomorphologic map of the Secchia river, taken from AiPo's GeoPortale.

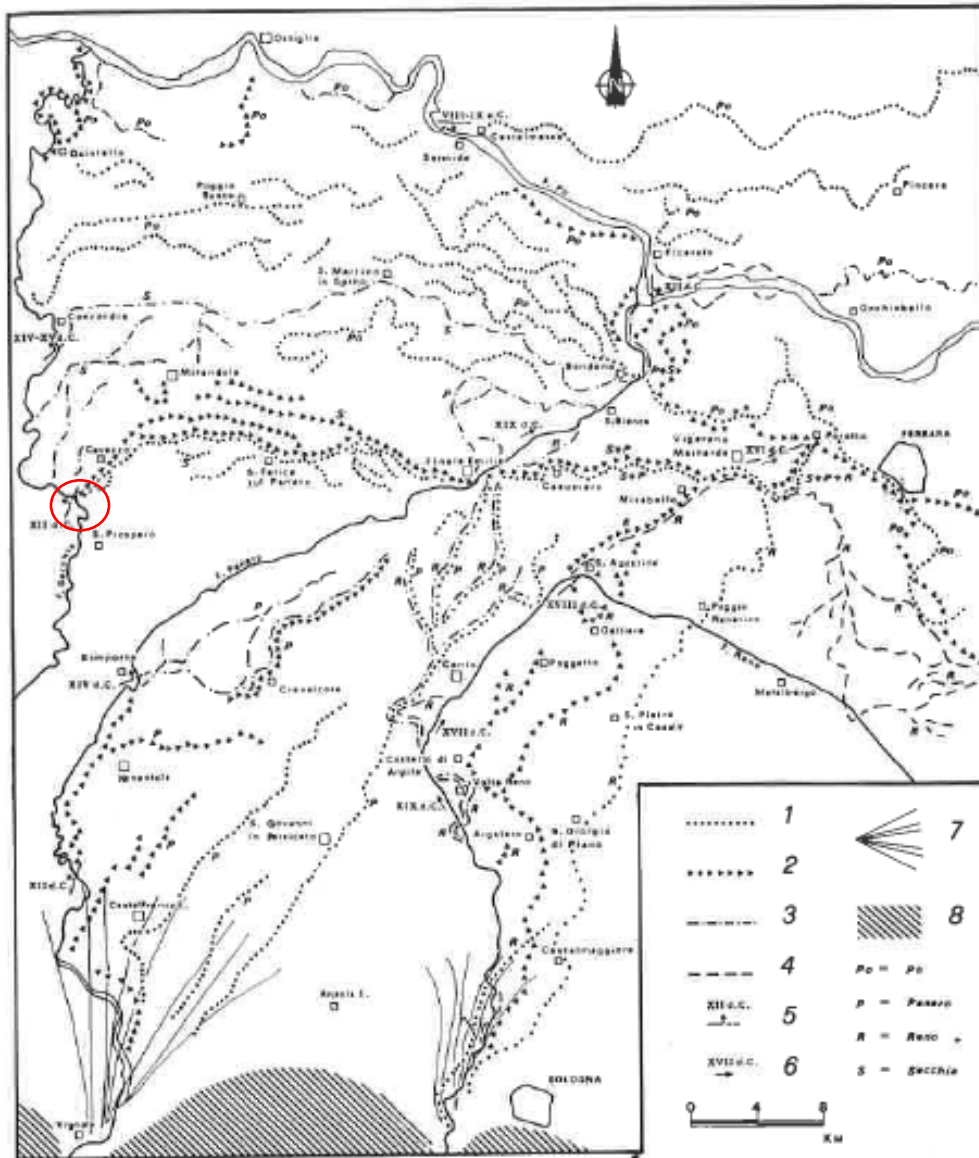
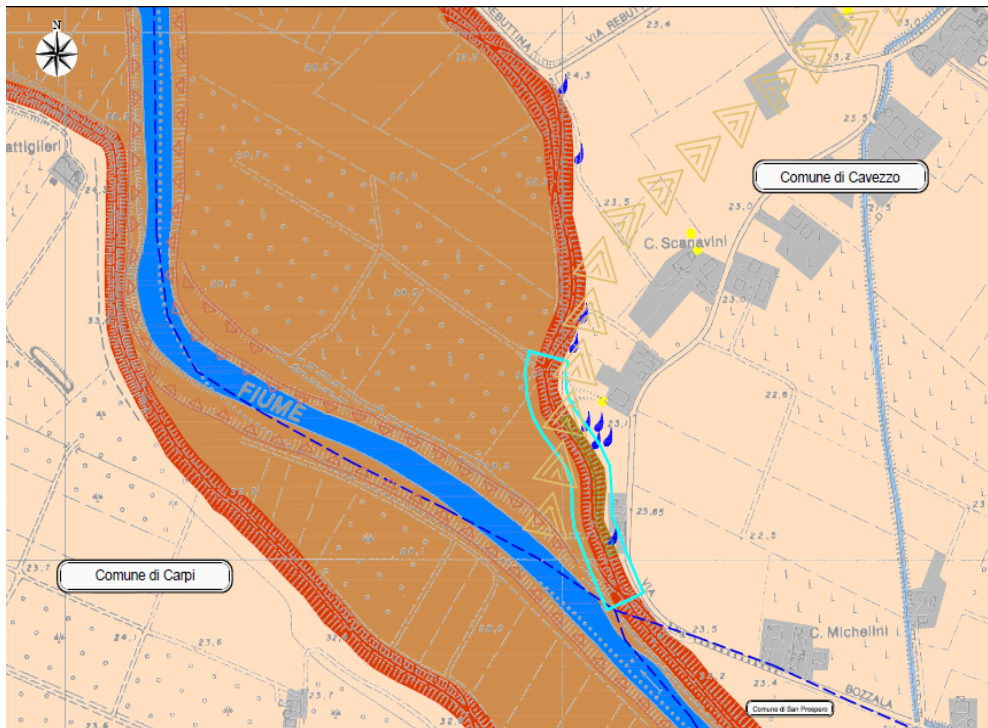


Figure 2.3. Ancient riverbeds chart of the rivers Po, Panaro, Reno and Secchia. Legend: 1) ancient riverbeds active before the VII century a.D.; 2) ancient riverbeds active between the VIII and the XII centuries a.D.; 3) ancient riverbeds active between the XII century a.D. and the XV century a.D.; 4) ancient riverbeds active after XV century a.D.; 5) main fluvial deviations with age indication; 6) main fluvial cut with age indications; 7) Panaro and Reno River alluvial fans; 8) Apennine hills formations².

² Castaldini, D., Raimondi, S. (1985). Geomorfologia dell'area di Pianura Padana compresa fra Cento, Finale Emilia e S. Agostino. Atti della Società dei Naturalisti e Matematici di Modena, 116: 147-176.



Legend

-  Study area
-  Municipal border
-  Urbanized area

Geology and geomorphology

-  Embankment and riverbed deposits inside the embankment consisting of sands, silts and clays in variable composition
-  Embankment and riverbed deposits outside the embankment consisting of sands, silts and clays in variable composition
-  Ancient riverbed trace from X-XII century
-  Fluvial erosion scarp
-  Master embankment of Secchia River
-  Levee subjected to gravitational movement
-  Minimum flow riverbed
-  Channel Canalino
-  Point where liquefaction was observed
-  Point characterized by significant past water seepage

Figure 2.4. Geology and geomorphology of the studied area. It is highlighted the part of the embankment with seepage problems and the ancient riverbed (yellow triangles) detaching from it. Source: Engeo Technical report³.

³ Engeo srl Studio Geologico ed Idrogeologico (2014). Fiume Secchia: Lavori urgenti per il miglioramento delle condizioni di stabilità del corpo arginale nei confronti di fenomeni di filtrazione – Geological and seismic report. AiPo.

2.3. *Hydrological and hydrogeological features of the Secchia river*

The aquifers of the territory under exam, being in the Emiliano-Romagnola part of the Padan Plain, are characterized by three Idro-stratigraphic Units, as represented in [Figure 2.5](#):

- Aquifer Group A, corresponding to the Upper Emilia-Romagna Synthem;
- Aquifer Group B, corresponding to the Lower Emilia-Romagna Synthem;
- Aquifer Group C, corresponding to the Marine Quaternary Super-Synthem.

These Units are separated by stratigraphic discontinuities, which have been caused by tectonic activities. Above the base of the hydro-stratigraphic limits, there are clayey-silty strata, tens of meters thick, with a tabular (planar and parallel) geometry; their extension is regional and it's interrupted only in those zone with a structural higher elevation. These strata act as permeability barriers (as aquitards or aquicludes) and make the three aquifer groups isolated hydraulically, therefore water flow remains confined within its unit, except for those areas there occurs the direct recharging of aquifers.

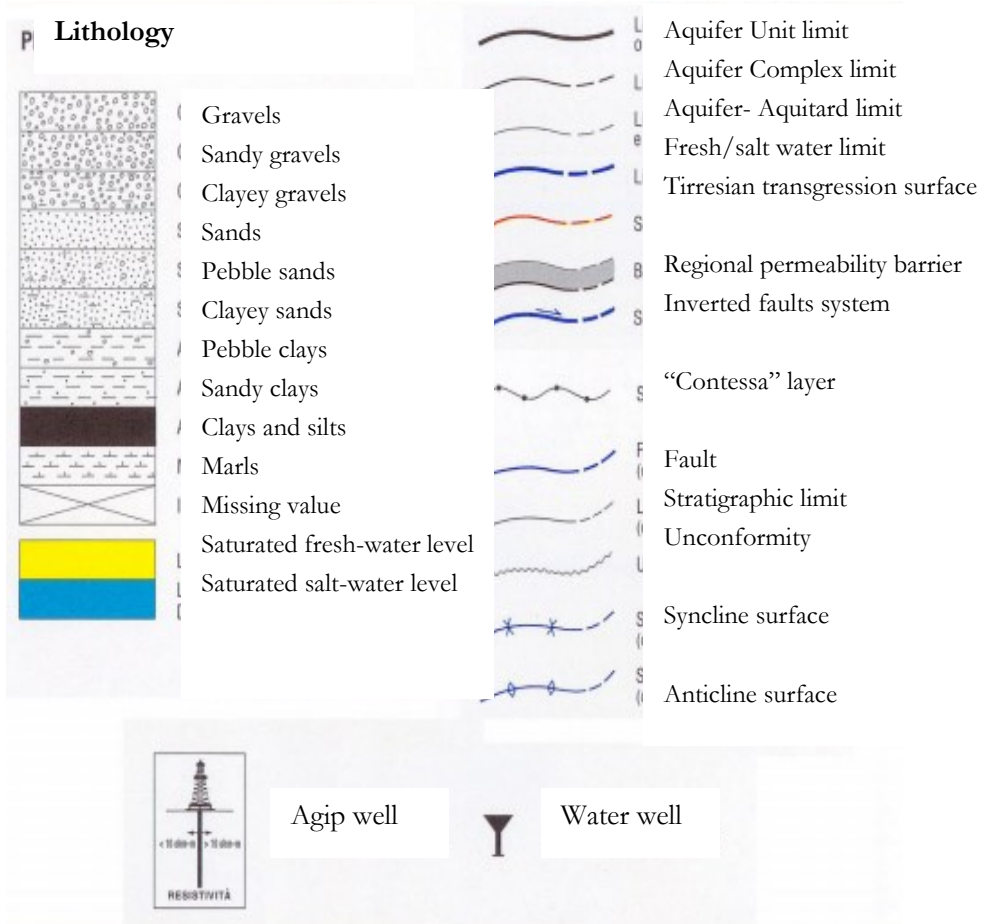
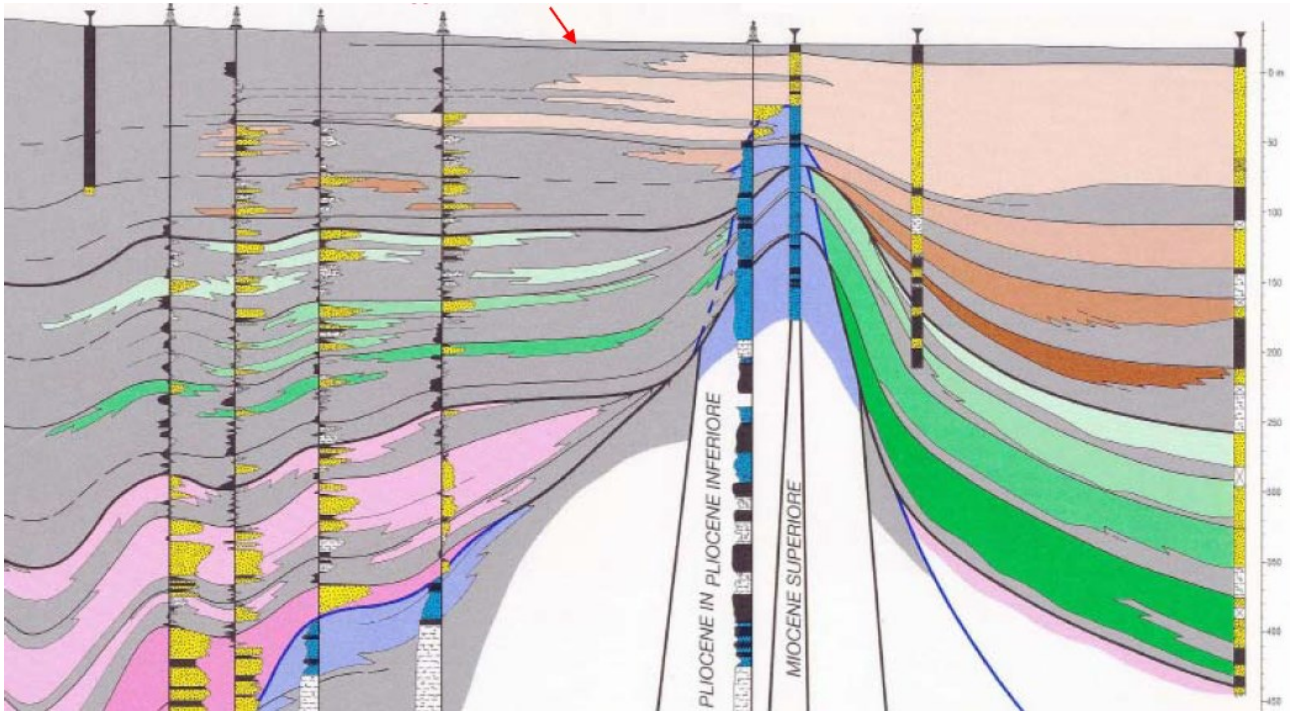
For what it concerns the hydro-stratigraphic reconstruction made by the Emilia-Romagna Region and Eni-Agip, in particular the section 26, depicted in [Figure 2.5](#), it's clear how the Ferrara folds caused a severe thinning of the Units; in fact, the base of the aquifer Unit A (in brown in [Figure 2.5](#)), where in the surrounding areas reaches 250 m of depth from the ground level, in correspondence of the axis of the Ferrara folds, its depth is around 70-80 m; likewise does the Unit B (in green in [Figure 2.5](#)), which stretches from a maximum depth of 450 m circa, to a minimum of 120-150 m of depth from the ground level.

In view of the above, it's clear that the subsoil of the area of interest consists mainly of fine deposits, with clayey or silty lithology, which are characterized by low permeability values. The aquifers are located in small lentiform formations, while in the surroundings areas the flow of water is extremely slow and implies very long times.

Groundwater generally remains near the ground level, and it is strongly influenced by local phenomena, such as the presence of surface water (e.g. the Secchia river), by emungations and by the permeability of the overlying land.

The seasonal excursions of the water level can be large: in particular, during the seasons characterized by intense rainy events, the height of the water table can rise in a very short time, until it touches the countryside level. For reservoirs near watercourses, similar phenomena are observed when the water level rises within the riverbed.

AREA UNDER STUDY



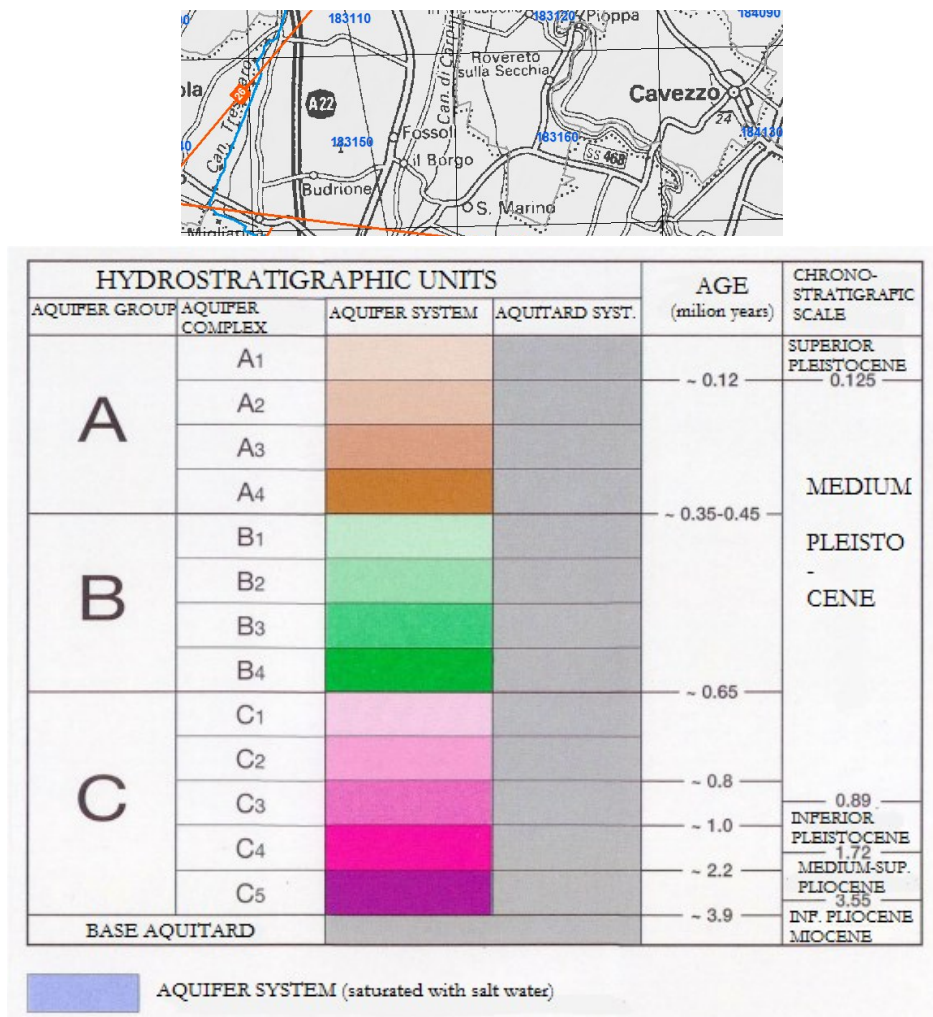


Figure 2.5. Excerpt from the idro-stratigraphic Section n.26. Source: website of Servizio geologico, Sismico e dei Suoli of the Emilia-Romagna Region.

2.4. Geomorphological features of the province of Modena and overview of the Secchia river

The province of Modena extends from the Po plain, with a lowest height of 10-12 m a.s.l., downward towards the northern Apennine chain, with a SW-NE direction. Its highest altitude is the Mount Cimone (2165 m). Therefore, Modena is characterized by various morphological characteristics, from the mountain environment, to hills (700-900 m) and reaching the lowlands of the right Po plain.

The area is crossed by different streams, which roughly follows the direction SSW-NNE; the major ones are the rivers Secchia and Panaro, both right tributaries of the Po river.

Concerning the geology of the area, it is widely heterogeneous, because of the tectonic stresses that caused the formation of the Apennines. Starting from the source of the streams (i.e. top of the Apennine chain), the outcropping formations are those of the Tuscan units, which consist mainly in sandstones from medium to coarse texture, moderately pervious, and marly-silty formations. These gave rise to morainic and detrital covers, with high permeability. The middle part of the Modena's Apennines is characterized by the outcropping of the Ligurian Units, made of clay and shaly-clay, which are overlaid by sedimentary flysches of the early Cretaceous-middle Eocene, made of marly-limestones, which have

very low permeability. Over these rocks, are found formations that belong to the Epiligurian Units, which were deposited at the end of the Apennines orogeny; they are mainly made of marls and calcareous sandstones, formed from the Eocene to the Miocene; they are characterized by a high permeability, caused by a high secondary porosity. In the hilly area, the marine sequence of the Apennine margin outcrops, which is constituted of sands and clays in the lower part, formed during the Pliocene, and of conglomerates of clay in the upper part, formed between the Pliocene and the Pleistocene. Finally, in the plain part and especially along the main water courses, deposits of gravel and sands are found, which are the alluvial fans created by the rivers Secchia and Panaro and other smaller streams.

At first glance, the general slope trend of the territory, if artificial modifications are excluded, appears substantially flat, with an almost constant slope and incisions due to the poorly marked draining network. While, with a more detailed examination of the morphology of the reliefs, it appears much more articulated and in close correlation with paleo-hydrography, which has shaped the plain areas giving rise to bumps and areas more depressed with appreciable gradients.

The forms of the territory are essentially connected to the fluvial dynamics that have characterized the watercourses in the last centuries, although the embankment has blocked its natural evolution, preventing it from wandering freely. It seems quite clear that, in the absence of human actions, the watercourses would have abandoned their current path, developing a more rectilinear path.

It should however be noted that the morphology of the area is not evident and detectable on site, both for the small slopes and for the intense anthropogenic action, aimed at modeling the ground. In fact, over the centuries, the human community has made continuous changes to the territory to make it feasible for housing and agricultural purposes.

The identification of relief areas and depressed areas is instead easier through the analysis of the distribution of the granulometric classes of surface deposits; in particular, the identification of depressed areas (valleys or interfluvial basins) is marked by the presence of fine and very fine deposits. These areas, due to the impermeability of the soil, were wetland areas and only reclamation works have given it its current appearance.

Of great interest can also be considered the "*crevasse splays*" along the current riverbeds and along the bumps corresponding to ancient riverbeds, characterized by coarse granulometries, mainly sandy and generally located on the concave shore of meanders, that is at the major energies of current. Moving away from them we find increasingly finer sediments: with silt dominance, at the distal banks, and clayey in interfluvial areas. This phenomenon is clearly highlighted in [Figure 2.6](#), which focuses on the area under study, where both along the Secchia river course and where there should be an ancient riverbed, the granulometry of the soil is coarse, i.e. mainly sandy; while it becomes more fine moving away from these areas.

Focusing on the Secchia basin, it is characterized by reliefs between 2'000 and 1'000 m a.s.l., in fact it starts to flow in the Alpe di Succiso, at 2'017 m a.s.l., at the border of the province of Reggio Emilia and Massa Carrara. Secchia extends in length for 172 km, until reaching the confluence with the Po river. The basin of Secchia river ([Figure 2.7](#)) has an area of 2'090 km²; the 57% of this surface is in mountain environment.

It has a high rainy regime in the ridges, because of the presence of strong meteorological fronts caused by the orographic position and by the proximity of the Ligure sea; whilst in the hills and in plain the rainy regime is of small entity.

Mean precipitations have a big span, going from 700 mm/year up to 2000 mm/year.

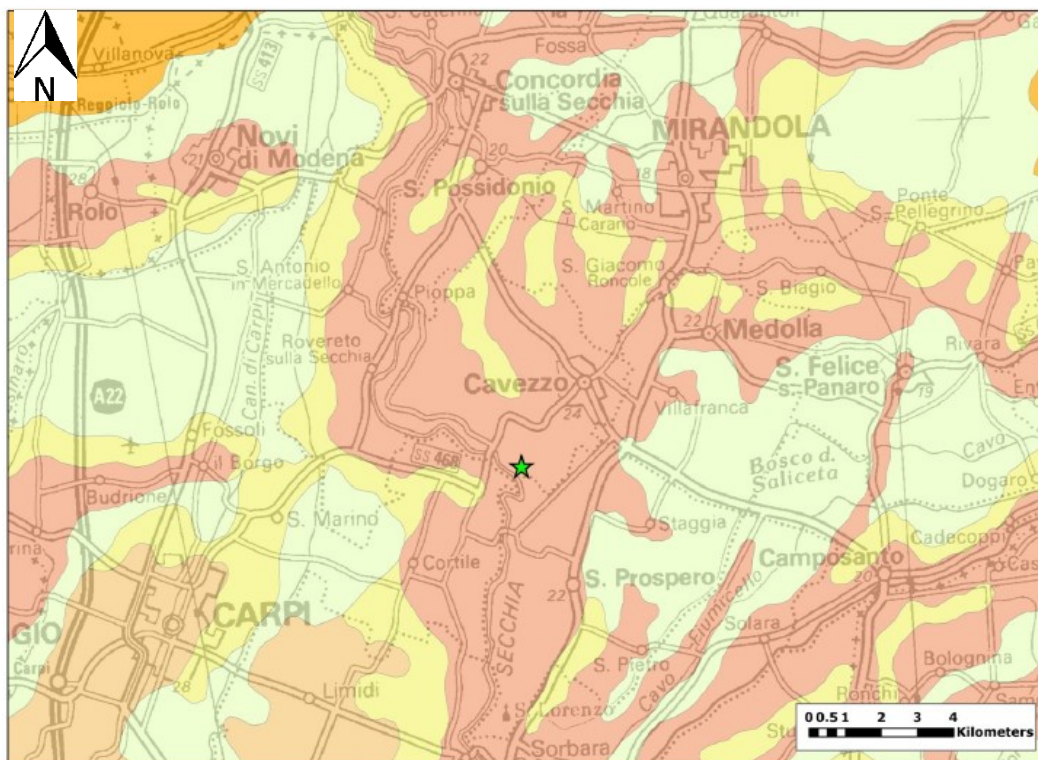
Intense weather events can happen all over the year, but the months characterized by the highest incidence are those between September and November.

The superficial flow is not influenced by effects of infiltration in the soil and by phreatic behavior of rocky substrate, since the basin is almost impervious, as stated in the previous chapter.

The Secchia starts to flow in plain surface at Sassuolo, where it receives a tributary, the Tresinaro stream. From here, the Secchia follows a meandered course, until its confluence to the Po, near Mirasole.

The hydrographic network is in continuous development, because the mountain part of the basin is mostly characterized by clayey formations and loose deposits, which are easily erodible. As consequence, the whole basin is featured by a strong solid transport, which is the cause, as previously said, of the everchanging morphology.

In its planar part, the river flows inside levees, and the bed is characterized by notching, which progressively lowers its height.



- | | | | |
|--|--|---|---|
|  | 1. Gravel and sand amalgamated in lenticular and canalized bodies, separated by sand and silty sand in layers few decimeters thick. |  | 6. Sandy silt, fine and very fine sand, silty clay, separated by silty-clayey sand in layers few decimeters thick. Deposits of distal embankment. |
|  | 2. Sand, sandy silt and silt, in layers few decimeters thick, sandy gravel and sand in canalized and lenticular bodies. Deposits of conoid and terrace. |  | 7. Medium and fine sand, separated by layers of silt and clay; locally medium and coarse sand bodies. Various channel and levee deposits. |
|  | 3. Silt and clayey silt in layers few decimeters thick, separated by gravel and sandy gravel in canalized and lenticular bodies. Deposits of conoid and terrace. |  | 8. Clayey silt and sandy silt, separated by layers of fine sand few decimeters thick; locally sands in lenticular bodies. |
|  | 4. Gravel, sand, silt and clayey silt. Undifferentiated alluvial deposits. |  | 9. Silty clays and clay, locally partially decomposed organic material. Interfluvial area and marsh deposits. |
|  | 5. Medium and fine sand in layers few decimeters thick, separated by fine silty sand; locally medium and coarse sand in lenticular and ribbon-shaped bodies. Deposits from the channel and the embankment. |  | 10. Medium and coarse sand, separated by deposits few decimeters thick of gravel and sandy gravel, silts and sandy silt. Alluvial and meander deposits. |

Figure 2.6. Type of soils.

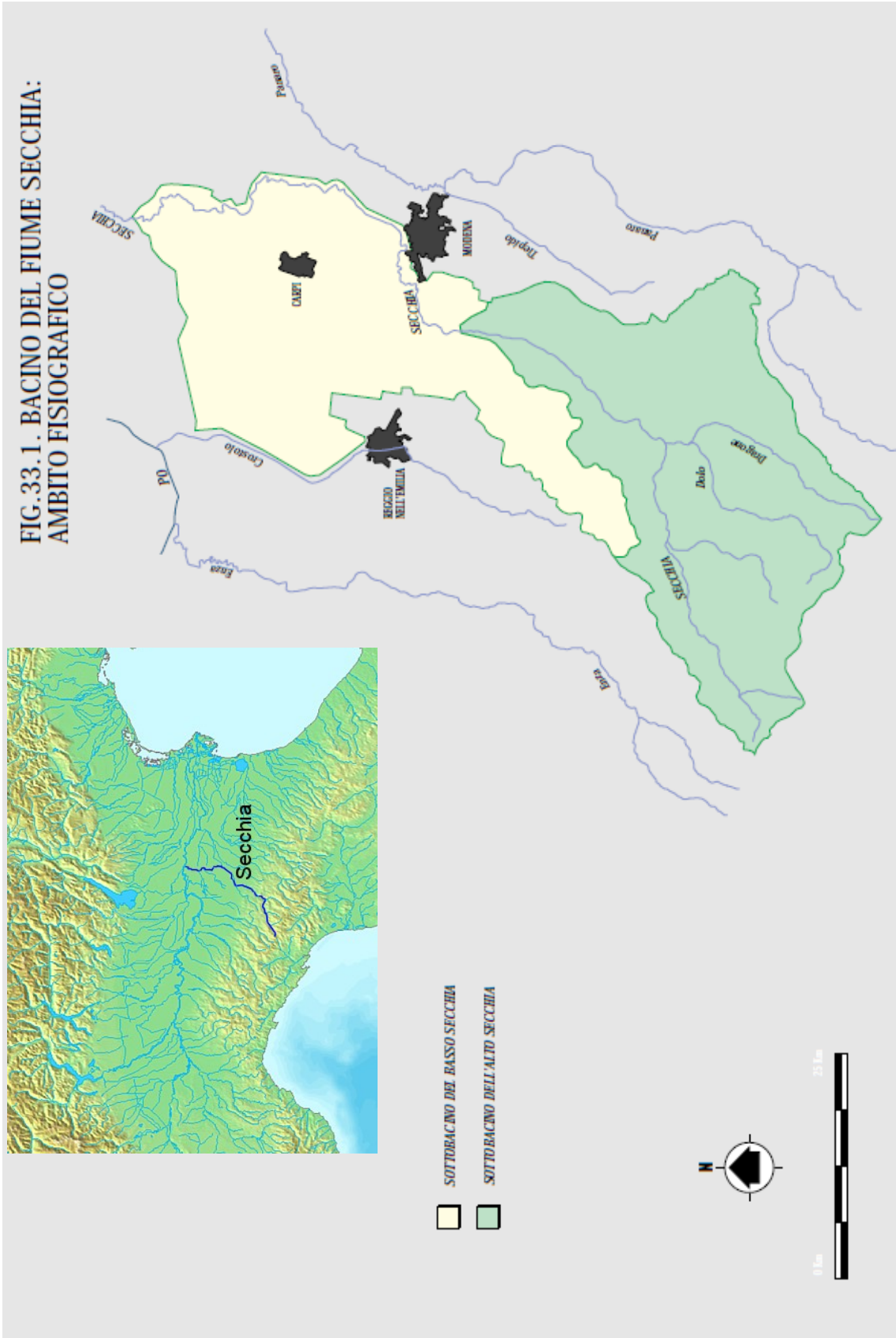


Figure 2.7. Secchia river and its tributaries.

3. Levees: role, components and mechanisms of failure

A levee is an either natural ridge or artificial fill that follows the stream of a river. It has three main hydraulic functions: to retain the water, reducing the risk of inundation of the external area; to channel floodwater downstream; to control the flood events with floodplains and detention basins.

A levee has many components; those shown in [Figure 3.1](#) are the generic ones and covers the majority of the cases.

The *foundation soils* are situated below the levee and interact with it. They must be taken in consideration when designing a levee, especially for their strength, permeability and texture, because they can affect its performances. They must sustain the weight of the levee and guarantee impermeability.

The *earth-fill* is the main volumetric component of a levee. It is composed of cohesive soil material, generally available in-situ. It provides stability against water pressure and minimize seepage.

The *impermeable core* provides for eventual inefficiency of the earth fill. A possible alternative to the impermeable core is an *impermeable mask*, put all over the levee. Their aim is to produce a resistance against water pressure and against infiltration; moreover, the impermeable mask prevents erosion problems.

The *crest* is the top surface of the levee. Generally, it is flat and horizontal; it protects the core of the levee from external agents (rain or possible overtopping of the water of the watercourse) that could cause erosion, and makes the levee accessible for maintenance or for recreational purposes.

The *revetments*, present over the both sides, are the interface between the levee and the external environment. These revetments are often made of grass, asphalt or geotextiles, and provide protection against erosion, caused by the current or by waves in the waterside, and by surface runoff or other agents in the landside.

The *berm* is a flat zone below the crest, usually built in the waterside. It helps to stabilize the levee by flattening its side, by increasing the path of the seepage through the levee and by relieving the weight of a possible overtopping discharge over the levee.

The *filter layers* are zones made of permeable materials, which help water to filter downward, in order to prevent soil displacement from the impervious core to the earth-fill.

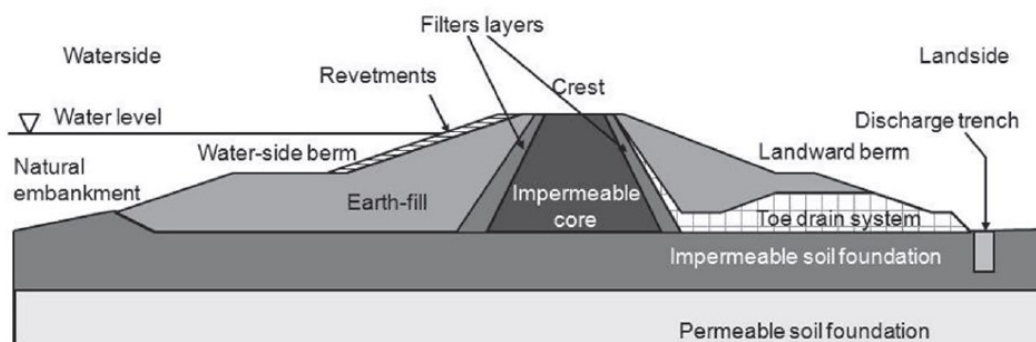


Figure 3.1. Components of a levee.

When a levee is no more able to guarantee the design performance, it is in state of failure. Since the main purpose of a levee is the protection against floods, a levee system is defined failed for example when the landside has been flooded.

There are two types of failure: non-structural (or hydraulic) failure and structural failure.

The hydraulic failure occurs when water is able to pass over the core of the levee and reach the landside; it is caused by overtopping of the levee, overflow of by piping. Structural failure is caused by a breach occurred in the levee system, as the one occurred along the Secchia in the 2014 ([Figure 3.3](#)).

There are many ways in which a levee system can fail, as described in [Figure 3.2](#). Apart from causes derived from hydraulic boundary conditions, such as flood events, there are three main causes that can lead to a levee to failure or in the worst scenario, to breach:

- Macro-instability: when water infiltrates into the embankment body, due to rainfall or to a high level of the water body, the pore water pressure inside the levee increases. While the pore pressure increases, the effective stresses σ' decrease, according to Terzaghi's law. The decrease of σ' causes instability because of the shear strength decreases. Thus, when along a plane shear stresses will be higher than the shear resistance, instability occurs along that plane, causing failure. Besides, the higher weight of the water inside the levee can contribute to trigger the driving moment that will cause instability. This phenomenon is described in the (C), (D), (E) cases in [Figure 3.2](#).
- Micro-instability: it occurs when a phreatic surface is formed from the free water surface of the water course to a lower point in the landside of the levee. The gradient of the phreatic surface identifies the direction of the movement of water inside the levee, which in this case is able to overcome the shear resistance of the soil and causes the removal of particles from the core of the levee, which will exit from in the landside. This removal is cause of instability. Case (F) in [Figure 3.2](#).
- Internal erosion: it's the mechanism through which water passes through the levee body thanks to existing cavities (e.g. animal burrows) or voids and removes soil particles. The soils characterized by this phenomenon, called *piping*, are generally permeable, poorly compacted and prone to erosion, with a high void ratio and low density, such as silts, silty sands. Case (G) in [Figure 3.2](#).
- External erosion: caused by wave damage or weather agents. Generally, it doesn't result in a breach, but it can decrease the efficiency of the levee. Cases (H) and (I) in [Figure 3.2](#).

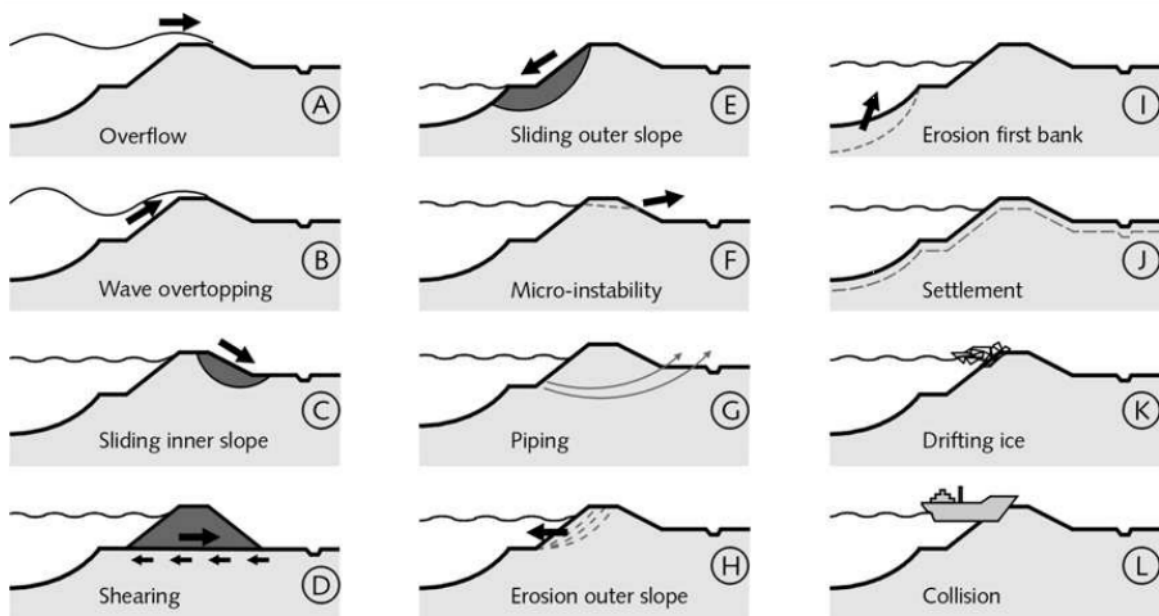


Figure 3.2. Main failure modes. Source: Schierek (1998), TAW report⁴.



Figure 3.3. Breach of the right levee of the Secchia river, San Matteo (MO). Image from Protezione Civile Modena - Aeroclub Marzaglia.

⁴ Schiereck, G. J. (1998). Fundamentals on water defenses. TAW-ENW report.

4. Characteristics and problems of the studied embankment

This chapter focuses on the morphological description of the studied embankment and will present the geognostic tests that has been performed along the embankment.

4.1. Morphology of the area

The studied area ([Figure 4.1](#)), which is in the plain area of the province of Modena, is located between the municipalities of Cavezzo (MO) and San Prospero (MO), and in particular it is the right embankment (hydrological right) of the Secchia River. In the upstream part, the river flows in direct contact with the levee, while going downstream and till Ponte Motta, a floodplain of variable extension, reaching 400 m near Ponte Motta, separates the levee from the river course.

The embankment has a height of 9 m with respect to the level of the ground and from 4 to 5 m with respect to the floodplain level, it has slopes both slightly below 1:2, without banks, as depicted in [Figure 4.2](#), representing a cross section of the embankment. The shape of the embankment, which is the result of numerous and successive additions, has been found to be strictly related to the problems of water ponding after flood events, because the drainage of water to the land side is difficult.



Figure 4.1. Geographical position of the studied area. The red line indicates the cross section of the following figure.

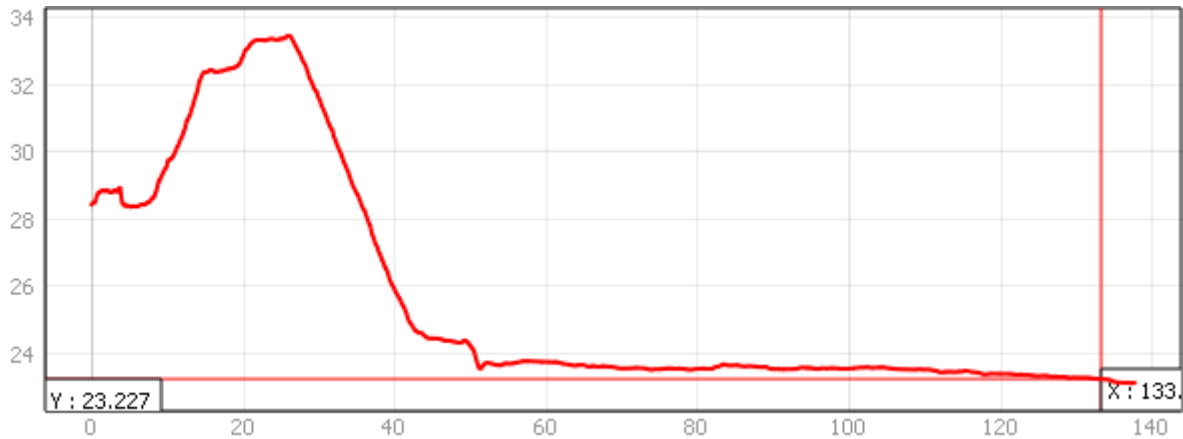


Figure 4.2. Cross section of the levee of the Secchia river in Via Bozzala (MO). Measures in meters and m a.s.l. for the height, from the DSM of the area.

An important feature of this area is the presence of a buried ancient riverbed of the Secchia River, as stated in Section 2.2, which detaches from the actual stream segment, going in a N-NE direction. This ancient riverbed is thought to be the cause of the seepage problems in the area near the embankment, when the hydrometric level rises and water, through piping, can reach the land side.

4.2. Water piping during 2014

The embankment has suffered from water piping problems in the last years, especially after flood events. In particular, from December 2013 to March 2014, the Secchia river has undergone a long series of floods (

Figure 4.3), along with the breach of part of an embankment near San Matteo on the 19th of January 2014.

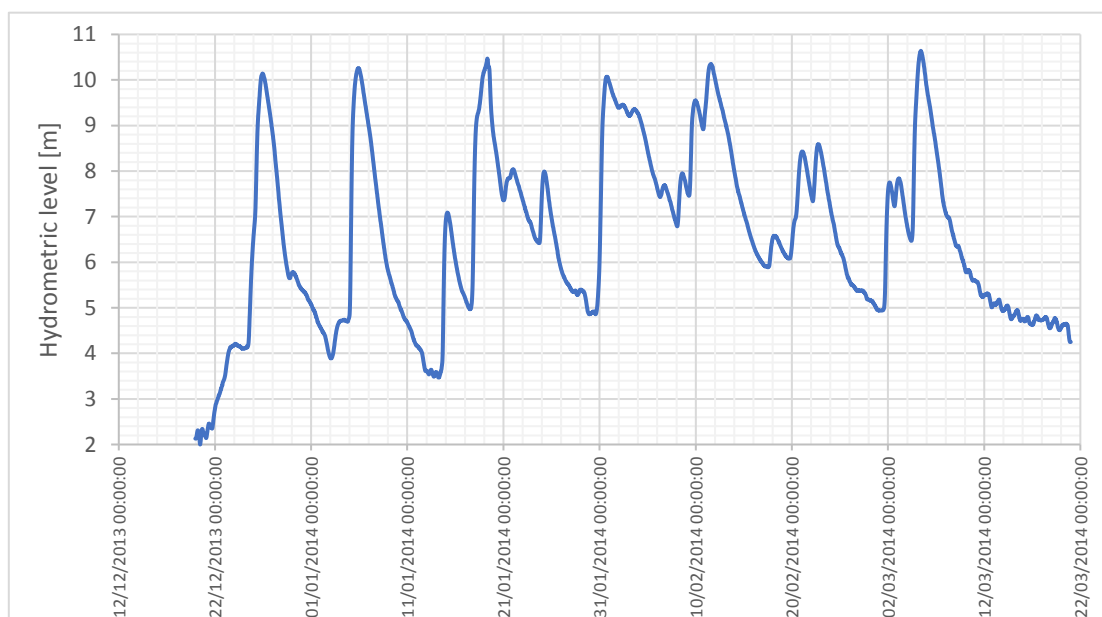


Figure 4.3. Hydrometric levels of Ponte Bacchello from 20/12/2013 to 20/03/2014.

Concentrated seepage (Figure 4.4) near the civic 10 of via Bozzala, in date 03/02/2014 has been also detected. This seepage required the building of an embankment made of sandbags (Figure 4.5). The geological investigations revealed the presence of burrow holes⁵, which have been sealed.



Figure 4.4. Concentrated seepage near the civic 10 of Bozzala street.



Figure 4.5. Embankment made of sandbags, made in date 08/02/2014.

4.3. Geognostic Investigations

After the breach of the embankment near San Matteo (MO) on the 19th of January 2014 and the water piping occurred as previously stated, the basin authority AIPo commissioned to Engeo Srl some tests (CPTU, electrical tomography, triaxial test, granulometric analysis and geophysical prospection with

⁵ Engeo srl Studio Geologico ed Idrogeologico (2014). Fiume Secchia: Lavori urgenti per il miglioramento delle condizioni di stabilità del corpo arginale nei confronti di fenomeni di filtrazione – Geological and seismic report. AiPo.

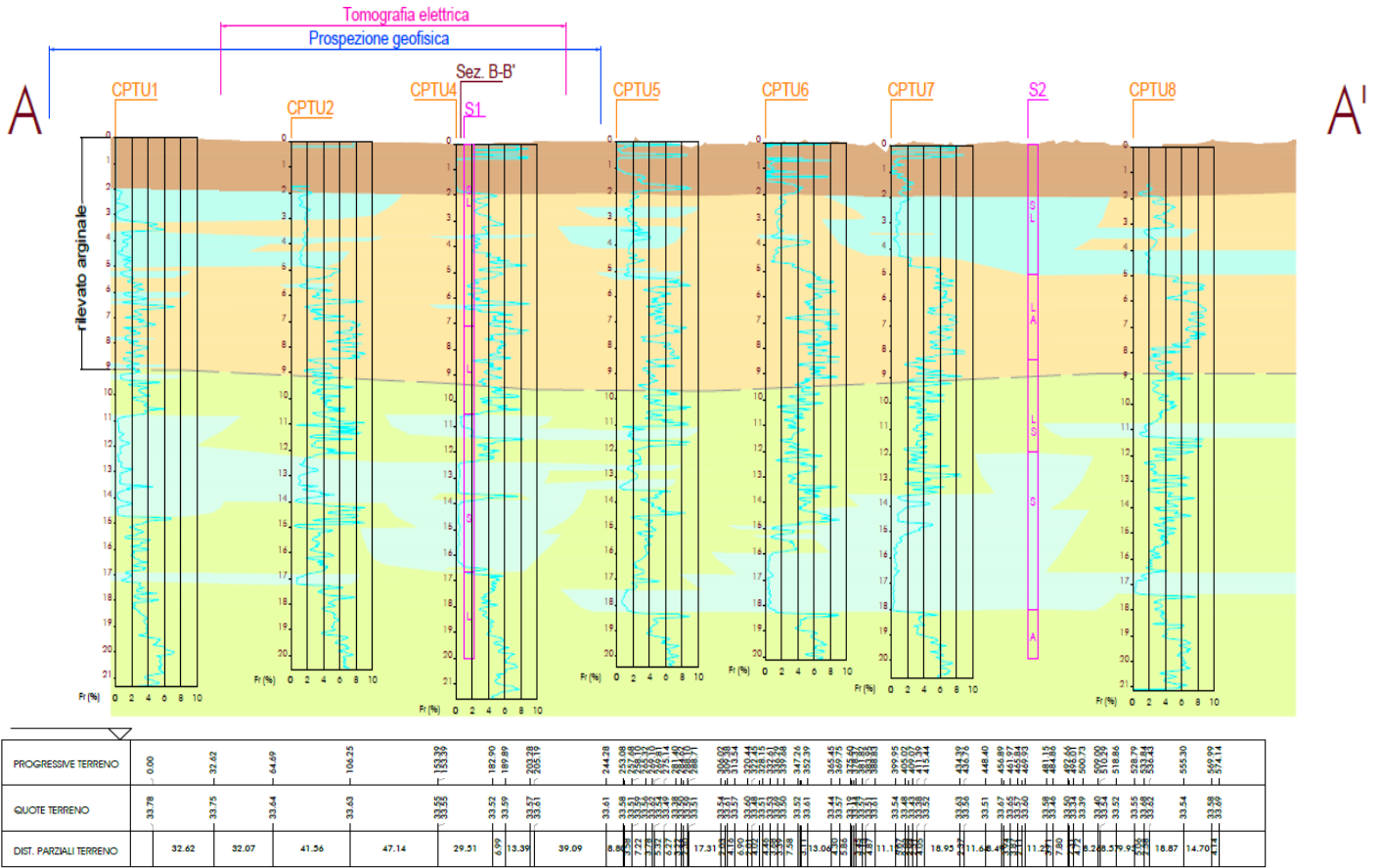
refraction seismic method) to understand the characteristics of the embankment and therefore also the nature of the seepage. In [Figure 4.6](#) the performed tests and their position are presented.

[Figure 4.7](#) and [Figure 4.8](#) show respectively the longitudinal and the cross sections of the embankment; the analysis of stratigraphy revealed that the first 2 meters starting from the top are composed of a mixture of materials, from clay to gravels, with pebbles; the main body is mostly made of clayey or silty material, with low permeability, but also large sandy levels have also been found, which can be preferential ways for the seepage of water inside the embankment body. They vary in thickness, from few centimeters up to 3 m.

The foundation soil is mainly composed of material with low permeability, clayey and silty soils, but even here sandy lenses can be found, with medium-high permeability, up to 6 m thick.



Figure 4.6. Geognostic tests performed along the embankment.



From these test, and especially from [Figure 4.8](#), is clear enough that the ancient riverbed is located below the embankment. Sectors where preferential groundwater flow occur due to the relatively higher permeability can be found in CPTU1 and CPTU4, where the sand soil is located around 13 m below the crown of the embankment, which means from 2 to 5 m below the ground surface external to the banked area; and from CPTU 6 to S2 (continuous core drilling).

Therefore, the ancient riverbed is not uniquely identified, but it probably wandering. It can however be noted that it runs almost parallel to the embankment in the section from CPTU1 to CPTU4.

4.4. Waterproofing intervention

To prevent seepage processes that might lead to the collapse of the embankment, a waterproof sheet pile has been installed, 200 m long and 12 m deep, to stop water from filtering under and across the embankment. The planimetry of the project is shown in [Figure 4.9](#), and its cross section is shown in [Figure 4.10](#).



Figure 4.9. Planimetry of the sheet pile. In yellow the concrete mantle, in pink the sheet piles, in orange the crown of the embankment.

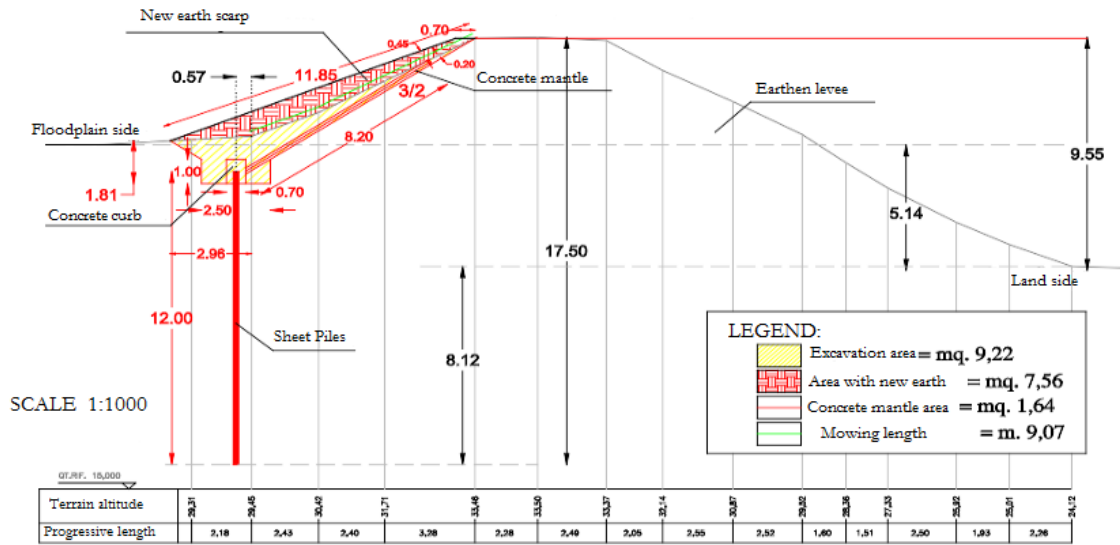


Figure 4.10. Sheet piles and embankment cross-section.

However, even after the building of the waterproofing sheet piles, when the water rises during flood events, and the floodplain get submerged, seepage still occurs in the land side, and especially in the areas between the houses and the levee, as testified by the inhabitants.

5. Experimental monitoring project

In this chapter, the experimental monitoring system will be described.

5.1. Objective of the project

After the installation of the sheet piles, and the securing of the part of embankment where these have been put, it has been observed that seepage problems still remain, creating potential critical conditions. The basin's authority thus decided to test a multiparametric monitoring system, which has been located immediately downstream with respect to the sheet piles.

The objective of this monitoring system is to allow AIPo to control the interstitial pore water pressures, the humidity and the displacement inside the embankment, especially during flood events. Moreover, the acquired data will progressively build a data base that will help AIPo to model the behavior of the embankment during and after floods, allowing to deal with emergency conditions; and to decide whether consolidation measures are necessary.

Once the effectiveness of this monitoring system will be proved, it will be possible to extend it to other critical points of the whole Po basin.

5.2. Architecture of the project

The monitoring system consists in a hydrometric station (ultrasonic hydrometer ULM20) installed at Ponte Motta, downstream the section of the studied embankment, and of a Wireless Sensor Network (WSN) along the embankment. All the data acquired by the installed sensors are sent by the related W-Point to the W-Master station installed at Ponte Motta through a wireless connection, and then to the central of AIPo in Parma, where they will be available to the personnel.

Because of different boundary conditions, different geomorphological and geotechnical characteristics, the studied embankment has been divided in three parts, as shown in [Figure 5.7](#), each equipped with a W-Point:

- *Upstream section*: the river has a flooded bank;
- *Median section*: in the part of the embankment where the sheet piles have been installed. The floodplain has a lateral extension of 80 meters;
- *Downstream section*: area downstream respect to the part of the embankment stabilized with the sheet piles. The floodplain has here a length of 200 meters. Here, during the past, have been observed important episodes of seepage.

The instruments installed are:

- **Casagrande piezometer P101**: it's an instrument used to measure the pore water pressure at the depth where it has been installed. For each piezometer, it has been performed a perforation, with internal diameter of 101 mm. The hole excavated was firstly cleaned with water to remove fine particles. Then, the Casagrande cell was put between two drains of 50 cm and 70, made of fine sand or gravel, respectively put before and after the piezometer. Then, over the upper drain, a bentonite impermeable seal was

imposed. Finally, the hole was filled with cement and the opening closed with a manhole cover of cast iron;

- **Humidity sensor SM150:** it's a sensor able to measure the water content inside the soil. Each sensor has been put inside a previously made perforation of 101 mm of internal diameter. The hole was then filled with inert material, for 1 meter, and with cement mixture for the remaining thickness. The wellhead was closed with a manhole cover made of cast iron. The installation scheme for the section consists in three humidity sensors put at 2 meters of distance, and each at different depth (Figure 5.1);

- **Multiparametric chain:** it consists in a set of different sensors, able to measure different parameters. The sensors to be installed in the set are selected according to the scope of the monitoring. Since the monitoring system's aim is to detect possible causes of collapse of the embankment, the parameters to be monitored are possible deformations of the embankment, caused by flood events, the temperature and the pore water pressure inside the embankment. The sensors used are:

- Inclinator sensors Tilt Link HR;
- Temperature sensor;
- Piezometer sensor Piezo Link.

The inclinometer and temperature sensors have been installed with a pitch of 1 meter, to detect each possible failure surface, while the piezometer was installed inside the sand deposit detected below the embankment. The scheme of installation is represented in Figure 5.2.

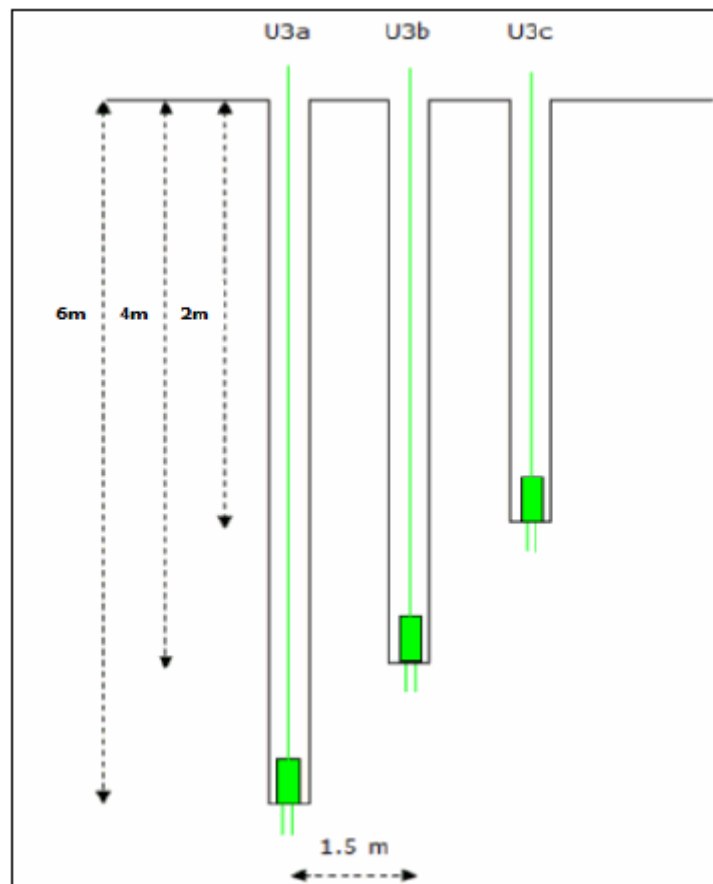


Figure 5.1. Installation scheme of the humidity sensors.

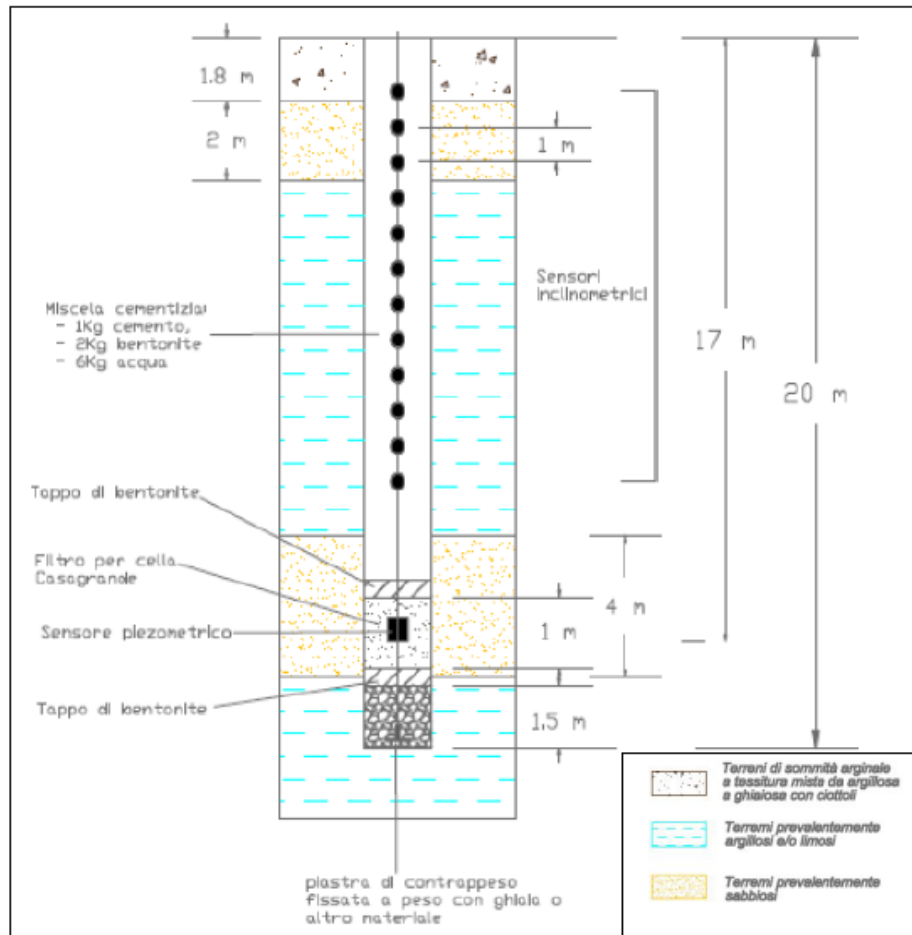


Figure 5.2. Installation scheme of the multiparametric chain.

5.3. Upstream section

In the upstream section n.2 Casagrande piezometers, with removable pressure transducers, have been installed:

- Piezometer P1: installed inside a sandy silty deposit, at an elevation of 17.28 m a.s.l., corresponding to a depth of 16.5 m from the crown of the embankment;
- Piezometer P2: installed inside a clayey soil at an elevation of 24.28 m a.s.l., corresponding to a depth of 9.5 m from the crown of the embankment.

The two pressure transducers send the measured data to a W-Point station (installed at 2 meters over the surface of the embankment), which powers the sensors and also send the received information to the W-Master module placed in the hydrometric station of Ponte Motta. The scheme of installation is shown in [Figure 5.3](#).

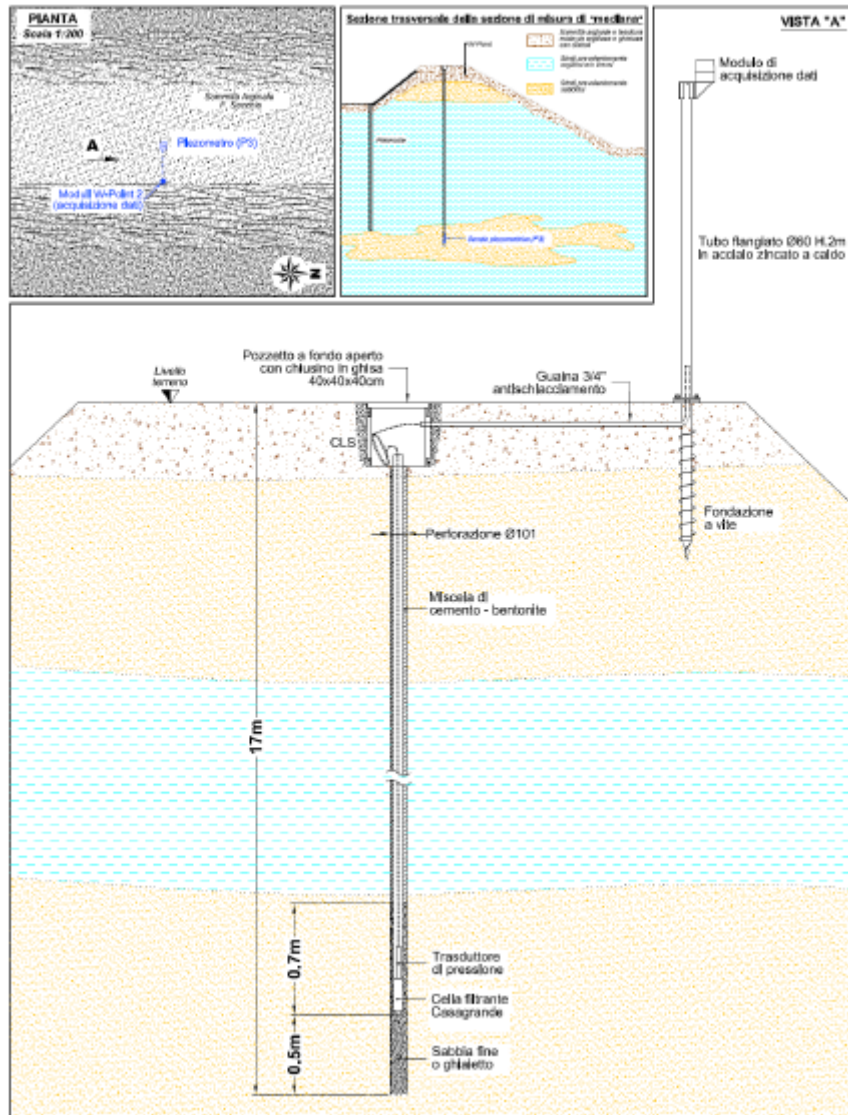


Figure 5.4. Installation scheme of the median section.

5.5. Downstream section

The downstream section, being the one still characterized by water filtering through the protected lowland, is the one that needs a complete and detailed characterization. In the specific, the following instruments have been installed:

- N.3 humidity sensors (U1a, U1b, U1c), set at different depth inside the levee body, respectively at -2 m, -4 m and -6 m from the crown of the levee;
- N.1 Casagrande piezometer P4, installed at a height of 24.55 m a.s.l., corresponding to a depth of 9 m from the crown of the levee;
- N.1 Multi-parameter chain INP1, equipped with n.12 inclinometer sensors, n.10 temperature sensors and one pressure transducer at a depth of 17 m from the levee summit. The aim of the inclinometer sensors is to detect deformations inside the levee body caused by the pressure of water

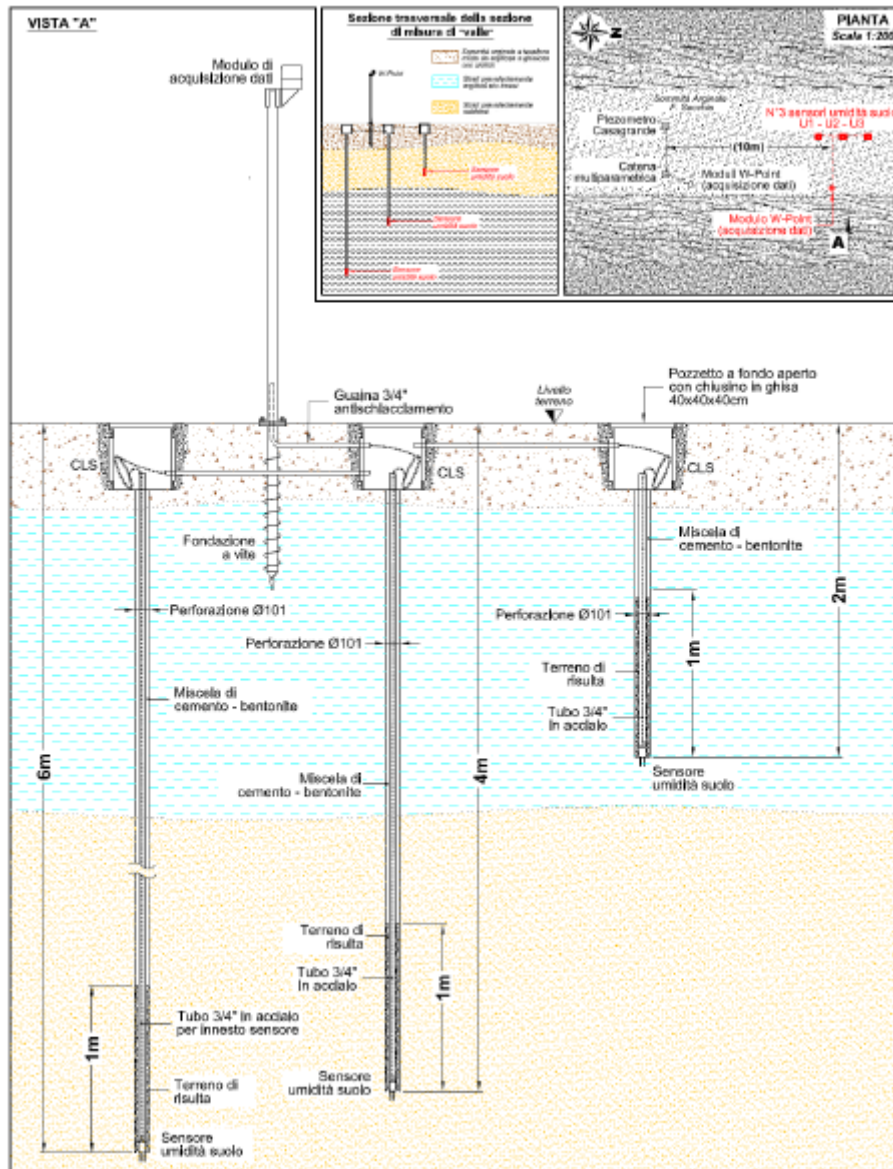


Figure 5.6. Installation scheme for the downstream section – humidity sensors U1a, U1b, U1c.

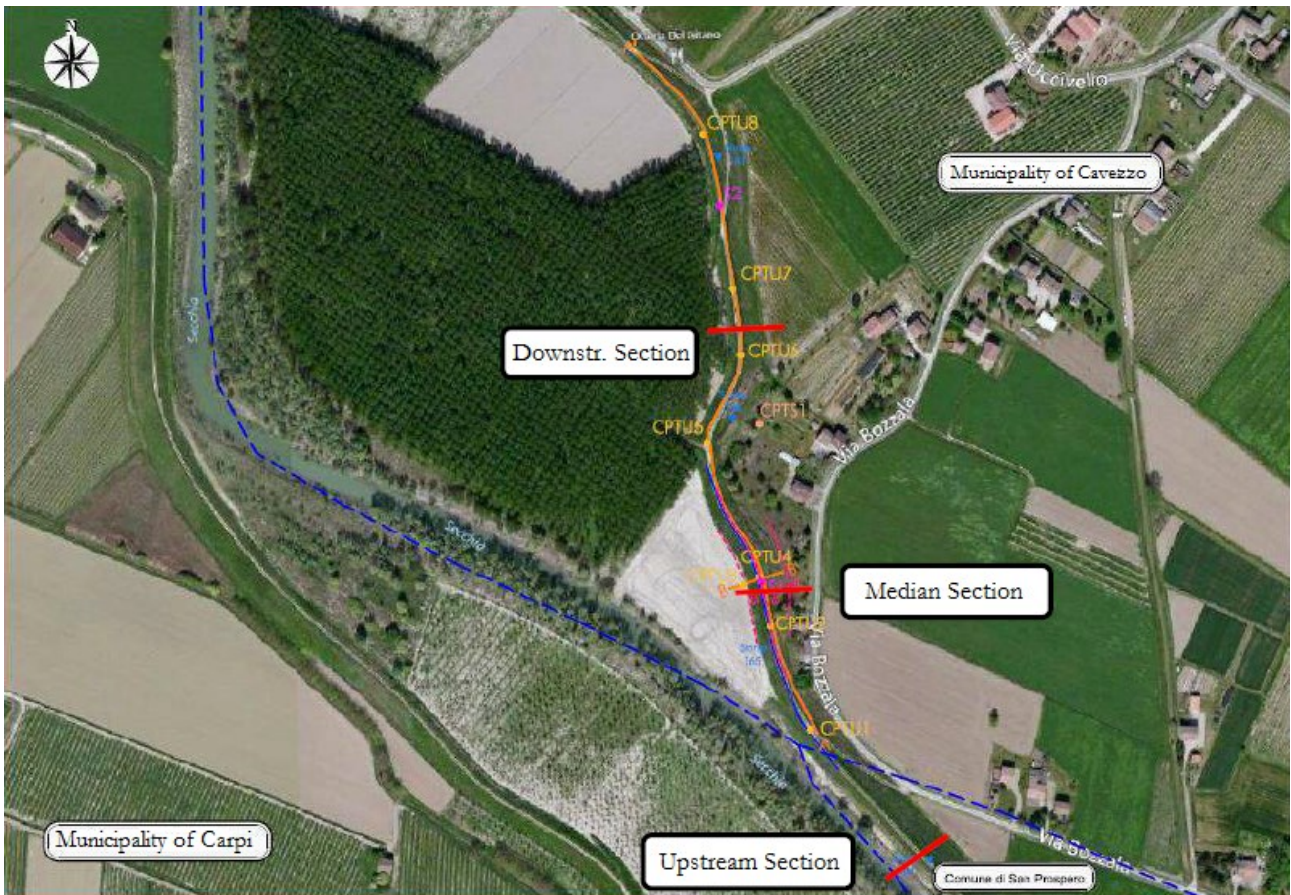


Figure 5.7. Disposition of the three sections of the monitoring network.

6. Analysis of the piezometric data

The pressure data that have been taken into consideration are those that might be useful to interpret remote sensing data. Since the surveys have been performed in May 2017, July 2017 and April 2018, those are the periods in which the analysis of the piezometers data will focus. Anyway, the eventual abundance of data will be useful to better understand the behavior of the groundwater flow in different periods than those of the surveys.

From the high quality DTM obtained from the photogrammetric reconstruction, the absolute height of the piezometers has been corrected with respect to the CAE report, and the depth values of the instruments have been recorded again and corrected by the personnel of AIPo in date 10/4/2018:

- P1 is located at 16.39 m a.s.l., at a depth of 16.84 m from the top of the embankment. It is situated in a silty sand deposit;
- P2 is located at 23.56 m a.s.l., at a depth of 9.79 m from the top of the embankment. It is situated in clayey soil, characterized by low permeability;
- P3, which is in correspondence of the sheet piles, is located at 17.23 m a.s.l., at a depth of 16 m from the top of the embankment. It is situated in a sand deposit, which is corresponding approximately to the depth of the sheet piles;
- P4 is located at 23.9 m a.s.l., at a depth of 9.38 m from the top of the embankment. It is situated in a clayey deposit;
- INP1 is located at 17.05 m a.s.l., at a depth of 16.5 m from the top of the embankment. It is situated in a sand deposit;

The pore pressure recorded by the piezometers, in kPa, have been converted in piezometric height value thanks to the conversion factor supplied by the manufacturer, which can also be obtained through the formula $u = z \cdot \gamma_w$, where z is the depth from the ground surface, u is the pore pressure and γ_w is the specific weight of water. The conversion has been done by multiplying the pore pressure value by 0.102 and adding to this the absolute height of the instrument.

The hydrometric zero of Ponte Motta has been fixed at 21.12 m a.s.l.

The floodplain levels are different for the median and the downstream section (in the upstream section, shown in [Figure 6.5](#), the floodplain is missing)

- Median section (P3): the floodplain is 90 m wide; the toe of the levee is located at 29.3 m a.s.l. in the floodplain, while in the landside at 24 m a.s.l. ([Figure 6.6](#));
- Downstream section (P4, INP1): the floodplain is more than 200 m wide; the toe of the levee is located at 29.3 m a.s.l. in the floodplain, while in the landside at 23.8 m ([Figure 6.8](#)).

In the present study, the moisture sensors installed in the embankment at different depths were not taken into account.

6.1. 2017 data

From February to August 2017 no significant flood events have been recorded, except for two peak discharges, in February and in May, which reached barely at 26/27 m a.s.l., which is not sufficient to reach the floodplain level in none of the sections. Nonetheless, from the trend of the data, shown in [Figure 6.1](#), it is possible to extrapolate some interesting observations.

Starting from the upstream piezometers, P1 showed the closer reaction to the increase of the hydrometric level in May 2017, in fact it increased for hydrometric levels higher than 22.5 m a.s.l.

In period of minimum flow of the Secchia river, such as from the end of May 2017 to July 2017, P1 showed a piezometric level higher than the hydrometric height of the river, meaning that the flow is directed from the aquifer to the river, which is recharged by groundwater.

For what it concerns P2, which records the pore pressure inside a clay soil inside the levee body, it has a decreasing trend from April 2017, and it's not influenced by the peak discharge of May 2017. Furthermore, even if the values from P2 are the highest, in terms of height, with respect to the other piezometers, it must be noted that P2 is the one with highest altitude (23.56 m a.s.l.), and its pore pressure values decrease from 10 kPa to 6 kPa, which correspond to 1 m and to 0.6 m of piezometric height. The presence of pore pressure inside the clayey soil it's referable to the overpressures caused by past flow events and that need long time to be dissipated, because of the soil's low permeability.

The piezometer P3 had a poor response to the peak discharge of May 2017. From this point till August 2017 it decreased till reaching values near to 40 kPa at the end of July 2017. A possible interpretation of this trend could be that during relatively small peak discharges, the impermeable barrier acts correctly, blocking most of the water seepage.

P4 and INP1 have been installed near one another. While P4 has been installed in a clayey soil, INP1 has been installed at higher depth, in a sand deposit. Since P4 most of the time has not recorded pore pressure values, or if it has they were extremely low, it has not been considered in the analysis.

Conversely, INP1 showed a trend similar to P2, even if it is situated, as previously stated, in a sand deposit. Its missed response to the peak of May 2017 can have the following reason: the sand deposit of INP1 is isolated within the embankment, and in order for the water to reach it, the clayey soil must be saturated first, which needs time and higher hydrometric levels.

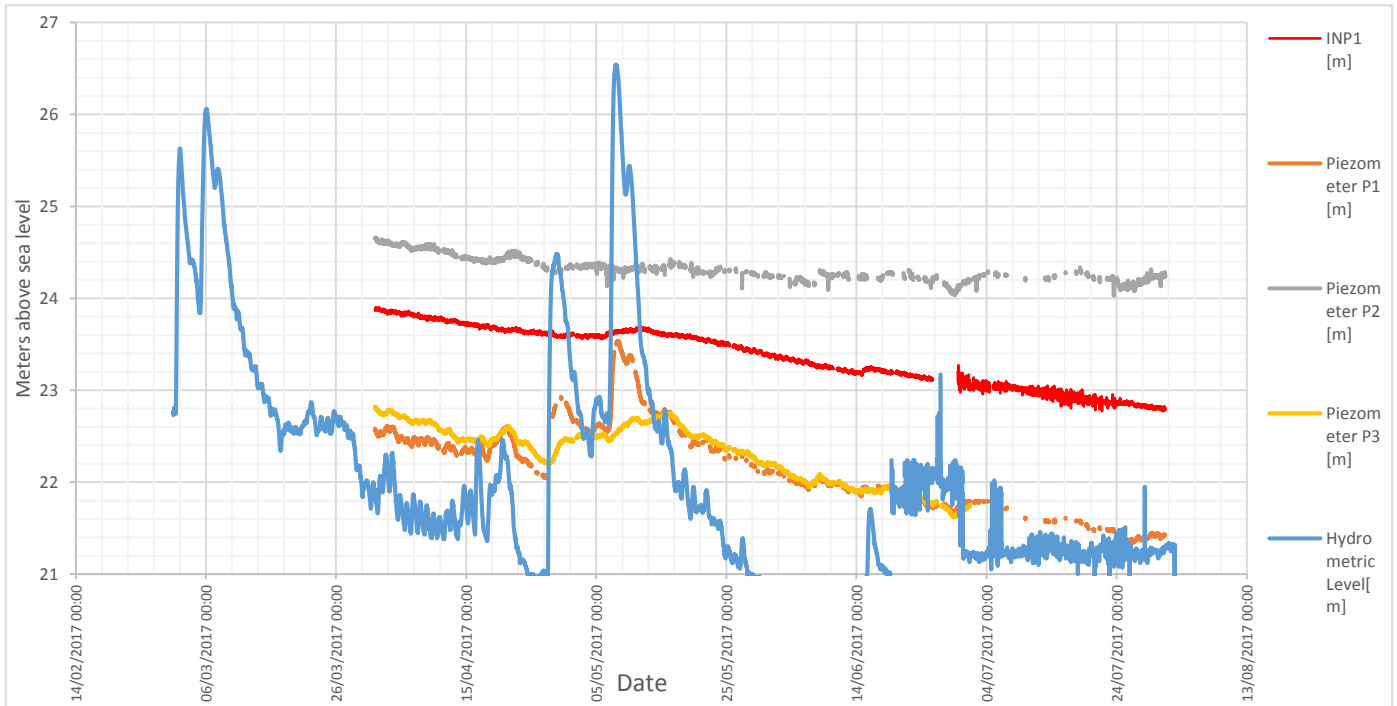


Figure 6.1. Hydrometric level and piezometric level from 03/ 2017 to 07/ 2017.

In the above graph, [Figure 6.1](#), it's clear that from the end of May 2017 and onwards the hydrometer showed problems. The interpretation of the graph can be easily solved, comparing the hydrograph of Ponte Motta with the hydrograph of Ponte Bacchello, which is situated few kilometers upstream. In fact, as showed in [Figure 6.2](#), the two hydrographs show the same height variation, along with a necessary time delay due to the water travel time. Thus, the hydrometric level of Ponte Motta after the end of May 2017 is in line with the mean of the scattering values of July 2017, which are characteristics of a low flow.

The hydrometric zero of Ponte Bacchello has been fixed at 23.45 m.a.sl.

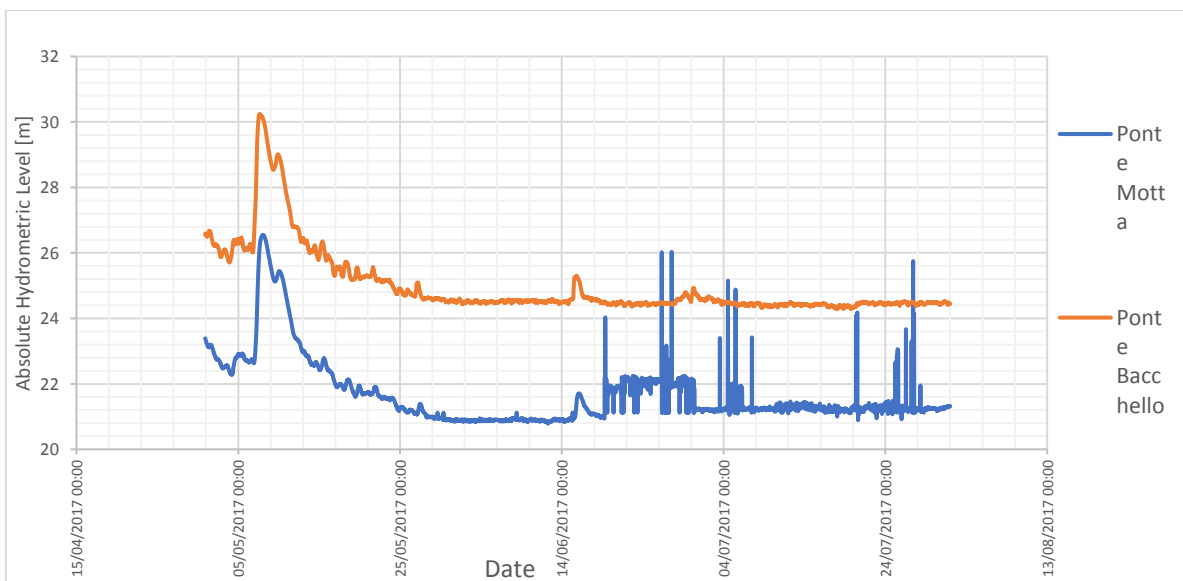


Figure 6.2. Hydrometric levels of Ponte Motta and Ponte Bacchello.

6.2. 2018 data

The Secchia River has been characterized by an important flood event during March 2018, with a peak flood which arrived at nearly 30 m a.s.l. in the sector of Ponte Motta. The flood started on the 8th of March and lasted till the 23rd of March; during these days the hydrometric level was higher than 28 m a.s.l. and for this reason the floodplain was flooded, causing the increase of pore pressure, registered by all the piezometers, except for P4. After this major flood, three secondary flood events occurred in a short span of time.

The hydrometric and piezometric levels are shown in [Figure 6.3](#).

In particular, levels in piezometer P1 showed the same trend of the river, even if the elevation reached is not very significant: the maximum is 25.45 m a.s.l. on the 20/03/2018. The fact that P1 increases simultaneously as the hydrometric level could mean that the aquifer is directly in contact with the riverbed of the Secchia River, and at the same time it is able to dissipate the pore water pressure, meaning that in this section ([Figure 6.5](#)) the groundwater can flow and it's not confined. The piezometric level recorded by P1 and the hydrometric level of Secchia River reached the same altitude at approximately 23 m a.s.l., on the 23/01/2018, 03/02/2018 and the 18/02/2018.

P2 has not been influenced by the flood of December 2017, but starting from the 30/12/17 it started to increase its level, until a sudden rise of the pore water pressure, reaching a maximum of 27.38 m a.s.l. on the 21/03/2018. In this occasion, the piezometric height of P2, initially at 24.6 m, started to increase after only one day since the Secchia river invaded the floodplain

In the successive lower discharge peaks, in April 2018, P2 is slightly influenced, probably because the saturated soil had a faster response time. From 4/4/18 P2's pore water pressure started to decrease, since the floodplain was no more flooded.

Concerning P3, it showed the more marked changes: its piezometric height has increased of 1 m, from 21.6 m to 22.8 m, during the flood event of December 2017, when the floodplain remained flooded for six days (from 11/12/2017 to 17/12/2017) and of almost 4 m during the flood event of March 2018, reaching 27 m a.s.l. (21/03/18) few days after the peak flow of 29.77 m (13/03/18). It's clear how the sheet piles proved to be not effective during the flood event of March 2018, while they blocked the groundwater flow during the flood of December 2017, which had a shorter duration.

P3 has shown a response for hydrometric levels higher than 25.5 m (06/03/2018 and 11/12/2017). From this it's possible to suppose that the ancient riverbed in the median section ([Figure 6.6](#)) it's not directly connected to the actual riverbed of the Secchia River. It can be supposed that the recharge of the aquifer begins from the upstream section, and to saturate this part of the ancient riverbed it's needed a certain hydrometric level persisting for many days to begin the groundwater to flow in the sand layers belonging to the ancient riverbed.

P4 did not show significant pore water pressure changes.

Finally, INP1 showed an increasing trend caused by the flood of December 2017, and the two successive peak flows on the 29/12/2017 and on the 04/02/2018.

During the flood of March 2018, the piezometric height of INP1 remained almost constant for the first five days, from the 07/03/2018 to the 12/03/2018. Starting from this day it had a marked increase,

reaching 26.7 m, and then started to decrease, even before the flood event finished. From the behavior of the pore water pressure recorded by INP1 it can be assumed that the sand lens in which the piezometer has been placed is more difficult to be reached by groundwater, since it is the farthest and a considerable time of high hydrometric level it's needed to increase the pore water pressure in the aquifer. Moreover, the groundwater flow is more likely directed towards the landside. In fact, in [Figure 6.3](#), during the three smaller flood events from 01/04/2018 to 14/4/2018, even though the hydrometric level increased, the pore pressure recorded by INP1 continued to decrease, except for a slight increase of 0.5 m on the 04/04/2018.

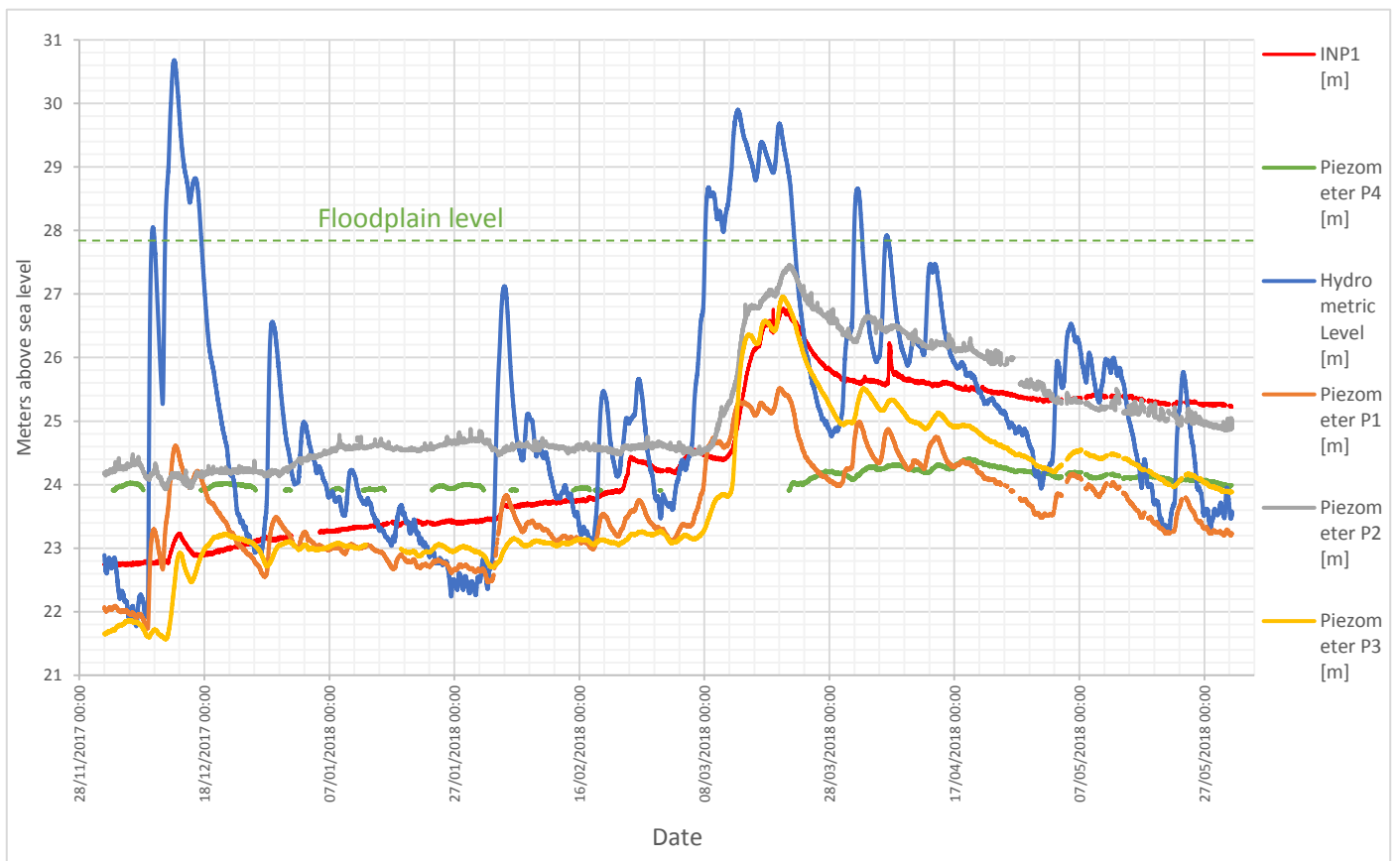


Figure 6.3. Hydrometric and piezometric levels from December 2017 to June 2018.

6.3. Geological cross sections

From the geognostic investigations performed by Engeo Srl and the piezometric data, it was possible to create three geological cross sections ([Figure 6.4](#)), comprehensive of the riverbed of the Secchia river and of the levee body, and to suppose the groundwater flow directions. The cross sections have been supplemented with data from AIPo where the DTM was not available, especially for the parts of the actual riverbed of the Secchia River.

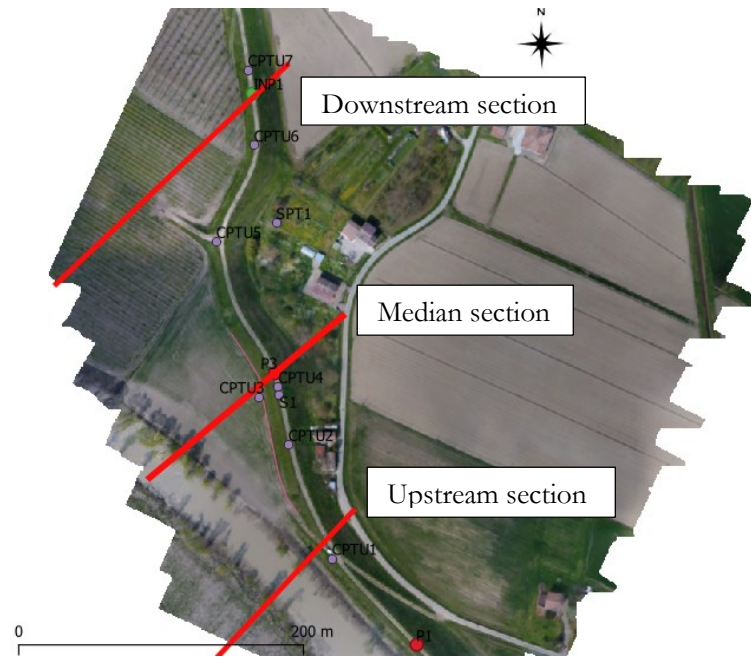


Figure 6.4. Map of the area with the three cross sections in red.

The upstream geological cross section, which is represented in Figure 6.5, shows the initial part of the floodplain and of the ancient riverbed. The sand layer is thought to be connected to the actual riverbed of the Secchia River since the piezometer P1 recorded increase of the piezometric height in correspondence to the increase of the hydrometric height. Furthermore, during flood events the pore pressure recorded by P1 doesn't reach high values, meaning that the groundwater flows towards the land side, while it flows towards the Secchia River during periods of low flow (i.e. when the piezometric height of P1 is higher than the hydrometric level).

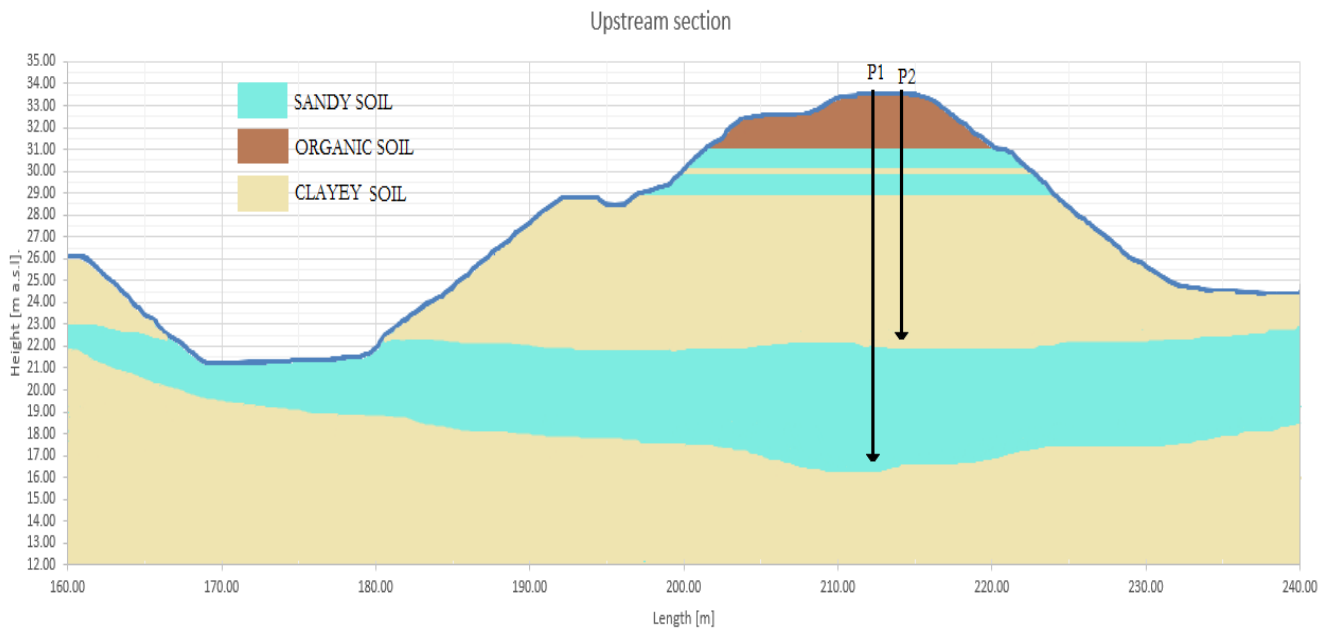


Figure 6.5. Upstream cross section.

The median cross section (Figure 6.6), which is the one that have been characterized by intense water seepage during the 2014 and by the building of the impermeable sheet piles, shows a wide floodplain (approximately 100 m) with an average elevation around 28 m a.s.l. This cross section is characterized by a thick sandy layer, which is not in direct contact with the actual riverbed of the Secchia River.

In fact, as stated in Figure 6.7, P3 detected increasing pore pressures after three days from the increase of hydrometric height, time necessary to saturate the clayey layer. Once the hydrometric level decreased, the pore pressure in the layer decreased as well, within a temporal difference of few hours. It has been supposed that also in this section the pore pressure decreases thanks to groundwater flowing towards the land side.

Moreover, in case of severe flood events, the pore water pressures can be dissipated also in the thin clayey soil layer separating the sand layer from the ground surface, leading to the phenomena of water ponding that have been witnessed many times by the inhabitants.

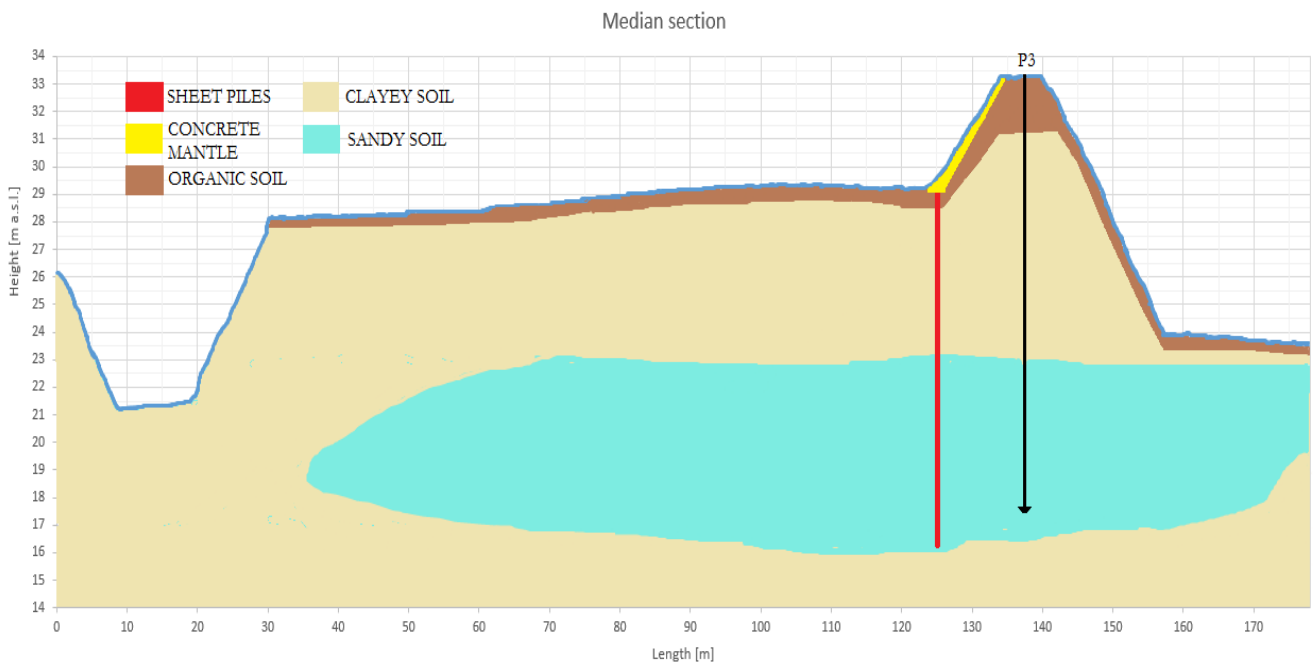


Figure 6.6. Median cross section.

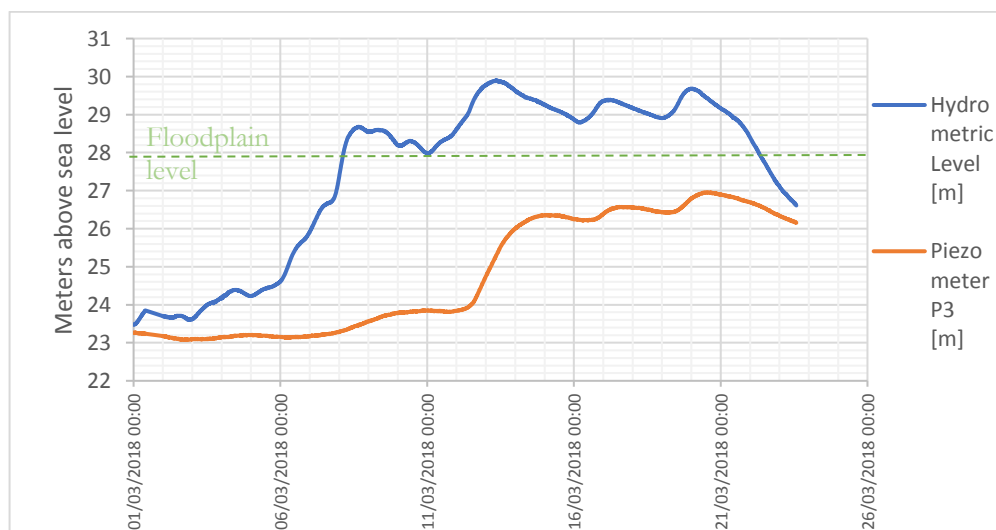


Figure 6.7. Piezometric and hydrometric height variations during a flood event.

Also in the downstream cross section in [Figure 6.8](#) the sand layer is separated from the riverbed of the Secchia River. As for the median cross section, INP1 recorded significant increases of pore pressure only for high hydrometric level ([Figure 6.3](#)), with water persisting for many days in the floodplain. Unlike the sand layer in the median section, which is able to dissipate the overburden pore pressure in few days, in this case the pressure needs many weeks to be dissipated.

This behavior leads to think that this sand layer is hydraulically separated from the land side and that the groundwater flows towards the Secchia River when the flood event finishes.

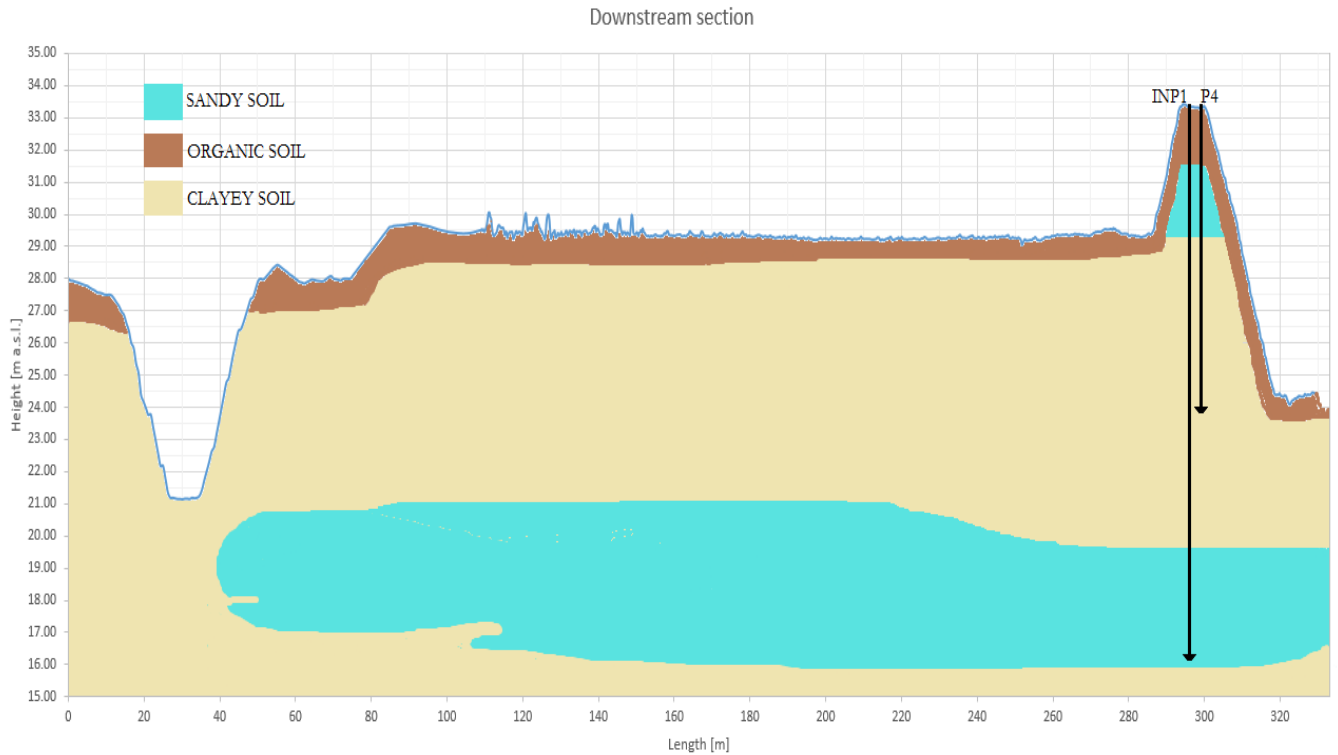


Figure 6.8. Downstream cross section.

7. Multispectral survey

In this section the main principles of remote sensing will be treated, and the procedure adopted for the multispectral surveys that have been performed will be explained.

7.1. Introduction to remote sensing technology

Remote sensing is a technique which consists in obtaining properties of an object of interest, without getting in contact with it. This is done thanks to the properties of the electromagnetic energy. The behavior of the electromagnetic energy is in accordance with the theory of waves, which states that electromagnetic energy travels in harmonic and sinusoidal waves (Figure 7.1), at the velocity of light c . It's called wavelength λ the distance from one wave peak to the following one, and it's called frequency ν the number of peaks that passes through a fixed point in a unit of time. The law that describes this behavior is:

$$c = \lambda \cdot \nu \quad (1)$$

Since c is practically a constant, frequency and wavelength are inversely related.

In the remote sensing field, it's common use to categorize the electromagnetic energy by their wavelength, generally expressed in micrometer μm (10^{-6} m).

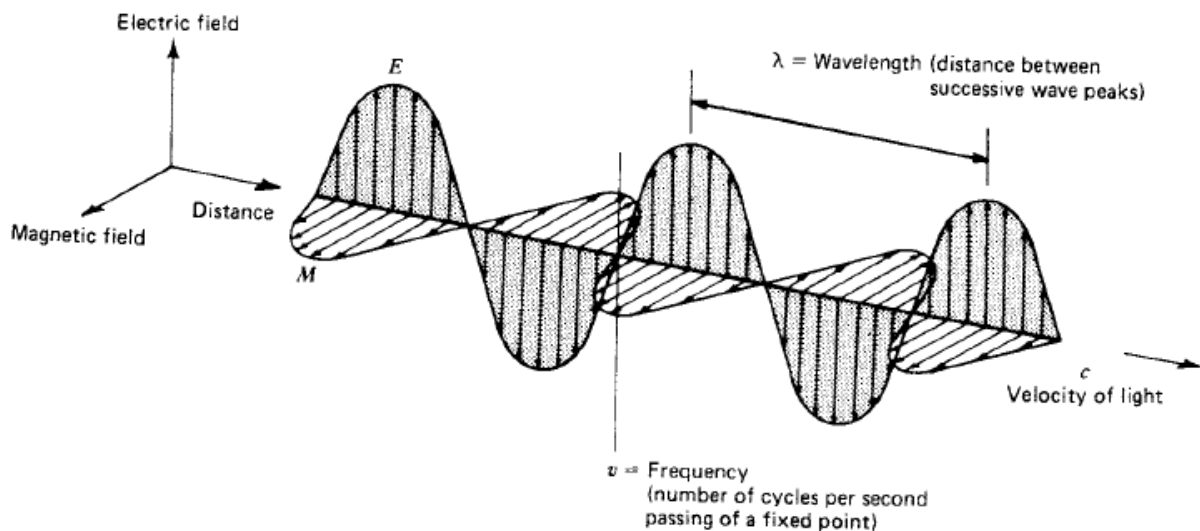


Figure 7.1. Description of an electromagnetic wave. Where E is the sinusoidal electric wave, and M is the magnetic wave. Both are normal to the direction of propagation.

The most used category in remote sensing is obviously the visible portion, which actually is very small, from $0.4 \mu\text{m}$ to $0.7 \mu\text{m}$. Where blue is in the range from $0.4 \mu\text{m}$ to $0.5 \mu\text{m}$, green from $0.5 \mu\text{m}$ to $0.6 \mu\text{m}$ and red from $0.6 \mu\text{m}$ to $0.7 \mu\text{m}$. After the $0.7 \mu\text{m}$ there are three different categories of the spectrum:

- Infrared Waves (IR): near IR from $0.7 \mu\text{m}$ to $1.3 \mu\text{m}$, mid IR from $1.3 \mu\text{m}$ to $3 \mu\text{m}$ and thermal IR from $3 \mu\text{m}$ to 0.4mm ;
- Microwaves from 0.4mm to 100cm ;

- Radio waves from 1 m to 100 m.

While at lower wavelengths, from the blue light and below there are respectively:

- Ultraviolet waves from 10^{-7} m to 10^{-8} m;
- X rays from 10^{-8} m to 10^{-11} m;
- Gamma rays below 10^{-11} m

The electromagnetic spectrum is summarized in [Figure 7.2](#).

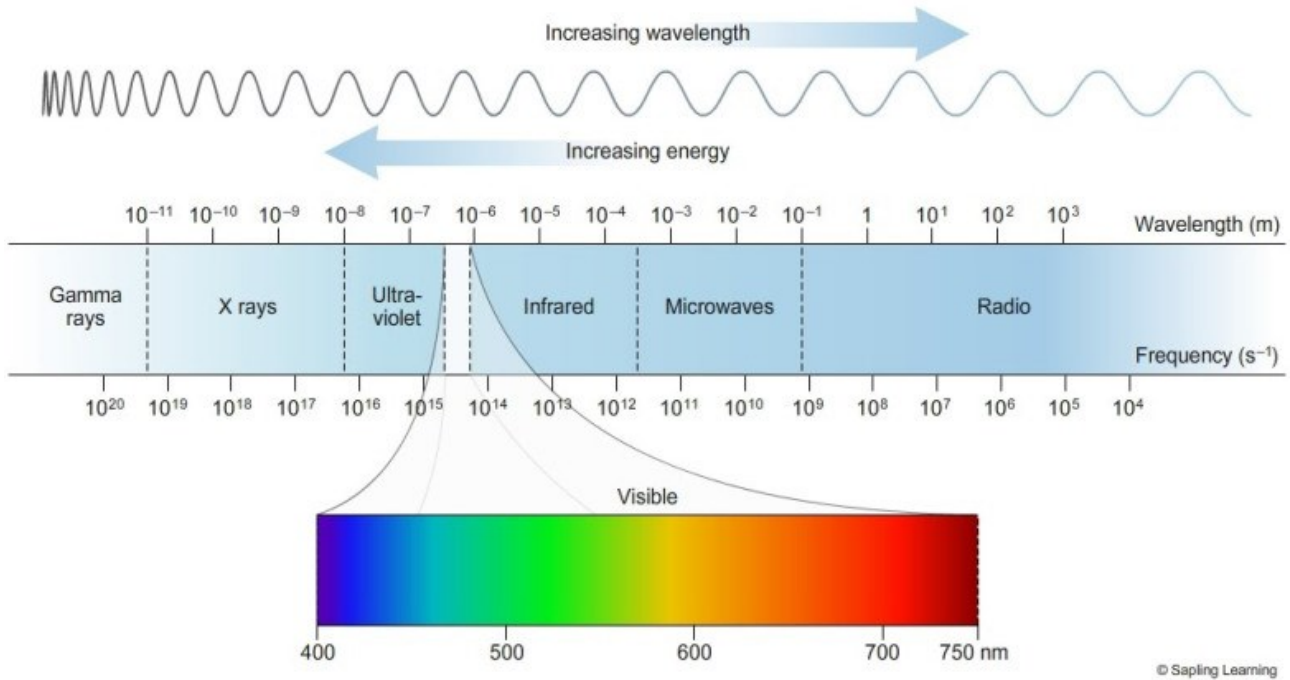


Figure 7.2. Electromagnetic spectrum.

7.2. Interactions between objects and electromagnetic energy

Three interactions are possible when an object situated on the earth surface is hit by electromagnetic energy: reflection, absorption and transmission. The relationship describing these interactions is the following:

$$E_I(\lambda) = E_R(\lambda) + E_A(\lambda) + E_T(\lambda) \quad (2)$$

where:

- E_I is the incident energy;
- E_R is the reflected energy;
- E_A is the absorbed energy;
- E_T is the transmitted energy.

Equation (2) is an energy balance which satisfies the principle of conservation of energy, and it can be noted that all the terms are function of the wavelength λ .

The terms on the right side of equation (2) vary widely depending on the material and the condition, but these are precisely the causes that allow to distinguish the different objects in a remote sensed image. As already said, the proportion of energy reflected, absorbed or transmitted depends on the wavelength.

This implies that two features may be identical if analyzed on a certain spectral range, but they may be different in a band with a different wavelength.

Another characteristic to be accounted is the geometric way in which the target object reflects the energy. This feature is mainly conditioned by the roughness of the object.

There are two main categories of type of reflection: *specular*, characterized by an angle of reflection that is equal to the angle of incidence, and *diffuse*, where the energy is reflected uniformly in all directions.

Anyway, these are only ideal reflection, where the specular is typical of flat surfaces, and the diffuse is typical of rough surfaces; the real types of reflection are between these two typologies, as described in [Figure 7.3](#).

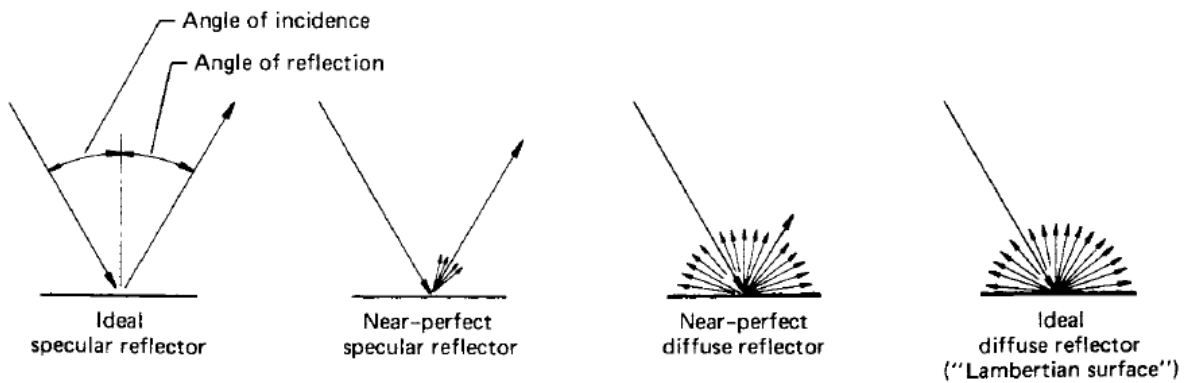


Figure 7.3. Typologies of reflection.

Each surface can be put in a category according to the surface roughness and to the wavelength of the energy that hits it. Moreover, the reflection type of a surface is determined by the wavelength of the incident energy with respect to variations in height of the surface. For example, a surface made of sand will appear smooth if hit by long wavelength energy, such as radio waves, but will appear rough in the visible part of the spectrum. This means that the height of the grains of sand is higher than the visible wavelength, but smaller than the wavelength of the radio waves. Thus, in the first case, when the wavelength of the energy hitting a surface is smaller than the surface height variations, the reflection will be diffuse.

In remote sensing, it is measured the energy reflected by a surface, defined as *spectral reflectance* ρ_λ . The type of reflection that carries spectral information of the color of the surface is the diffusive type, while the specular type does not, since it carries only white light. The spectral reflectance is measured as a percentage of the energy reflected (E_R) over the energy incident (E_I):

$$\rho_\lambda = \frac{E_R(\lambda)}{E_I(\lambda)} = \frac{\text{energy of wavelength } \lambda \text{ reflected from the object}}{\text{energy of wavelength } \lambda \text{ incident upon the object}} \times 100 \quad (3)$$

The spectral reflectance of many objects is graphed as function of the wavelength, these graphs are called spectral reflectance curves. They are useful since they provide spectral characteristics of the object

that could be surveyed and allow to choose the correct wavelength region for the acquisition of the remote sensed data.

7.3. Multispectral technology

Multispectral technology is an application of the remote sensing. Remote sensing can be both “active”, i.e. when the signal is emitted by an external artificial source (laser, microwave), or “passive”, i.e. when the solar radiation reflected by the object or the electromagnetic energy emitted by the object itself are registered by the sensor.

Multispectral imaging is a “passive” technology. As previously stated, it acquires the electromagnetic energy of the Sun reflected by a certain object, or emitted by it, through the use of a sensor, which can be put on satellite or an airborne vehicle.

Once the information has been obtained, it is processed and the object can be recognized analyzing its spectrum, and matching it with its equivalent, present in databases. For example, the green grass has a precise reflectance spectrum, since it absorbs certain wavelengths (around $0.45\ \mu\text{m}$ and $0.65\ \mu\text{m}$, i.e. red) and reflects others (around $0.55\ \mu\text{m}$, i.e. green), as shown in [Figure 7.4](#).

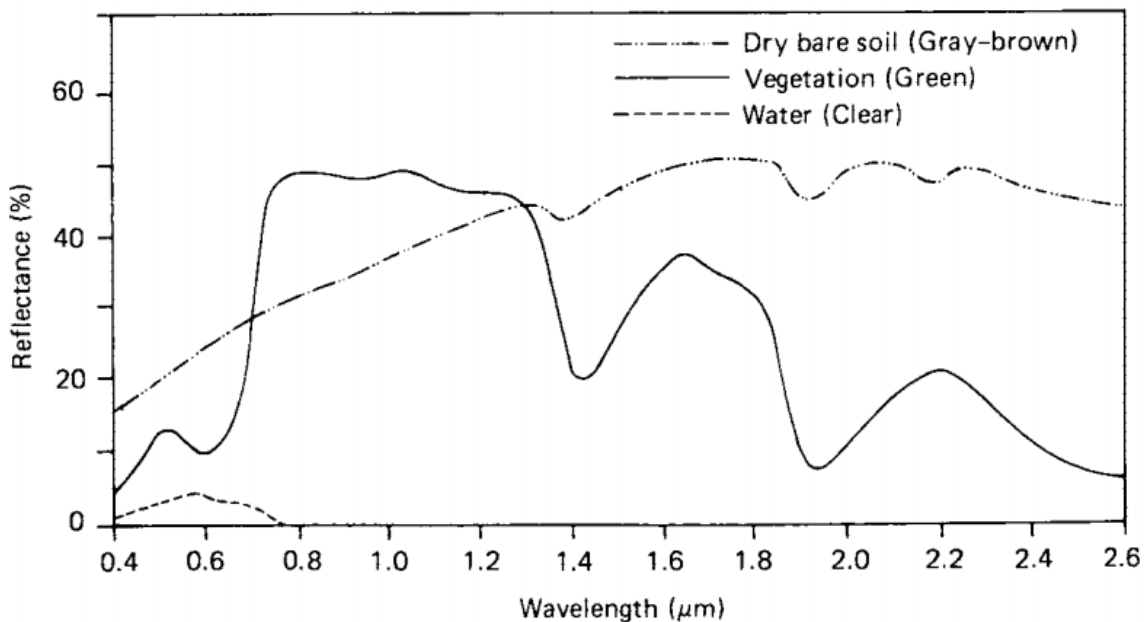


Figure 7.4. Average reflectance spectrum of three different objects with different spectral characteristics: dry bare soil, green vegetation and clear water. Source: Lillesand et al. (1994).

Multispectral technology uses a finite number of spectral bands, typically from 3 (RGB, i.e. visible) to 15 (RGB, SWIR – short wave infrared and LWIR – long wave infrared); while other type of techniques, hyperspectral and ultraspectral imaging, use a much higher number of bands, as shown in [Figure 7.5](#).

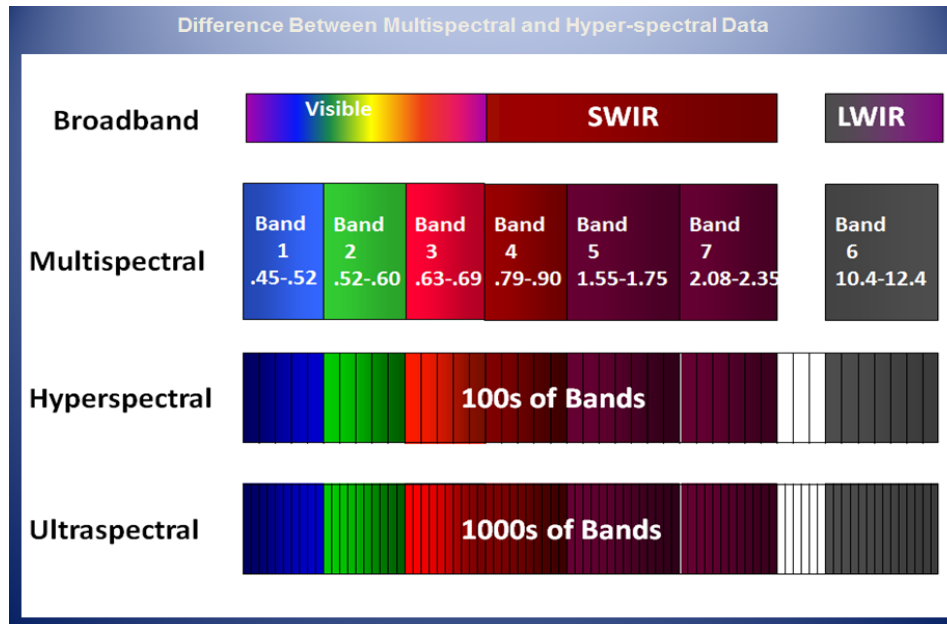


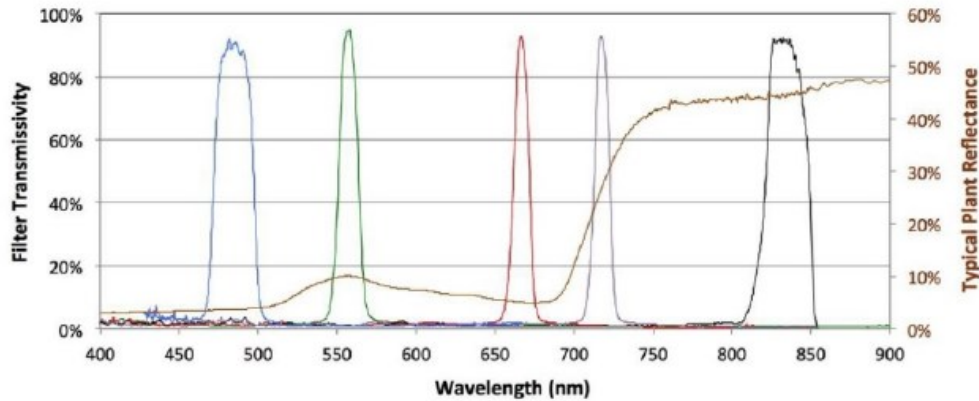
Figure 7.5. Acquisition bands of three different passive remote sensing technologies.

7.4. Description of the surveys and methodology used

The experimental multispectral survey has the aim of detecting possible water leaks in the levee, in a way that saves time and resources, with respect to the traditional visual inspection. This can be done through the evaluation of vegetation vigor; where area with a high vigor which are near to area with a much lower vigor can be a symptom of possible water leaks.

The instrumentation used in the an aero-photogrammetric survey is a RPV (Remotely Piloted Vehicle), mounted with the multispectral camera MicaSense RedEdge™ 3, which can acquire images over 5 bands (475-840 nm): Blue, Green, Red, Red Edge and NIR, with a dimension of 1280x960 pixels, saved in .tiff format. In [Figure 7.6](#) are described the characteristics of spectral acquisition of the camera.

Spectral Bands



Band Number	Band Name	Center Wavelength (nm)	Bandwidth FWHM (nm)
1	Blue	475	20
2	Green	560	20
3	Red	668	10
4	Near IR	840	40
5	Red Edge	717	10

Figure 7.6. Specifics on the spectral bands detected by the MicaSense RedEdge™ 3 camera.

For the tridimensional reconstruction of the surveyed area, from 5 to 13 georeferenced Ground Control Points (GCPs) have been used, each measured with a topographic GPS Stonex S9 III working in Network Real Time Kinematic (NRTK), connected to the Real Time Kinematic (RTK) network SmartNet ItalPoS by Leica Geosystems through GSM. Each GCP has been measured with centimetric precision, in the coordinate system WGS84 UTM 32 Norm (EPSG: 32632). The height of each GCP is ellipsoidal, measured in datum WGS84 (EPSG:4326).

Each flight followed the same path, described in [Figure 7.7](#), in which a longitudinal and transversal overlap of the footprint of the 80% has been maintained, which will allow a high quality photogrammetric reconstruction of the surveyed area.

The sensor has not been radiometrically calibrated, so it wasn't possible to obtain radiance data from the acquired images, but only the Digital Number (DN) for each pixel.

The resolution of the pixel was 0.3175 m; the mean altitude of the flights was 100 m (ellipsoidal altitude).

The dates in which the flights have been performed are:

- The 26th of May 2017, at 1 p.m.;
- The 18th of July 2017 at 12 a.m.;
- The 19th of July 2017 at 8 a.m.;
- The 6th of April 2018 at 3 p.m.



Figure 7.7. Representation of the RPV's flight plan.

8. Photogrammetric reconstruction of the survey

In this chapter the fundamental principles of photogrammetry will be treated, focusing on aerial photogrammetry and analytic reconstruction. Following that, the method used to calculate the DEMs and the orthophotos of the surveyed area will be described.

8.1. Introduction to photogrammetry

Photogrammetry is a science that allows to determine the tridimensional position of objects in the real surface starting from photos and therefore to allow measurements of them.

The photogrammetric principle states that to each tridimensional object's point P, Q, \dots (*object space*) corresponds a homologous point P', Q', \dots on the photograph (*image space*). Then, if a photograph is approximated to a central perspective, the image points and object points are connected by segments that meet in a point C , few centimeters distant (*focal length*) from the image space, called *projection center*.

To determine the real position of the objects from the points in the photograph it's necessary to define geometric relationships between the tridimensional position of the object's points and those of its image on the photograph. Since from a single photo can be obtained only 2D information, it's necessary to have two or more photographs of the same object taken from different positions (Figure 8.1), the so-called *stereoscopic vision*. The point P is geometrically defined if the spatial position of image points P' and P'' and their focal length f are known, because, as previously stated, it is the intersection of the projecting rays that connect the image points with their correspondent projection centers.

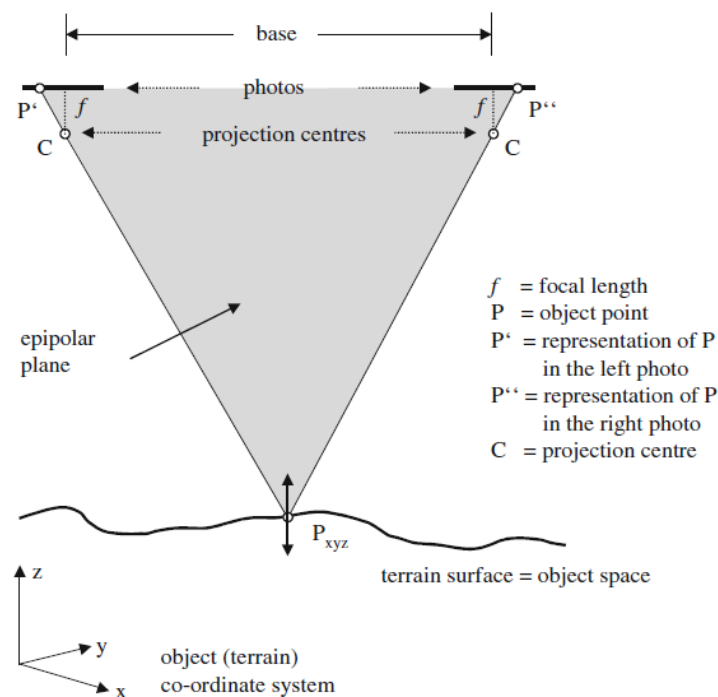


Figure 8.1. Geometry of a stereoscopic model in aerial photogrammetry⁶.

⁶ Linder, W. (2016). Digital photogrammetry – A practical course. Springer. pag. 2.

The positions of the projection centers and the orientation of the image space are not usually known a priori. However, it is possible to obtain this information from the photographs, if they contain a certain number of points of support on the ground (GCP), whose positions are derived from traditional topographic operations, as described in Section 6.3.

Today the photogrammetric problem is solved by obtaining the coordinates from the intersection in the space of the projecting rays with the resolution of a system of equations (*collinearity equations*) obtained from relationships of analytical geometry; while in the past the same operations were carried out with mechanical instruments (or optical) of analogic type, which made it possible to establish the position of the generic point P within a small-scale reconstructed object space, called the model.

8.2. *Orientation of the photograph*

To obtain a correct final product, it's necessary to calculate two different types of orientation: interior and external orientation.

The *interior orientation* is necessary to define the position of the projection center C with respect to the image plane. To perform this orientation is necessary to know those parameters that allow the calculation of the projecting rays of the image in a central projection. These parameters are peculiar of each camera. Therefore, they will be equal for each image taken during the surveys.

To define the position of C it is necessary to set two axes (x, y) on the plane of the image, which are materialized by four (or eight) fiducial marks fixed on the edges of the frame at the time of taking, and a z-axis normal to the plane of the plate. The coordinates of the projection center and the focal length are precisely measured and supplied by the manufacturer.

The projection center of the camera, theoretically, should be realized in such a way that the perpendicular from C to the image plane (called *principal point* P) falls in the origin of the xy system of the image plane, which is the intersection of the lines connecting the fiducial marks. But since this doesn't occur perfectly during the construction of the camera, the principal point P will deviate few hundredths of millimeter from the origin. Thus, the manufacturer of the camera will provide the measures of this deviation (x_P and y_P).

In [Figure 8.2](#) are exemplified the parameters necessary for perform the interior orientation.

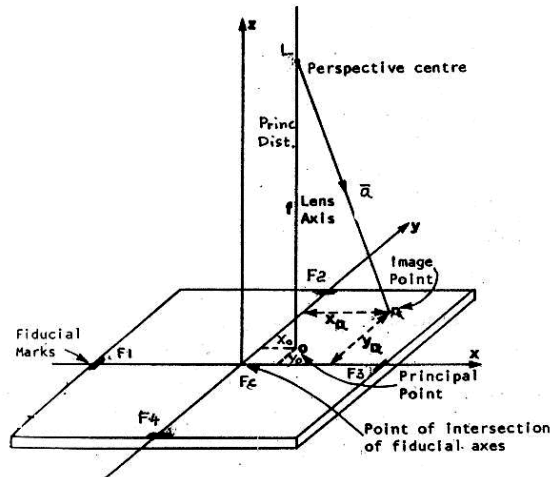


Figure 8.2. Interior orientation of a camera⁷.

For a correct interior orientation, it is also needed to correct the errors of the optic system, which creates deformations in the image. These deformations are constant over a certain configuration of the camera, and they can be corrected by knowing the position of the principal point P in the image plane, the principal distance and the distortion curve of the objective.

The *external orientation* consists in positioning the two or more photographs in the same spatial projection, which they had during the taking of the photos. For each photograph is necessary to determine a number of parameters equal to the movements that a rigid object can perform in the space, i.e. three rotations and three translations. These six parameters can be:

- The 3 coordinates of the projection center C;
- The 3 rotational angles of the camera during the flight, i.e. roll (rotation around x), pitch (rotation around y) and yaw (rotation around z).

To perform the reconstruction of each stereoscopic model, all constituted by two photos, it is necessary to determine $6+6=12$ parameters; these parameters can be defined through homologous points of the object and through some support point located over the terrain surface, the GCPs, which are present in both photographs.

Practically, this operation is performed through the solution of a system of equations by a software. Moreover, it is carried out in two steps, called: *relative orientation* and *absolute orientation*.

Relative orientation consists in the determination of five parameters which define the relative position of the camera at the moment in which the first photograph was taken, with respect to the position of the camera when the second photograph was taken.

While *absolute orientation* consists in the determination of seven parameters (i.e. rotation (3), translation (3) and factor scale (1)), which are necessary to calculate the exact position of the target object in the space.

⁷ Khalfā, A. Z., Alwan, I. A. K., & Jameel, A. (2013). Establishment of 3D Model With Digital Non-Metric Camera in Close Range Photogrammetry. *Engineering and Technology Journal*, 31(8 Part (A) Engineering), 1601-1611.

8.3. *Aerial triangulation*

In the description of the external orientation, it has been stated that for each stereoscopic model (i.e. 2 photos) are necessary at least 5 GCP, which are a big burden, in time and money, if an area of few hectares must be surveyed, since each GCP must be measured either with traditional topographic measurements or with GPS. To solve this problem, it has been developed the so-called *aerial triangulation*, which consists in considering the sequence of stereoscopic models as unique, for which orientation are necessary only few GCP. This method was made possible thanks to the analytic photogrammetry, since to solve the equations are necessary huge computational resources.

The steps necessary to perform the external orientation through aerial triangulation are:

- a) Creation of a block of stereoscopic models, for which the relative orientation is performed. For this operation, as previously stated, no GCPs are needed;
- b) Each model present in the block is connected to the following one thanks to common points;
- c) A single big model is created, whose absolute orientation is obtained with at least 5 GCPs; to maintain the errors of positioning small it's suggested to distribute them around the surveyed area;
- d) Once the big model has been oriented, also the single models have been oriented; this allows to identify different points on the surface and obtain their absolute coordinates analytically.

8.4. *Photogrammetric restitution of the surveys*

In the following sections will be described the steps performed for the photogrammetric reconstruction of the multispectral surveys. It consists of three main steps: importing and aligning the photos, creating a thin cloud of points; optimizing the parameters of the camera and building a dense cloud of points; creating a mesh and a texture from the dense cloud and finally restitution of a high-quality DEM and an orthophoto, which will have the data of the five acquisition bands.

8.4.1. *Import and alignment of the photos*

The data obtained by the multispectral camera during the different flights have been used to build the DEMs and the orthophotos of the surveyed area, with the software PhotoScan Professional 1.4.3 by Agisoft. To reach these final results the data (i.e. the photos) needed to be processed.

Firstly, the images of the survey, one for each acquisition band, have been imported. The software is able to create a single photo with the data of the 5 different bands; this feature allows to compute one fifth of the cameras, saving computing time and requesting lower processing capacity of the computer. The quality of the images has been analyzed and those with a quality lower than 0.6 have been removed. The value of this parameter is calculated on the sharpness of the part of the photo which is more focused.

The cameras have been imported in the coordinate system WGS84. Each photo in its metadata has memorized the location in which was taken, thanks to a GPS device mounted on the RPV.

The photos have been aligned: the software detects the position of the camera and create the model of the surveyed area with a sparse cloud, which is made of interest points, which are in common in the different images. An algorithm detects these interest points, called *descriptors*, which are stable and can be identified and distinguished in more photos. Each *descriptor* is univocal because of its own radiometric characteristics and for those of the surroundings; moreover, each *descriptor* is a bond between different images, as shown in Figure 8.3, where the “valid points”, with respect to the parameters set, of image IMG_0000_1, which are in common with image IMG_0038_1, are connected with a blue line, while those invalid, that won't be used in the reconstruction, are connected by a red line.

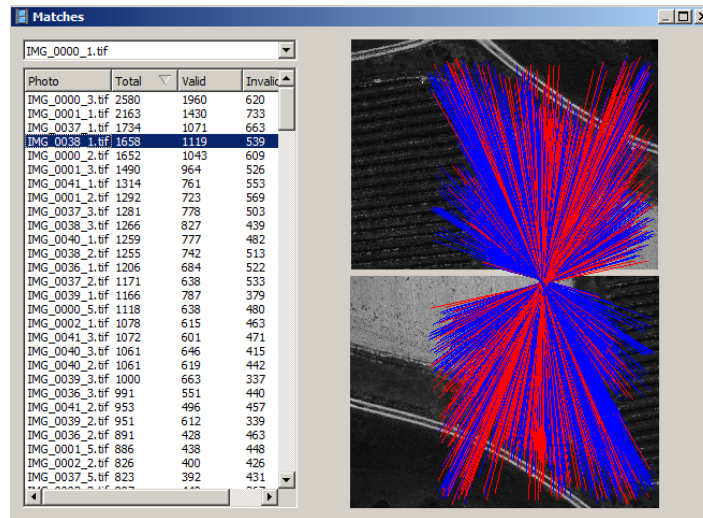


Figure 8.3. Example of valid (blue line) and invalid (red line) match points in two different images.

Once the bond points have been identified, Photoscan will solve the *collinearity equations*, as already mentioned in Section 3.1. These equations are used in photogrammetry to relate the geometry of the image taken from the camera and the real ground geometry:

$$x = -f \frac{a_1(X - X_0) + a_2(Y - Y_0) + a_3(Z - Z_0)}{a_7(X - X_0) + a_8(Y - Y_0) + a_9(Z - Z_0)} \quad (4)$$

$$y = -f \frac{a_4(X - X_0) + a_5(Y - Y_0) + a_6(Z - Z_0)}{a_7(X - X_0) + a_8(Y - Y_0) + a_9(Z - Z_0)} \quad (5)$$

Where (X_0, Y_0, Z_0) are the coordinate of the projection center; (X, Y, Z) are the coordinates of the ground reference system; (x, y, z) are the internal coordinates (i.e. of the photo); f is the focal length of the lens; a_1 to a_9 are constants calculated as follows:

$$\begin{pmatrix} a_1 & a_2 & a_3 \\ a_4 & a_5 & a_6 \\ a_7 & a_8 & a_9 \end{pmatrix} = \begin{pmatrix} 1 & 0 & 0 \\ 0 & \cos \omega & \sin \omega \\ 0 & -\sin \omega & \cos \omega \end{pmatrix} \begin{pmatrix} \cos \varphi & 0 & -\sin \varphi \\ 0 & 1 & 0 \\ \sin \varphi & 0 & \cos \varphi \end{pmatrix} \begin{pmatrix} \cos \kappa & -\sin \kappa & 0 \\ \sin \kappa & \cos \kappa & 0 \\ 0 & 0 & 1 \end{pmatrix} \quad (6)$$

Where ω , φ , κ are the rotation angles (roll, pitch, and yaw) around the coordinate system of the projection center. These equations are solved by the software for each image having at least 3 GCP.

Photoscan allows a selection of feature in the alignment parameters:

- *Quality*: highest, high, medium, low. The parameter has been set to high, which allows an analysis of the images at full scale;
- *Key point limit*: maximum number of points extracted from each photo. Set to 50'000;
- *Tie point limit*: maximum number of “tie points” identified for each couple of images. Set to 4'000; this means that even if 10'000 tie points are identified, only 4'000 with the probability of the best *matching* are used.

In case of bad alignment, a realignment will be performed, preceded by a manual matching procedure of the GCPs on the different photos ([Figure 8.4](#)). It's needed to fix in at least two photos the same GCP, in this way the software will be able to perform a correct alignment.



Figure 8.4. The GCP (T121) is manually moved to the center of the panel where the coordinates of the GCP were taken.

The final result is the sparse cloud of point, as shown in [Figure 8.5](#).

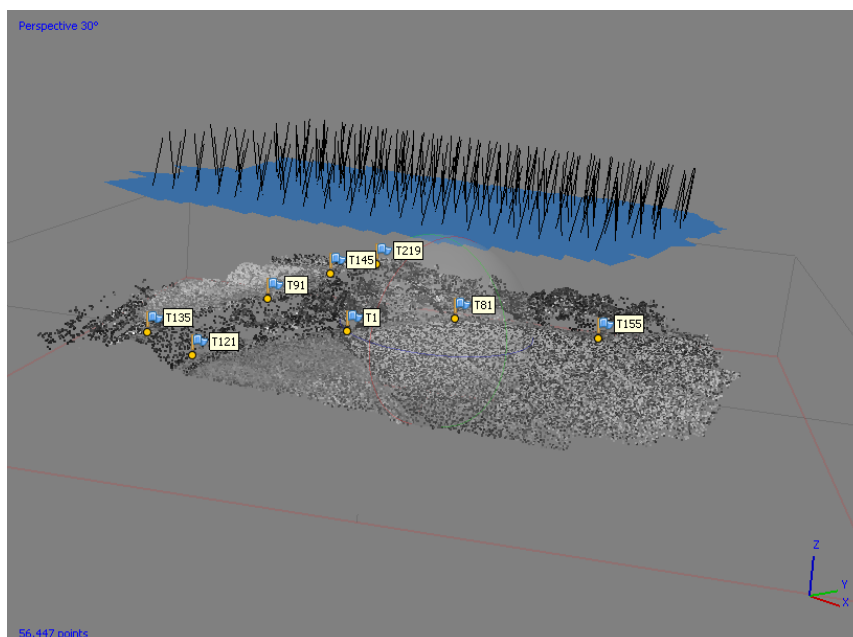


Figure 8.5. Workspace from Photoscan Professional Pro representing the sparse cloud of point with GCP.

8.4.2. Dense Cloud

Before processing the dense cloud, the calibration parameters of the camera have been optimized, through the appropriate function “Optimize cameras”. The parameters are the following:

- f : focal length;
- c_x, c_y : coordinates of the principal points, which are the coordinates of the intersection between the sensor plane and the axis of the optical lens (as explained in Section 3.2);
- k_1, k_2, k_3, k_4 : coefficients of affinity and skew transformation;
- p_1, p_2 : coefficients of tangential distortion;
- b_1, b_2 : coefficients of radial distortion.

This procedure is aimed at decreasing the positioning error.

The next step is the creation of the dense cloud of points, which is a tridimensional reconstruction of the area, with a high density of points. Through the use of *image matching* algorithms and again solving the collinearity equations for each pair of photos, Photoscan is able to create a depth map for each photo, which assigns a relative depth value to each pixel in the image. Subsequently, the dense cloud, thanks to the previously done alignment, is built (Figure 8.6). Again, Photoscan allows to select some features:

- *Quality*: specifies the quality of the tridimensional reconstruction and especially the geometry. It has been set to high;
- *Filtering depth*: during the creation of the depth maps, some errors can be generated, due to the bad quality of some pixels. The filtering algorithms of Photoscan can solve the errors. The depth of filtering has been set to Moderate or Mild, to maintain a good quality of the geometry.

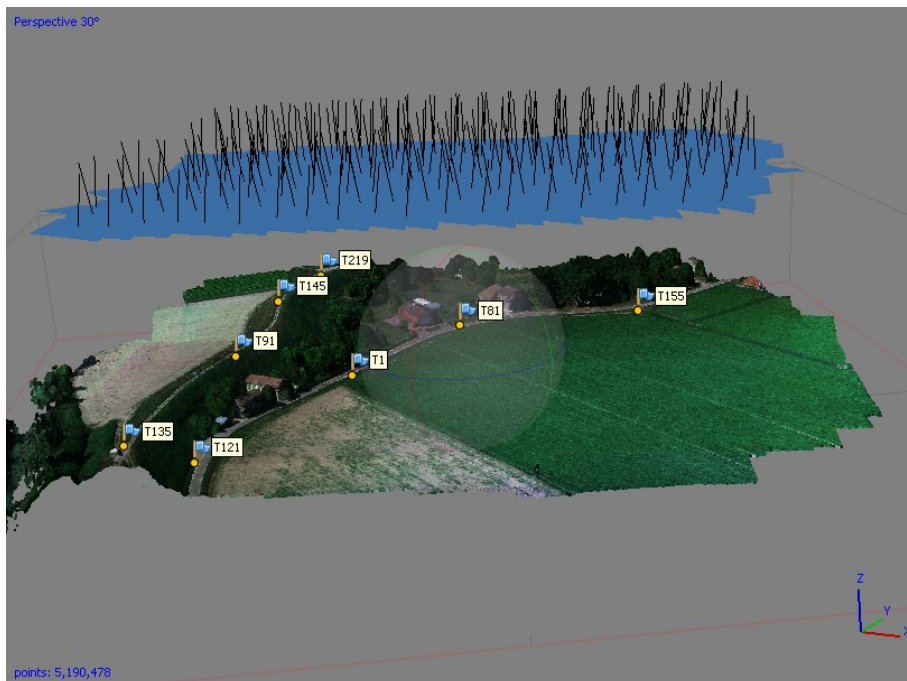


Figure 8.6. Workspace from Photoscan Professional Pro representing the dense cloud of point with GCPs.

8.4.3. Mesh and Texture

From the dense cloud is possible to generate a *mesh*, which is a surface made of triangles that connects the points of the cloud. The mesh has been created with a surface type called “Height field”, suited for territorial purposes. The surface created is a 2.5D type, which is characterized by a single value of height for each point on the plane. The number of faces has been set to “high”. The interpolation has been set to “enabled”, in this way the software will interpolate some areas within a certain radius around the points of the dense cloud.

Once obtained the mesh (Figure 8.7), it can be computed the *texture* that will be superimposed to it. “Texturizing” a mesh means to apply a color content to the mesh. The texture (Figure 8.8) has been computed in modality “orthophoto”, which will texturize the area orthographically, i.e. with a low quality of the vertical surfaces. The values of the pixels from the different photos have been combined in the “Mosaic” modality, which consists in creating a continuous background with the low frequency components (i.e. low detailed features) and selecting the high frequency components, from images with nadiral position with respect to the processed area, to generate the details.

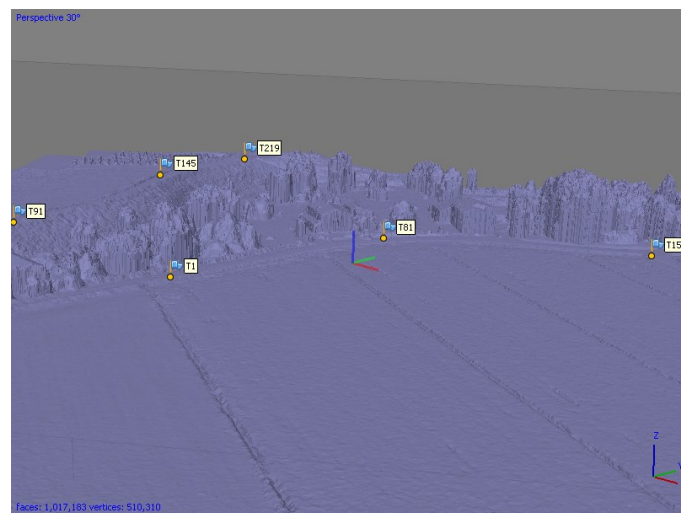


Figure 8.7. Workspace from Photoscan Professional Pro representing a part of the polygonal mesh with GCPs.

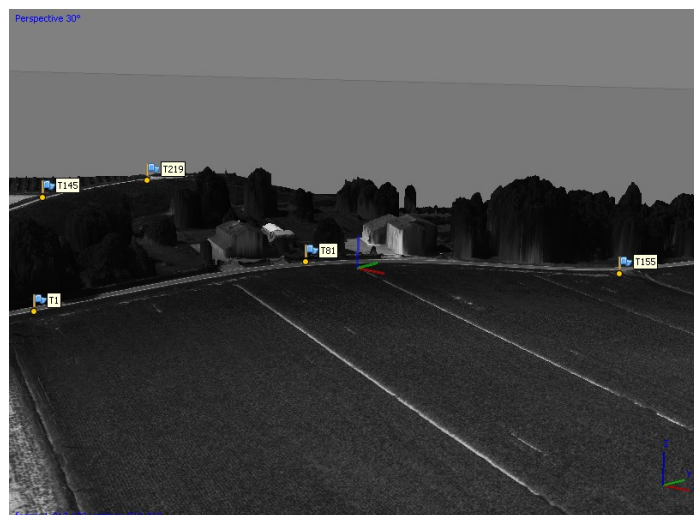


Figure 8.8. Workspace from Photoscan Professional Pro representing a part of the textured polygonal mesh with GCP.

8.4.4. DEM and Orthophoto

Finally, from the 3D model obtained it's possible to generate the DEM (Figure 8.10) and the orthophoto (Figure 8.9) and extract them in .tiff format, necessary for the analysis of the area in a GIS software. Each orthophoto is exported with the 5 spectral channels. Both the DEMs and the ortophotos have been exported in the coordinate system WGS84/UTM 32N



Figure 8.9. Orthophoto of the 26/05/2017 survey, with GCPs.

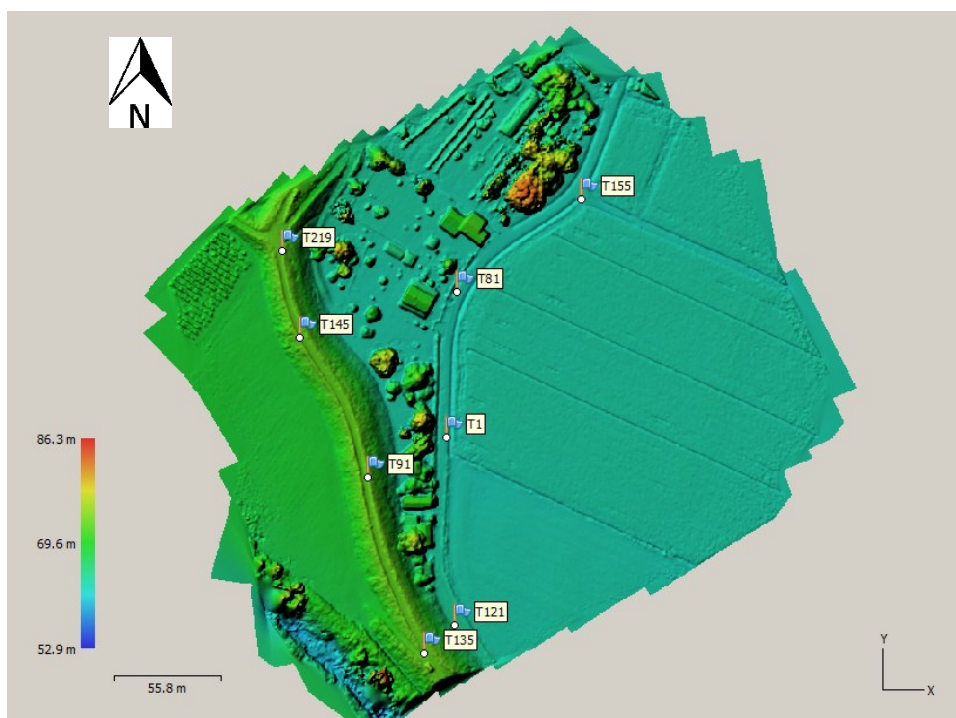


Figure 8.10. Digital Elevation Model of the 26/05/2017 survey, in Ellipsoidal height. With GCPs.

8.4.5. Results of the photogrammetric models

In the following tables the results of the photogrammetric reconstruction are summarized.

Table 1. Average camera location error. X – Longitude, Y – Latitude, Z – Altitude.

	X error (m)	Y error (m)	Z error (m)*	XY error (m)	Total (m)
Survey of 26/05/2017	0.835292	1.34913	43.5459	1.58678	43.5748
Survey of 18/08/2017	1.10247	1.22526	41.4622	1.64824	41.495
Survey of 19/09/2017	1.30831	0.730848	39.6722	1.4986	39.7005
Survey of 06/04/2018	1.07835	1.13258	43.6822	1.56384	43.7102

*Z error represent the comparison between the absolute ellipsoidal height recorded by the GPS mounted on the drone and of the GCPs.

Table 2. Survey of 26/05/2017. Ground control points mean root square error*. X – Longitude, Y – Latitude, Z – Altitude.

Survey of 26/05/2017					
Count	X error (cm)	Y error (cm)	Z error (cm)	XY error (cm)	Total error (cm)
8	0.969054	0.850959	2.55657	1.28965	2.86343
Label	X error (cm)	Y error (cm)	Z error (cm)	Total error (cm)	Image (pix)**
T219	0.21951	-0.00768862	-0.183752	0.286372	0.214 (3)
T135	0.574839	- 2.02151	-2.81652	3.51421	0.057 (3)
T91	0.909118	0.944688	-1.99393	2.38636	0.111 (3)
T1	-1.99641	0.248914	-5.1627	5.54086	0.238 (4)
T121	-0.624167	0.826541	2.94017	3.11727	0.096 (4)
T155	0.665264	0.0777367	-1.52217	1.66301	0.187 (4)
T81	-1.07234	-0.0578929	1.6455	1.96492	0.201 (4)
T145	0.582812	-0.244022	-0.153072	0.650114	0.165 (4)
Total	0.969054	0.850959	2.55657	2.86343	0.172

*RMS error = $\sqrt{\sum_{i=1}^n [(X_{i,est} - X_{i,in})^2 + (Y_{i,est} - Y_{i,in})^2 + (Z_{i,est} - Z_{i,in})^2]} / n$

(X, Y, Z)_{i,in} are the input value for (X, Y, Z) coordinates for i camera position;

(X, Y, Z)_{i,est} are the estimated value for (X, Y, Z) coordinates for i camera position.

**Error in pixels shows average reprojection error for tie points present on each photo. Error lower than 0.8 corresponds to good quality model⁸.

⁸ Agisoft, L. L. C. (2018). Agisoft PhotoScan user manual: professional edition, Version 1.4.

Table 3. Features of the reconstruction parameters of the survey of 26/05/2017.

General	
Number of cameras	1205
Flying altitude	101 m
Ground resolution	6.71 cm/pix
Reprojection error	0.613 pix
Coverage area	0.0831 km ²
Point Cloud	
Points	416'297
RMS reprojection error	0.194292 (0.612951 pix)
Average tie point multiplicity	21.9071
Dense Point Cloud	
Points	5'173'281
3D Model	
Faces	1'0161'470
Vertices	509'778
DEM	
Resolution	13.4 cm/pix
Point density	55.6 points/m ²

Table 4. Survey of 18/07/2017. Ground control points mean root square error. X – Longitude, Y – Latitude, Z – Altitude.

Survey of 18/07/2017					
Count	X error (cm)	Y error (cm)	Z error (cm)	XY error (cm)	Total error (cm)
5	0.43184	0.381102	1.14155	0.575955	1.27862
Label	X error (cm)	Y error (cm)	Z error (cm)	Total error (cm)	Image (pix)
11	-0.224722	-0.259359	1.0582	1.11246	0.158 (5)
61	0.236099	-0.160706	-1.18277	1.21676	0.243 (5)
91	0.76591	0.65428	-1.44896	1.76471	0.229 (5)
145	-0.251229	-0.127031	1.16747	1.20094	0.194 (5)
187	-0.420061	-0.434605	-0.731083	0.948586	0.185 (4)
Total	0.43184	0.381102	1.14155	1.27862	0.205

Table 5. Features of the reconstruction parameters of the survey of 18/07/2017.

General	
Number of cameras	1040
Flying altitude	102 m
Ground resolution	6.85 cm/pix
Reprojection error	0.629 pix

Coverage area	0.09 km ²
Point Cloud	
Points	481'731
RMS reprojection error	0.157959 (0.629271 pix)
Average tie point multiplicity	5.68934
Dense Point Cloud	
Points	5'603'386
3D Model	
Faces	1'105'750
Vertices	554'216
DEM	
Resolution	13.7 cm/pix
Point density	53.2 points/m ²

Table 6. Survey of 19/07/2017. Ground control points mean root square error. X – Longitude, Y – Latitude, Z – Altitude.

Survey of 19/07/2017					
Count	X error (cm)	Y error (cm)	Z error (cm)	XY error (cm)	Total error (cm)
8	0.960185	0.679127	1.94492	1.17608	2.27286
Label	X error (cm)	Y error (cm)	Z error (cm)	Total error (cm)	Image (pix)
T31	0.694038	-0.826352	3.56707	3.72673	0.200 (4)
T241	-0.228302	-0.686036	-0.631242	0.959809	0.223 (8)
T187	1.78344	0.97659	-1.88856	2.77508	0.266 (10)
T145	-0.143445	0.778454	2.18391	2.32294	0.253 (8)
T91	-0.6126	-0.683791	-0.021548	0.918321	0.230 (11)
T61	0.482624	0.0356012	-0.39918	0.627326	0.250 (16)
T11	-1.74087	-0.67067	0.20908	1.87727	0.144 (16)
T287	0.0418427	0.24053	-2.93252	2.94266	0.138 (8)
Total	0.960185	0.679127	1.94492	2.27286	0.216

Table 7. Features of the reconstruction parameters of the survey of 19/07/2017.

General	
Number of cameras	955
Flying altitude	99.9 m
Ground resolution	6.72 cm/pix
Reprojection error	0.617 pix
Coverage area	0.0906 km ²
Point Cloud	
Points	369'022
RMS reprojection error	0.166353 (0.617031 pix)

Average tie point multiplicity	8.04561
Dense Point Cloud	
Points	5'651'299
3D Model	
Faces	1'111'742
Vertices	557'360
DEM	
Resolution	13.4 cm/pix
Point density	55.3 points/m ²

Table 8. Survey of 06/04/2018. Ground control points mean root square error. X – Longitude, Y – Latitude, Z – Altitude.

Survey of 06/04/2018					
Count	X error (mm)	Y error (mm)	Z error (mm)	XY error (mm)	Total error (mm)
13	3.80167	2.32362	8.38828	4.45555	9.49817
Label	X error (mm)	Y error (mm)	Z error (mm)	Total error (mm)	Image (pix)
A1	2.51786	-0.158529	2.29009	3.40723	0.034 (4)
A2	3.54495	1.10044	-27.5319	27.781	0.022 (2)
A3	0.766212	-1.46035	2.04978	2.63083	0.025 (4)
A4	-1.00931	3.78392	-6.33181	7.44503	0.073 (3)
A5	5.12055	-1.03167	-1.07383	5.33268	0.035 (10)
A6	6.20149	-3.8933	2.97601	7.90398	0.042 (5)
S1	-0.666414	-1.78178	-2.472	3.11876	0.120 (7)
S2	-5.40414	3.34506	-2.77846	6.93642	0.151 (6)
S3	-0.666414	2.20657	-4.67575	5.21303	0.074 (4)
S4	-7.15035	2.08059	0.342404	7.45477	0.035 (4)
S5	3.57276	-2.26369	-1.72275	4.56692	0.017 (3)
S6	-2.89312	2.72587	6.26103	7.41626	0.028 (3)
S7	0.58593	-0.405259	-4.38078	4.43826	0.022 (7)
Total	3.80167	2.32362	8.38828	9.49817	0.071

Table 9. Features of the reconstruction parameters of the survey of 06/04/2018.

General	
Number of cameras	1360
Flying altitude	98.2 m
Ground resolution	6.64 cm/pix
Reprojection error	0.574 pix
Coverage area	0.168 km ²
Point Cloud	

Points	574'394
RMS reprojection error	0.165209 (0.574253 pix)
Average tie point multiplicity	5.66624

Dense Point Cloud	
Points	37'663'696

3D Model	
Faces	7'486'876
Vertices	3'747'555

DEM	
Resolution	6.64 cm/pix
Point density	227 points/m ²

9. Review on the Spectral Indexes used

The following sections will provide a review of the vegetation index (VI) used in this work, along with their positive and negative aspects. The spectral indexes consist in empirical relations between the different acquisition bands of the remote sensed data, with the aim of gathering information which are not directly available.

The VIs are mainly aimed at detecting the chlorophyll (Chl) content. Chl is a pigment present in vegetation which is essential for the conversion of the energy of light to chemical energy, which will be stored by the plants. Thus, the amount of solar radiation that is absorbed by the leaves is a function of the content of photosynthetic pigments, and consequently of Chl content. From this information is possible to estimate the vegetation status, where higher contents of Chl indicate an overall good condition of the plant, and vice versa.

Chl absorbs the red band of the electromagnetic spectrum and reflects the green one, and even if it has high reflectance in the blue region, this reflectance is not used because it overlaps with the absorbance of the carotenoids (Wu et al., 2008).

In [Table 10](#) is presented the list of the spectral indices used, their formulation and their reference.

Table 10. Definition and sources of the VIs used.

Index	Spectral Bands	Formula	Reference
CI _{Green}	NIR - Green	$\frac{\rho_{NIR}}{\rho_{green}} - 1$	Gitelson, 2003
CI _{Red-edge}	NIR - Red-edge	$\frac{\rho_{NIR}}{\rho_{RE}} - 1$	Gitelson, 2003
GDI	NIR - Red - Green	$\rho_{NIR} - \rho_{red} - \rho_{green}$	Vescovo, 2006
MSR	NIR - Red	$\frac{\rho_{NIR} - 1}{\rho_{red}}$ $\frac{\rho_{NIR}}{\sqrt{\rho_{red}}} + 1$	Chen, 1996
MSR _{Red-edge}	NIR - Red-edge	$\frac{\rho_{NIR} - 1}{\rho_{RE}}$ $\frac{\rho_{NIR}}{\sqrt{\rho_{RE}}} + 1$	Chen, 1996
NDVI	NIR - Red	$\frac{\rho_{NIR} - \rho_{red}}{\rho_{NIR} + \rho_{red}}$	Rouse et al., 1974
NDVI _{Red-edge}	NIR - Red-edge	$\frac{\rho_{NIR} - \rho_{RE}}{\rho_{NIR} + \rho_{RE}}$	Gitelson, 1994
NDWI	NIR - Green	$\frac{(\rho_{green} - \rho_{NIR})}{(\rho_{green} + \rho_{NIR})}$	McFeeters, 1996
SAVI	NIR - Red	$\frac{(1 + L) \cdot (\rho_{NIR} - \rho_{red})}{(\rho_{NIR} + \rho_{red} + L)}$	Huete, 1988

9.1. *Normalized Difference Vegetation Index*

The NDVI it's a remote sensing indicator, introduced by Rouse et al. (1973), which allows to detect the presence of vegetation over the surveyed area. This indicator is effective because it combines the values of the NIR and the red portion of the spectrum. The NIR, in fact, is reflected by the internal structure of the plants, where higher values of reflectance imply healthier plants. While the red portion of the spectrum is absorbed by Chl, which also in an indicator of the status of the plant.

$$NDVI = \frac{\rho_{NIR} - \rho_{red}}{\rho_{NIR} + \rho_{red}} \quad (7)$$

The formulation of NDVI combines the information of two different spectral bands into a single value, which ranges between -1 and +1 thanks to the negative sign on the numerator.

Therefore, values close to +1 are typical of healthy vegetation, values between -0.1 and +0.2 match with bare soils or buildings, and negative values beyond -0.1 are typical of surface water, because the NIR light is strongly absorbed by water and thus the red light reflected is higher than the NIR (Gao et al, 2014).

The main advantages of the NDVI indicator are:

- Monitoring of changes in vegetation growth along seasons;
- Detection of arid areas in extensive crop cultivation;
- Seepage detection: 1) in arid areas with little vegetation, high NDVI values may indicate vegetation that is receiving water from seepage. 2) Negative or near zero NDVI values outside the boundaries of a water body indicate presence of seepage;
- With the ratio is possible to reduce certain noises in the image, such as the difference of illumination, the shadow of clouds and the atmospheric attenuation present in multiple bands of multitemporal images (Huete et al., 2002);

It has also disadvantages:

- In case of satellite imagery, the NDVI value can be influenced by noise, such as the atmospheric path radiance (Huete et al, 2002);
- NDVI is sensitive to the canopy background, i.e. the soil visible through the canopy, especially for dark canopy background.
- It has been noticed that NDVI is not able to differentiate between medium/high and high Chl content. In fact, over for a Chl content higher than 200 $\mu\text{mol}/\text{m}^2$ it saturates, reaching value around 1.

9.2. *Normalized Difference Vegetation Index with Red Edge*

The red-edge is an abrupt increment in the reflectance spectrum of vegetation, occurring between the red and the NIR, from which the name. Its lower bound has been defined to be around 680 nm, while the upper bound can vary from species, from 740 nm to 800 nm. It is caused by the chlorophyll

absorption of red wavelengths, together with the internal scattering of the leaf which causes strong reflectance in the NIR region (Horler, 1983).

Gitelson et al., (1994) found a closer correlation between the index NDVI, which uses the red-edge instead of the red band, with Chl content, and a higher sensitivity to pigment changes in leaves.

Below, [Figure 9.1](#) Figure 9.1. Spectrum of reflectance of a fresh soy leaf (Hosgood et al. 1995), with red-edge zone highlighted in red. shows the typical reflectance spectrum of vegetation, with the red-edge band highlighted in red.

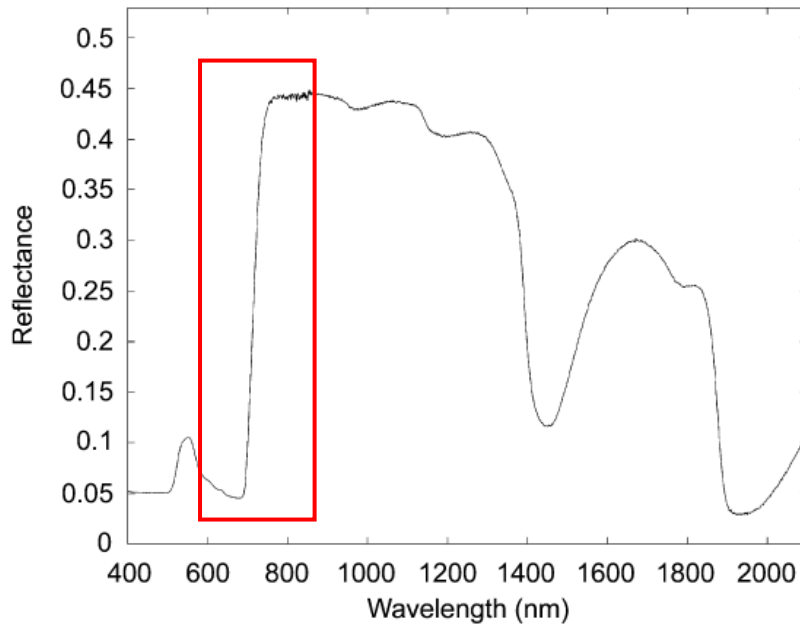


Figure 9.1. Spectrum of reflectance of a fresh soy leaf (Hosgood et al. 1995), with red-edge zone highlighted in red.

The index is calculated as following:

$$NDVI_{Red-edge} = \frac{\rho_{NIR} - \rho_{RE}}{\rho_{NIR} + \rho_{RE}} \quad (8)$$

9.3. Modified Simple Ratio and Modified Simple Ratio with Red Edge

The Modified Simple Ratio Index (MSRI), introduced by Chen (1996), is a non-linear combination of Q_{NIR} and $Q_{RED}/Q_{RedEdge}$. Chen demonstrated that thanks to this combination the noise in the signal decreases and the sensitivity is improved, with respect to SR. Sims and Gamon (2002), after comparing a large number of different types of leaves at different growth state, found that the MSR was the index that showed the best correlation with chlorophyll content.

The relationships to calculate the MSR and the MSR-RE are the following:

$$MSR = \frac{\frac{\rho_{NIR}}{\rho_{red}} - 1}{\sqrt{\frac{\rho_{NIR}}{\rho_{red}} + 1}} \quad (9)$$

$$MSR_{Red-edge} = \frac{\frac{\rho_{NIR}}{\rho_{RE}} - 1}{\sqrt{\frac{\rho_{NIR}}{\rho_{RE}} + 1}} \quad (10)$$

9.4. Green Difference Index

The Green Difference Index (GDI), introduced by Vescovo (2006) is aimed at the estimation of Green Ratio (GR), which is the percentage of the green biomass with respect to the total phytomass. and it has also been found to be more predictable than vegetation biomass. Furthermore, the relationship between GDI and GR is linear, and consequently there are no saturation problems, showed for example by the NDVI.

The relationship for GDI estimation is the following:

$$GDI = \rho_{NIR} - \rho_{red} - \rho_{green} \quad (11)$$

9.5. Green and Red-Edge Chlorophyll Index

The Chlorophyll Index (CI) was introduced by Gitelson et al. (2003). The index is used to calculate the total Chl content of the leaves. It has been designed to avoid the saturation problems, common to indexes that use the reflectance in the red range (around 680 nm), which consists in reaching the maximum value of the index (e.g. 1 for NDVI) for moderate Chl content. According to the research of Gitelson et al. (2003) NDVI became invariant for Chl content bigger than 100 $\mu\text{mol}/\text{m}^2$.

In [Figure 9.2](#) are exemplified the relationships between the index values and the Chl content, where it's clear that NDVI (top-left scatter plot) shows an asymptotic behavior for values equal to 1, while CI (bottom-right scatter plot) has a linear behavior.

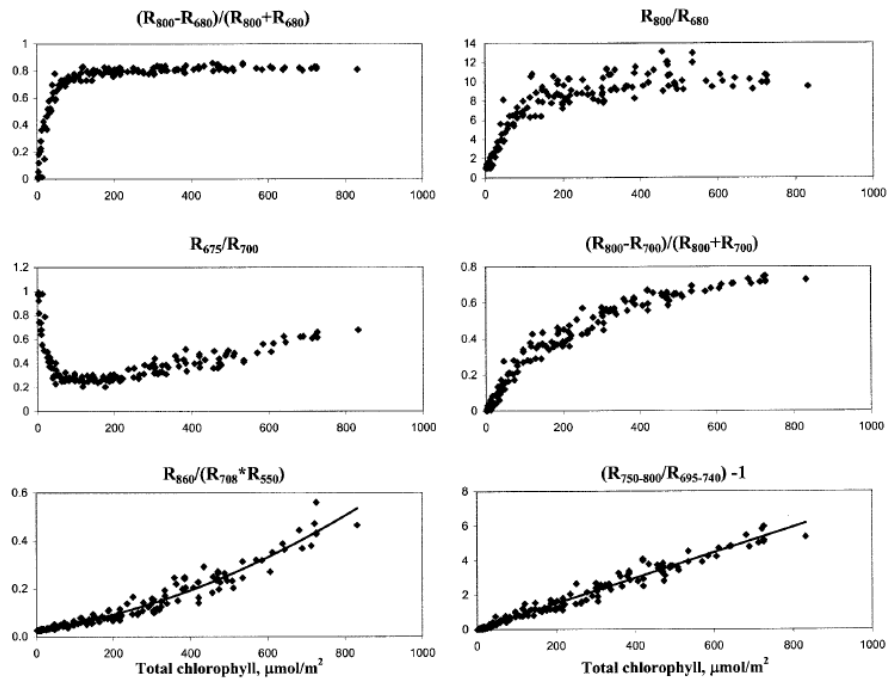


Figure 9.2. Scatter plots indicating the relationship between various reflectance indices and total chlorophyll content.

Source: Gitelson et al. (2003).

The relationships for calculating CI and CI-RE are:

$$CI = \frac{\rho_{NIR}}{\rho_{green}} - 1 \quad (12)$$

$$CI_{Red-edge} = \frac{\rho_{NIR}}{\rho_{RE}} - 1 \quad (13)$$

The reflectance in the NIR range and the visible range is caused by different processes. An increase in the NIR range reflectance might be caused by an increase in leaf thickness, or in the density of the canopy; while in the visible range, an increase indicates a lowering in the pigment content. For example, for leaves with the same Chl content, an increase in leaf thickness might lead to an increase in NIR reflectance and subsequently to a decrease in Chl concentration per volume, which means an increment of reflectance in the green and red-edge (Gitelson et al., 2003).

So, the CI and CI – RE, thanks to their formulation, have a good correlation with total Chl content.

9.6. Normalized Difference Water Index

The Normalized Difference Water Index (NDWI) was introduced by McFeeters (1996). This index has been formulated to detect water over the ground surface. It is calculated with the following expression:

$$NDWI = \frac{(\rho_{green} - \rho_{NIR})}{(\rho_{green} + \rho_{NIR})} \quad (15)$$

The principal characteristics of this index are that thanks to the green wavelengths recorded, it is able to maximize the green reflectance of water surfaces and to minimize the low reflectance of NIR thanks to the subtraction at the numerator.

The resultant values are higher than zero for water features, while bare soil or vegetation show values near or below zero. Xu (2006) highlighted the fact that the use of NDWI in built-up areas won't allow to achieve the expected results, since the water information get mixed with noise coming from the built-up land. Furthermore, values lower than zero indicate vegetation.

Since NDWI is the opposite of GNDVI (Green Normalized Difference Vegetation Index), for which the green band is subtracted to the NIR band in the numerator, those negative values can be interpreted following this index. In fact, Siegfried (2019) found a strong correlation between the value of GNDVI and soil moisture, detected by tensiometers during the earliest growth of vegetation (crop in particular). Therefore, bigger negative values of NDWI are indicative of areas with higher soil moisture.

It's important to mention here that another spectral index was named NDWI by Gao (1996). Unlike McFeeters' NDWI, Gao's NDWI uses NIR and Mid-Infrared Spectroscopy (MIR) to detect the liquid water inside vegetation:

$$NDWI_{GAO} = \frac{(\rho_{NIR} - \rho_{MIR})}{(\rho_{NIR} + \rho_{MIR})} \quad (16)$$

This index would have been extremely useful in the analysis of the area under exam, but the MIR are wavelengths detected by more complex sensors, such as the hyperspectral ones.

9.7. *Soil Adjusted Vegetation Index*

The NDVI and the RVI indexes well correlate with many vegetation parameters, such as green leaf area, biomass, photosynthetic activity and productivity. However, their main limitations are that they are influenced by atmospheric conditions and mostly by soil substrate, in case the vegetation is not dense. In fact, when the vegetation is sparse, a significant part of the radiant flux, in this case the NIR light, is passing through the canopy and is reflected by the soil. In case of dark soil, the spectral signal strongly resembles to vegetation spectral signature (Huete, 1988).

To solve this problem, Huete introduced the SAVI in 1988, which is formulated as following:

$$SAVI = \frac{(1 + L) \cdot (\rho_{NIR} - \rho_{red})}{(\rho_{NIR} + \rho_{red} + L)} \quad (17)$$

Where L is a factor related to the density of vegetation:

- $L = 1$ for the analysis of very low vegetation density;
- $L = 0.5$ for intermediate vegetation density;
- $L = 0.25$ for higher vegetation density.

Anyway, $L = 0.5$ was suggested by the author because it was found that it minimizes soil brightness noise and doesn't need calibration for different soils.

The main disadvantage related to this index is that it reduces the amplitude of the signal of the vegetation index with respect to the NDVI, anyway this problem is partially compensated by the fact that the soil and the vegetation are better defined.

10. Results of the Spectral Indexes

Before applying the VI formulas, a rough homogenization of the DN values has been performed, through which solve the absence of a calibration of the reflectance values. The homogenization consisted in using a survey as reference and obtaining a correction coefficient for every band of each survey. The coefficient is obtained from the interpolating line (linear) of six different points, taken along the road.

But since the results of this homogenization were not satisfactory, it has been decided to maintain the original data.

Thus, the data collected have been imported in a GIS environment, using the open source software QGIS. This is meant to interpret the information from the georeferenced photos of the aerial survey using the other data available from the experimental monitoring network and from other sources, such as rain gauges near the site. The position of the piezometers, of the penetrometric investigations and the sheet piles have been also imported. In [Figure 10.1](#) is presented the map of the area with the piezometer and the geognostic intervention locations, taken during the survey of April 2018 in the visible portion of the spectrum, which can help to have a comprehensive picture and it is also useful to detect possible water ponding with the bare eye.

With the Raster Calculator tool of QGIS is possible to calculate the fore-mentioned VIs, combining the different bands of each image.

Since the maps have different sizes, a mask, which is comprehensive of the biggest area in common to the different maps has been created to perform a coherent analysis of the values. Another mask, shown in [Figure 10.2](#), which covers approximately the area that should be crossed by the ancient riverbed, has been created to verify its position according to the geomorphological maps of Section 2.2 ([Figure 2.4](#)). It has been cut in the northern part, to adapt to the surveys of the 2017, which covered a smaller area.

The resulting maps for each VI have been imported in R Studio and confronted with a common scale. From the data, the histograms have also been derived, which can be useful for a quantitative interpretation.

The survey of April 2018 captured the largest area, those parts of the map that have been cut by the masks, but that could be useful to the study, will be treated later in a separate chapter.

In the following pages the two types of masks and the spectral maps for each index considered are presented.

The coordinates are expressed in the coordinate system WGS 84/UTM zone 32N.

The SAVI maps were not included in this chapter because they had results comparable to those of the NDVI maps. This is probably due to the presence of dense vegetation, where the soil is not visible (e.g. corn field), together with area where the soil, which is not dark, is well discriminated, without creating confusion in the reflectance.



Figure 10.1. Map of the survey in the visible spectrum, with geognostic interventions and piezometers position.

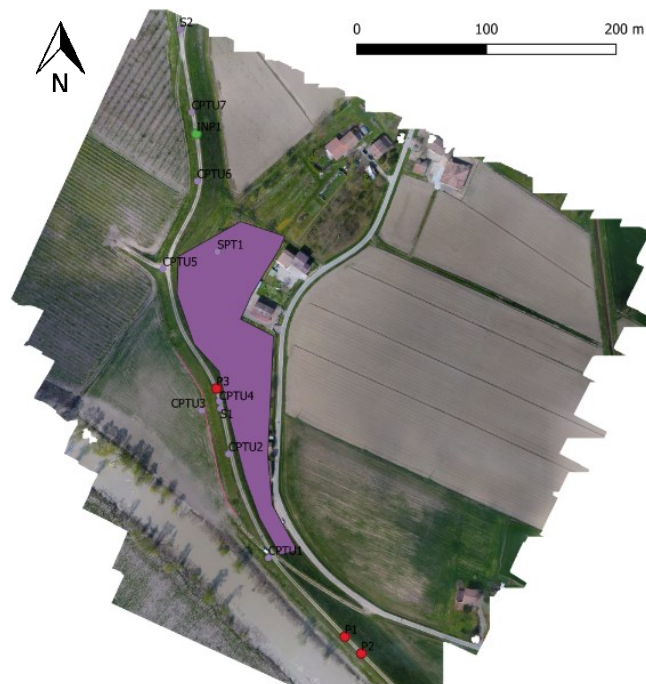


Figure 10.2. Map of the surveyed area along with the ancient riverbed mask (in violet).

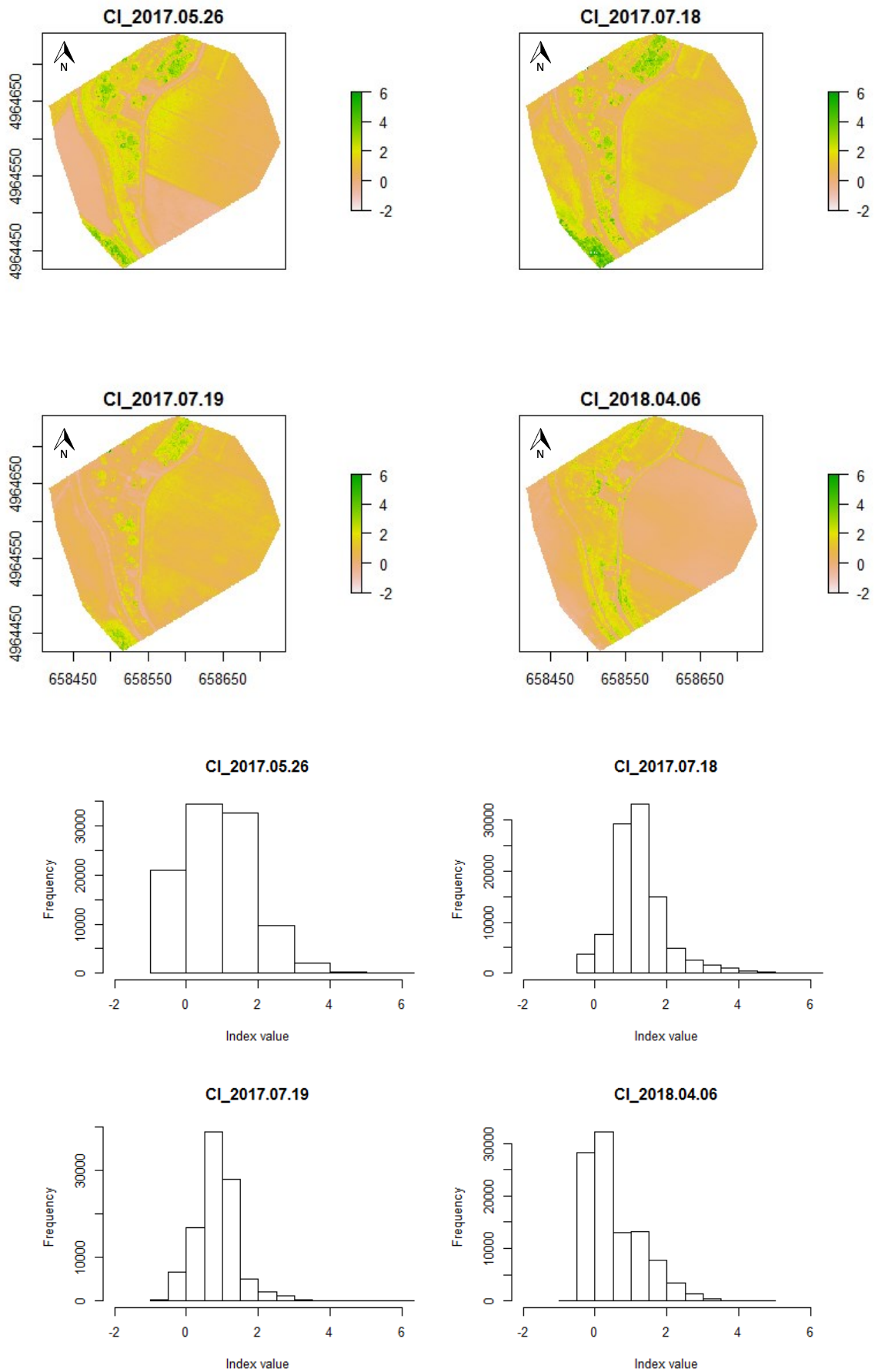


Figure 10.3. Maps and histograms of the four surveys expressed with CI.

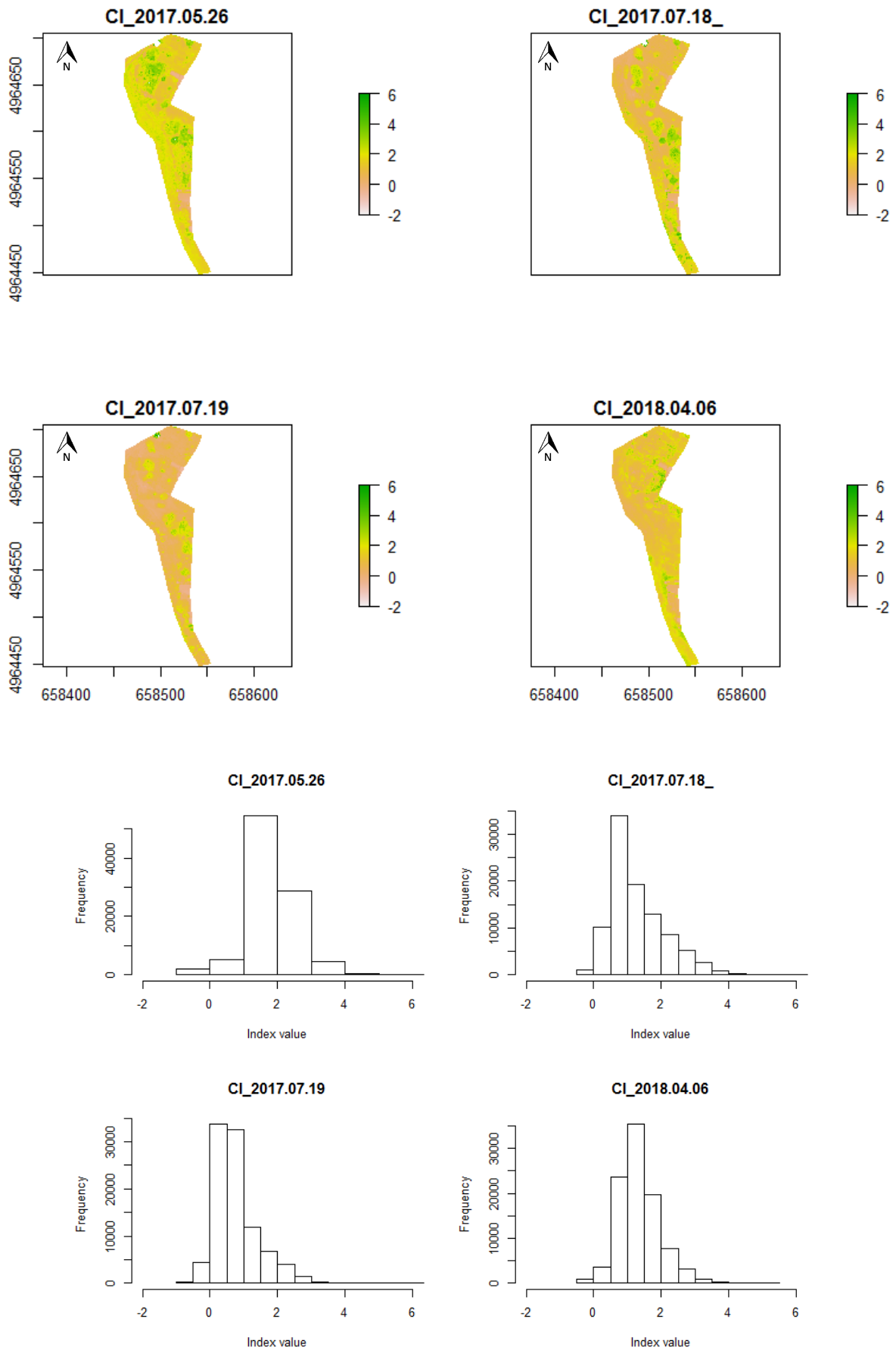


Figure 10.4. Maps and histograms of the four surveys expressed with CI, ancient riverbed.

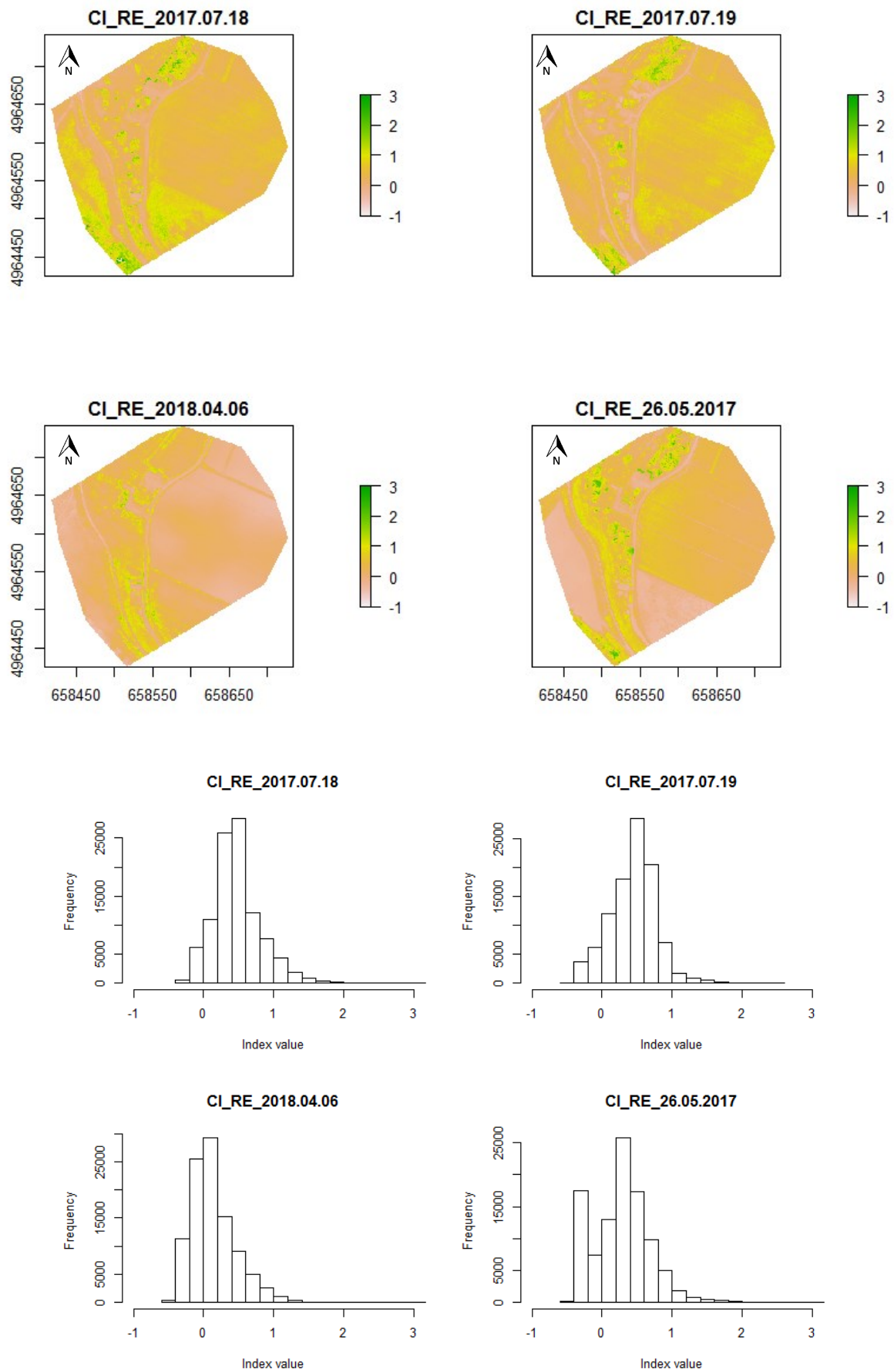


Figure 10.5. Maps and histograms of the four surveys expressed with CI-RE.

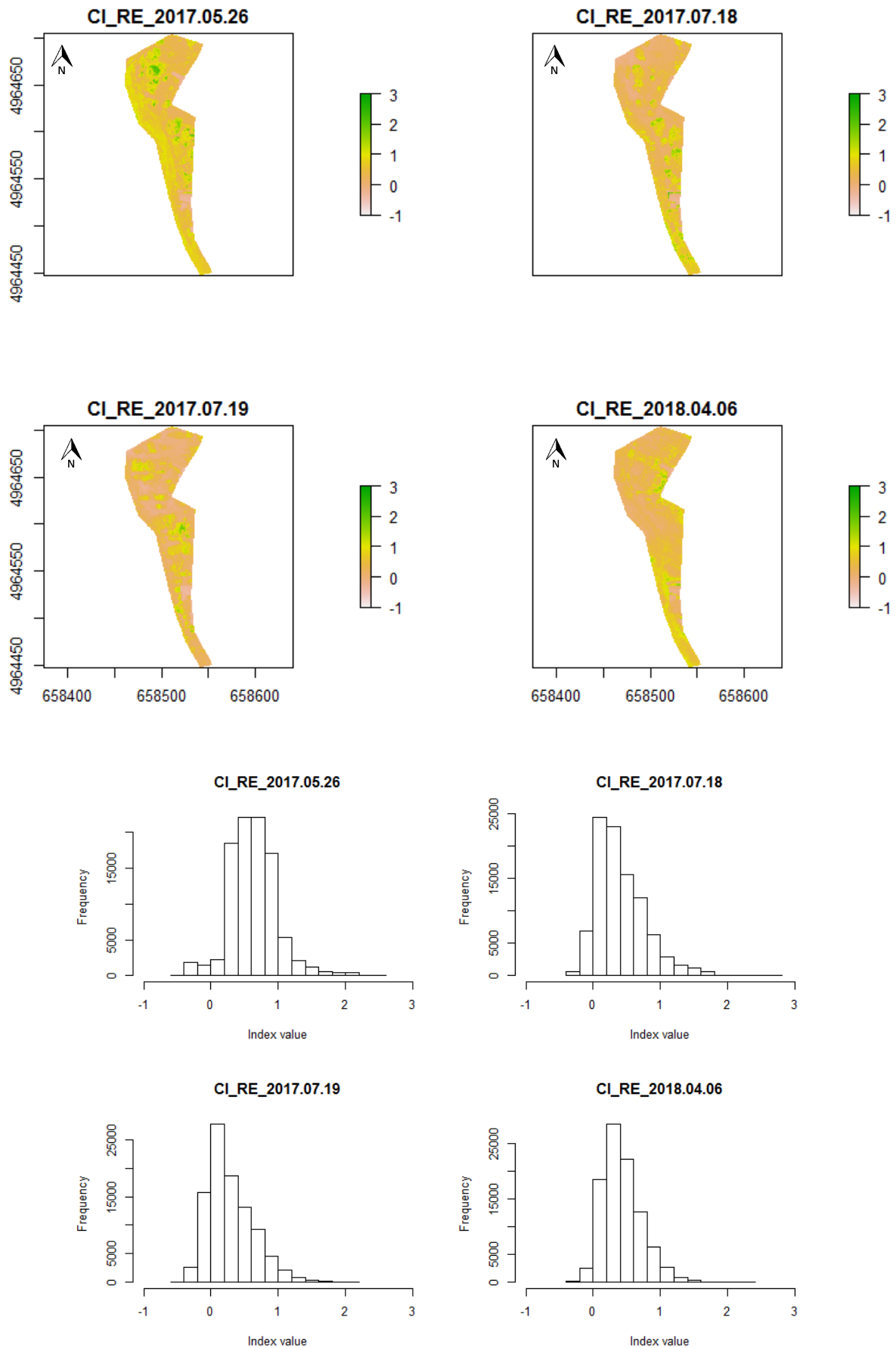


Figure 10.6. Maps and histograms of the four surveys expressed with CI-RE, ancient riverbed.

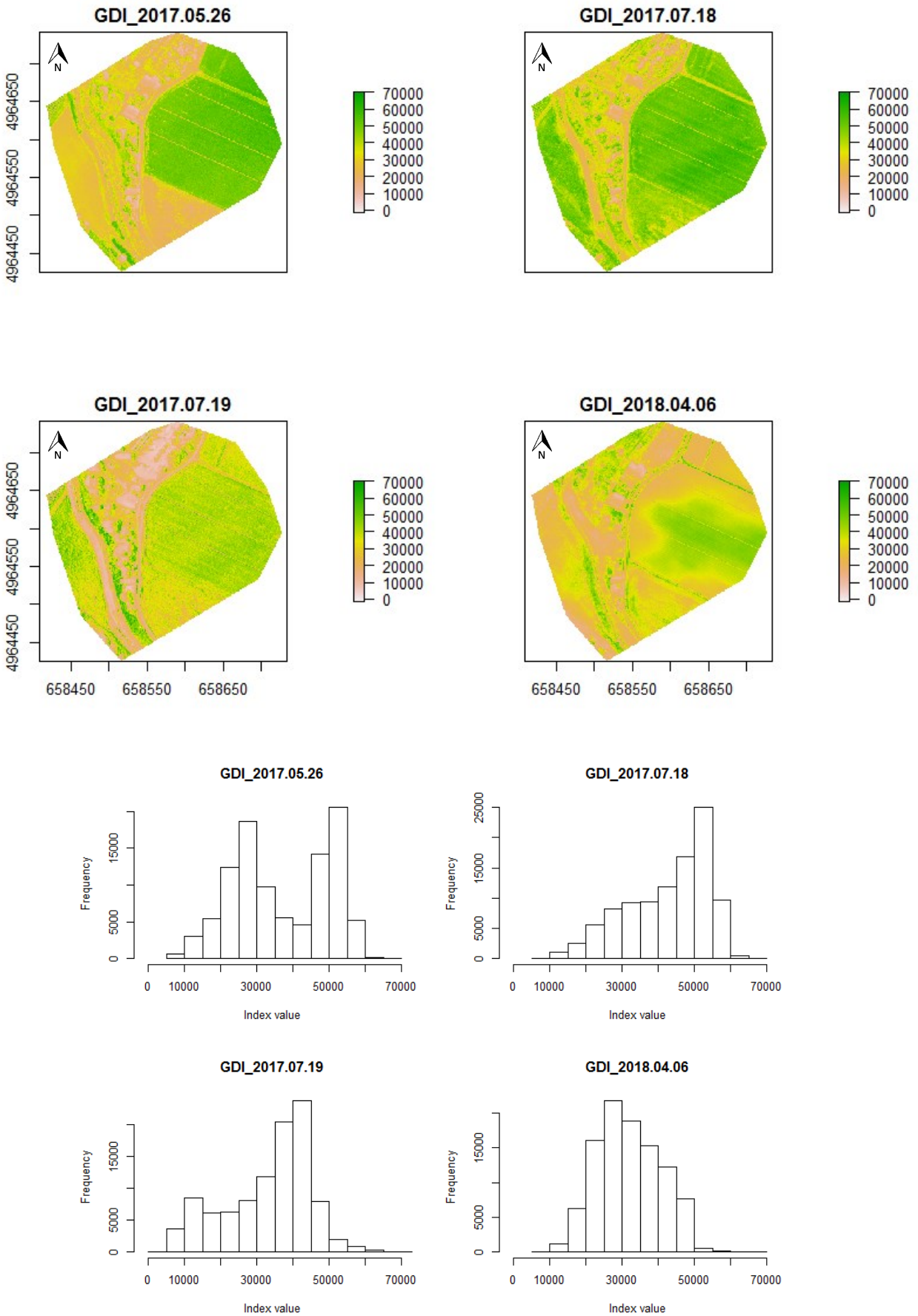


Figure 10.7. Maps and histograms of the four surveys expressed with GDI. V values in W/m^2 .

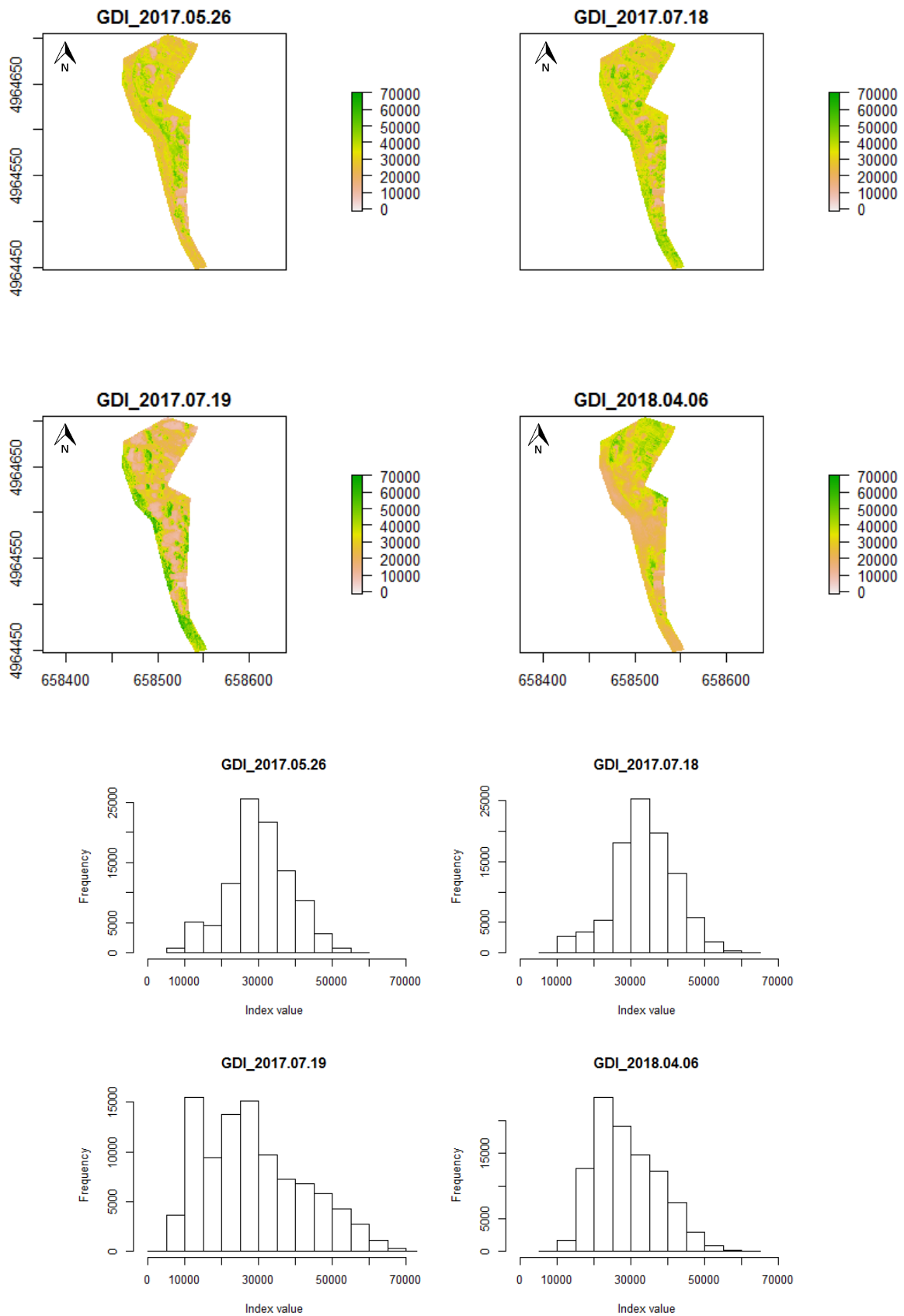


Figure 10.8. Maps and histograms of the four surveys expressed with GDI, ancient-riverbed. Values in W/m^2 .

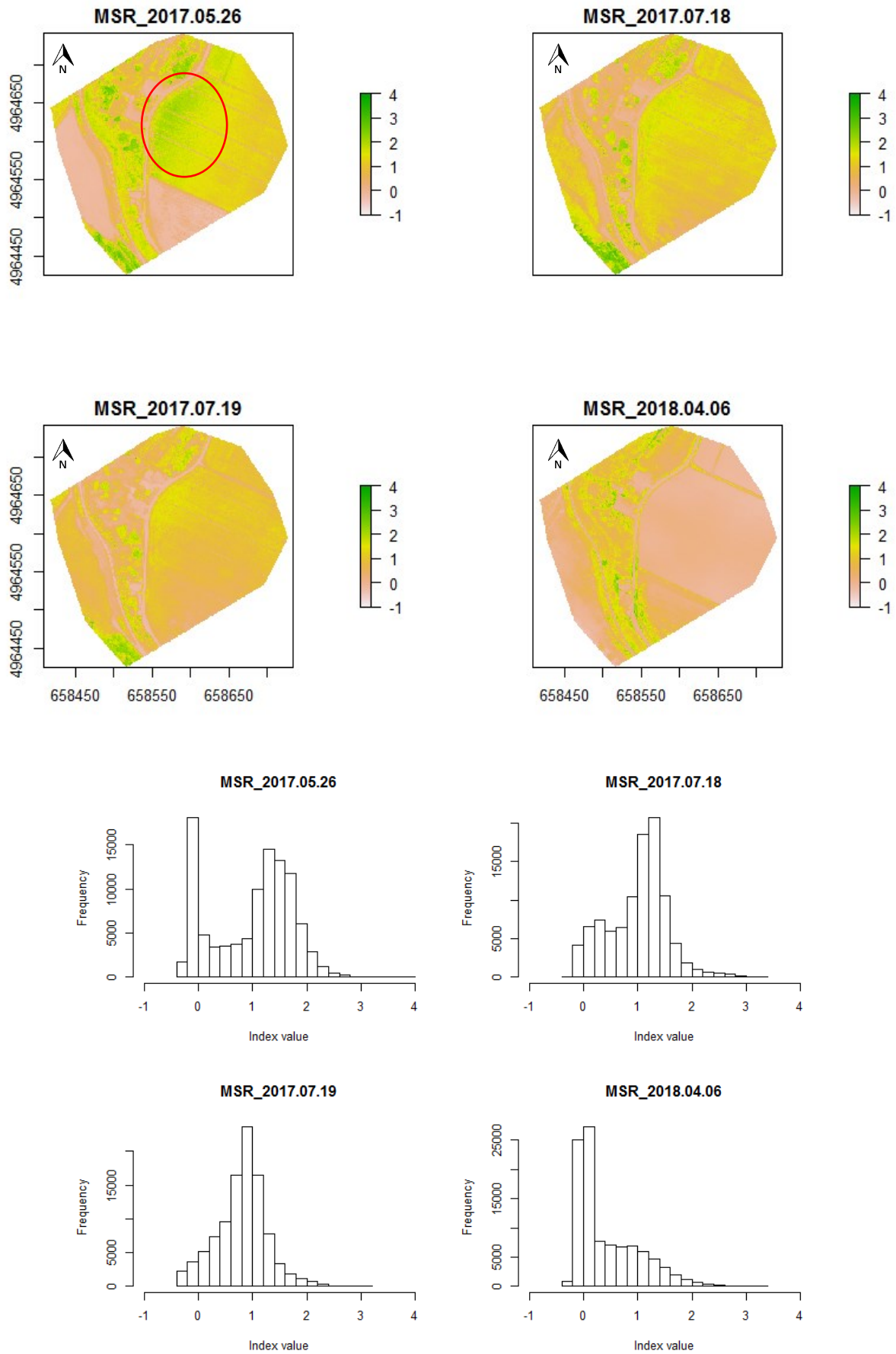


Figure 10.9. Maps and histograms of the four surveys expressed with MSR.

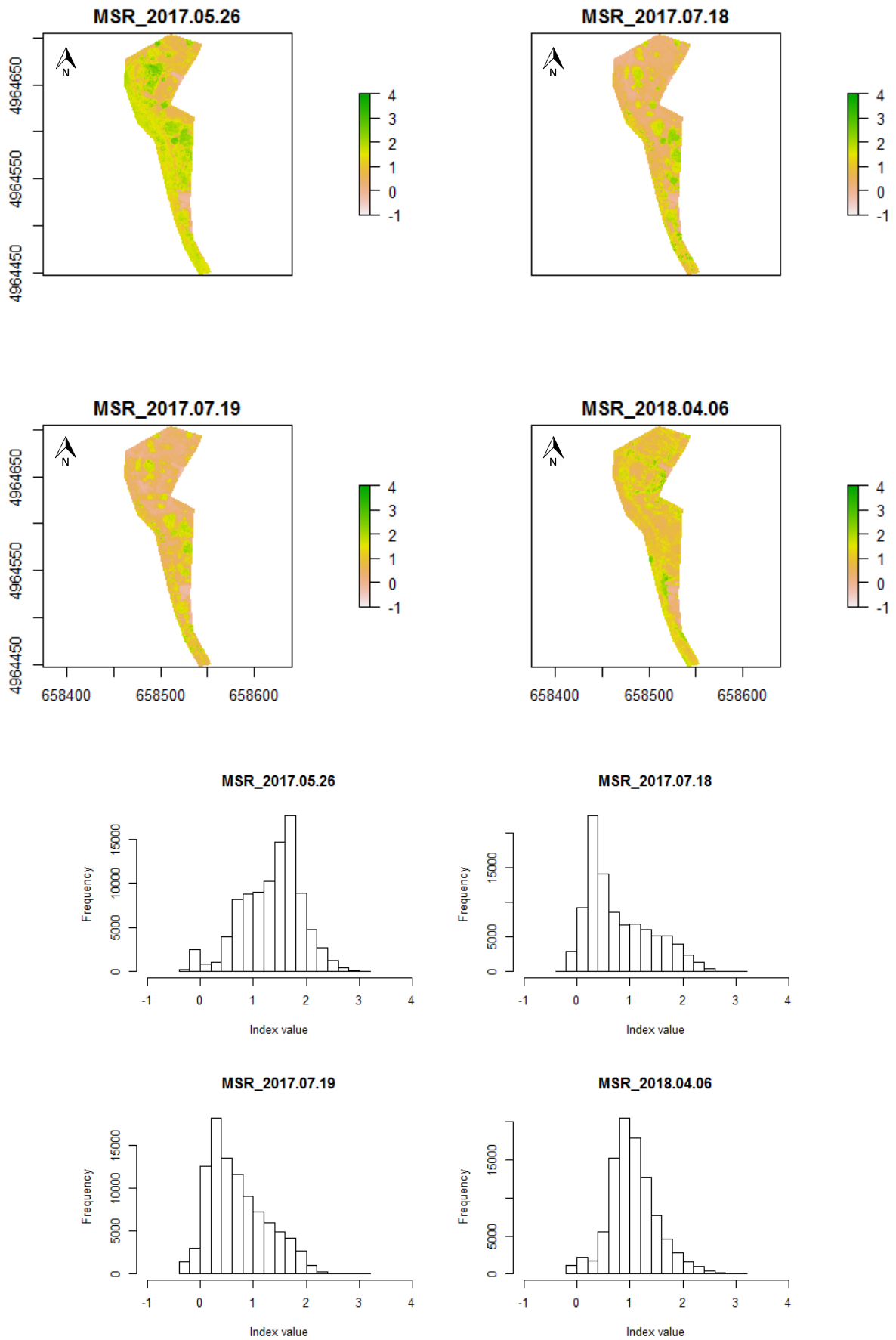


Figure 10.10. Maps and histograms of the four surveys expressed with MSR, ancient riverbed.

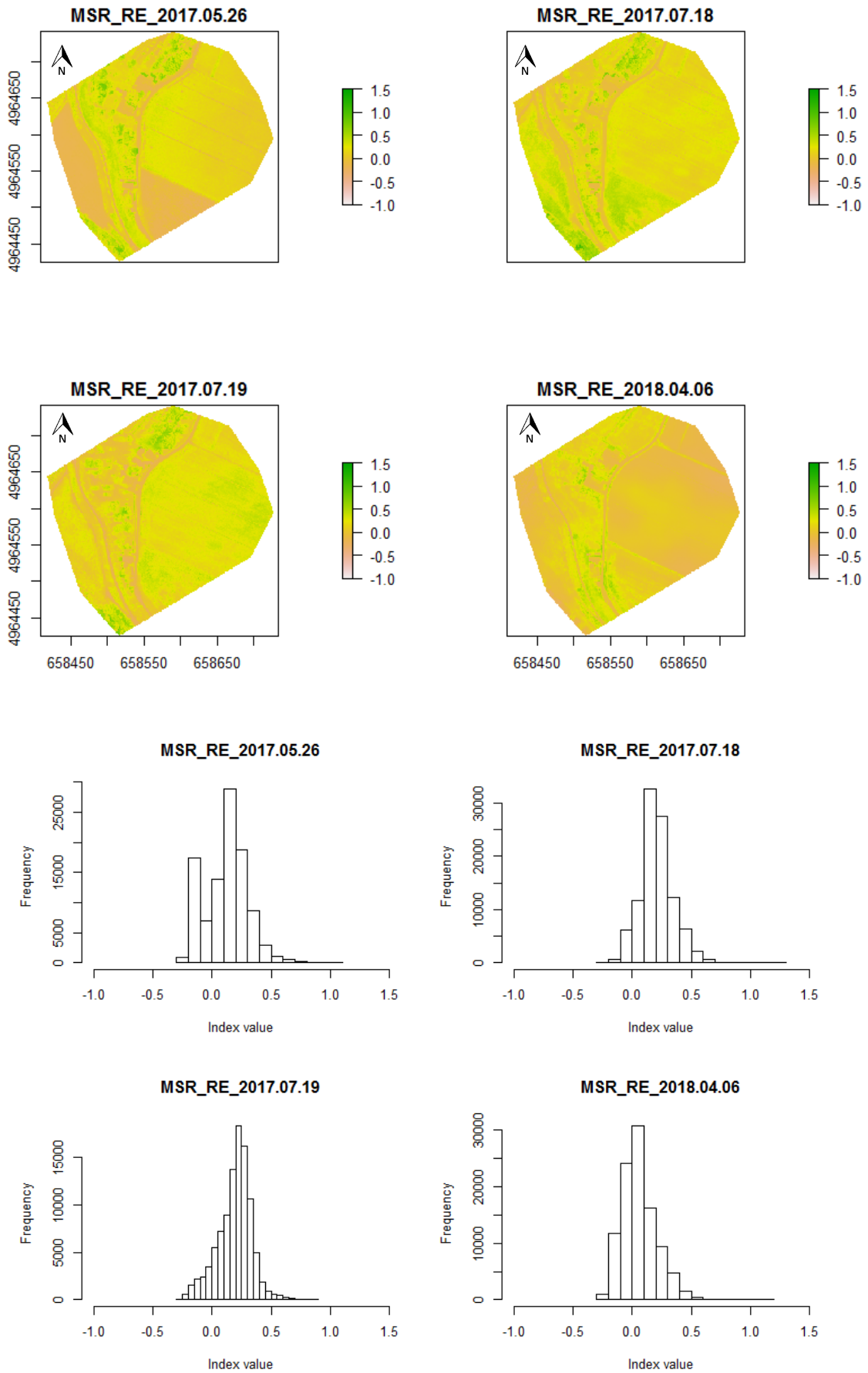


Figure 10.11. Maps and histograms of the four surveys expressed with MSR-RE.

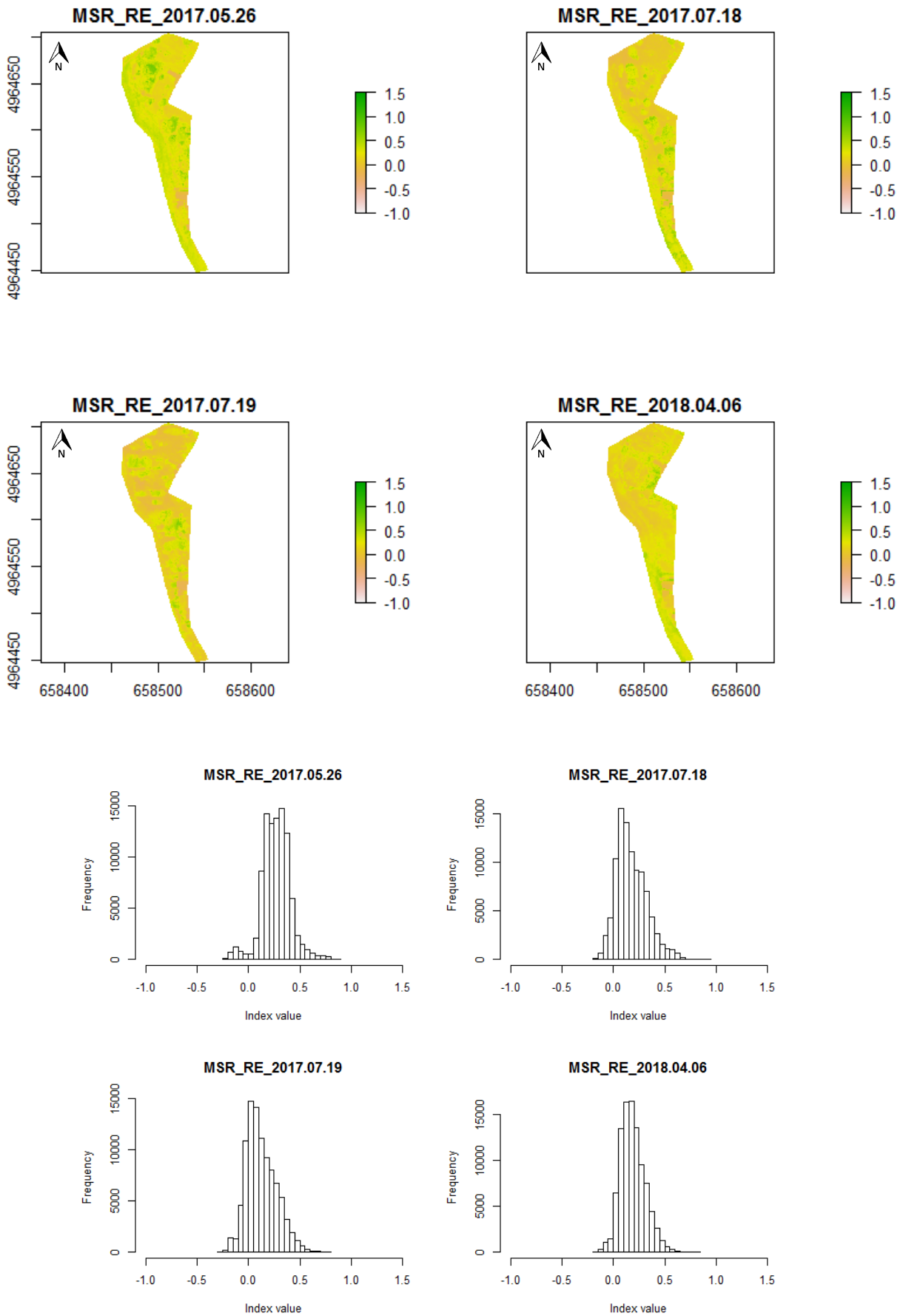


Figure 10.12. Maps and histograms of the four surveys expressed with MSR-RE, ancient riverbed.

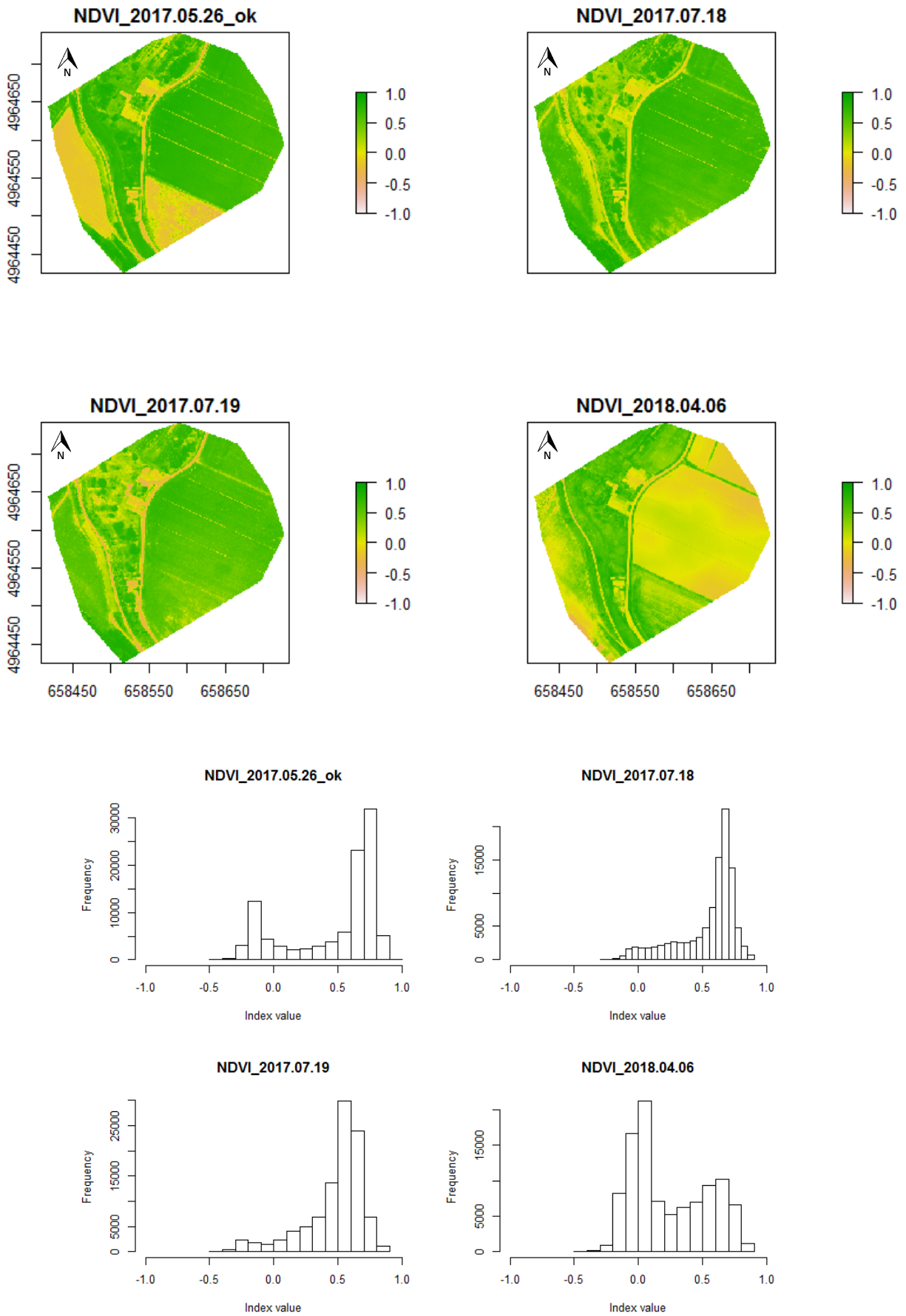


Figure 10.13. Maps and histograms of the four surveys expressed with NDVI.

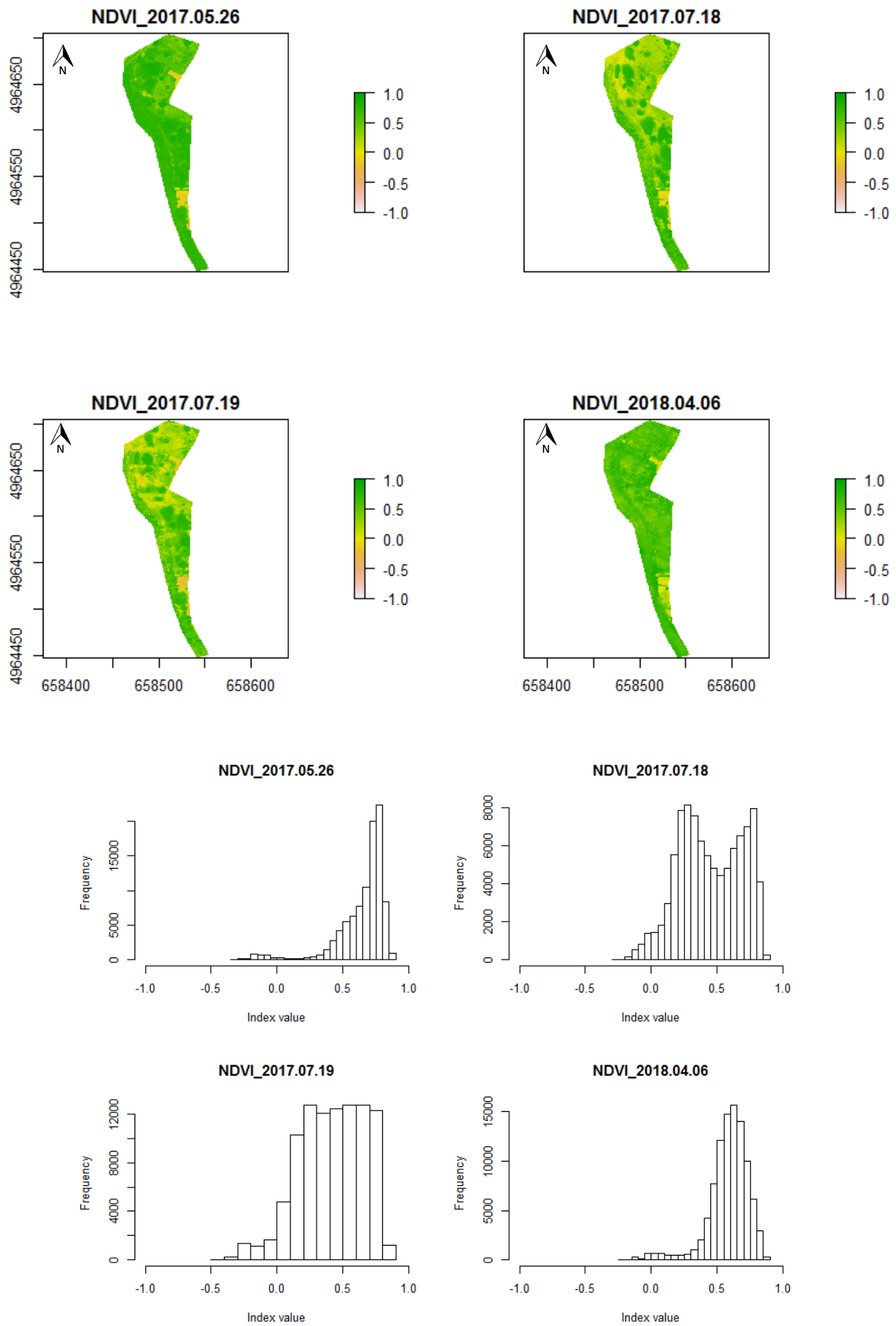


Figure 10.14. Maps and histograms of the four surveys expressed with NDVI, ancient riverbed.

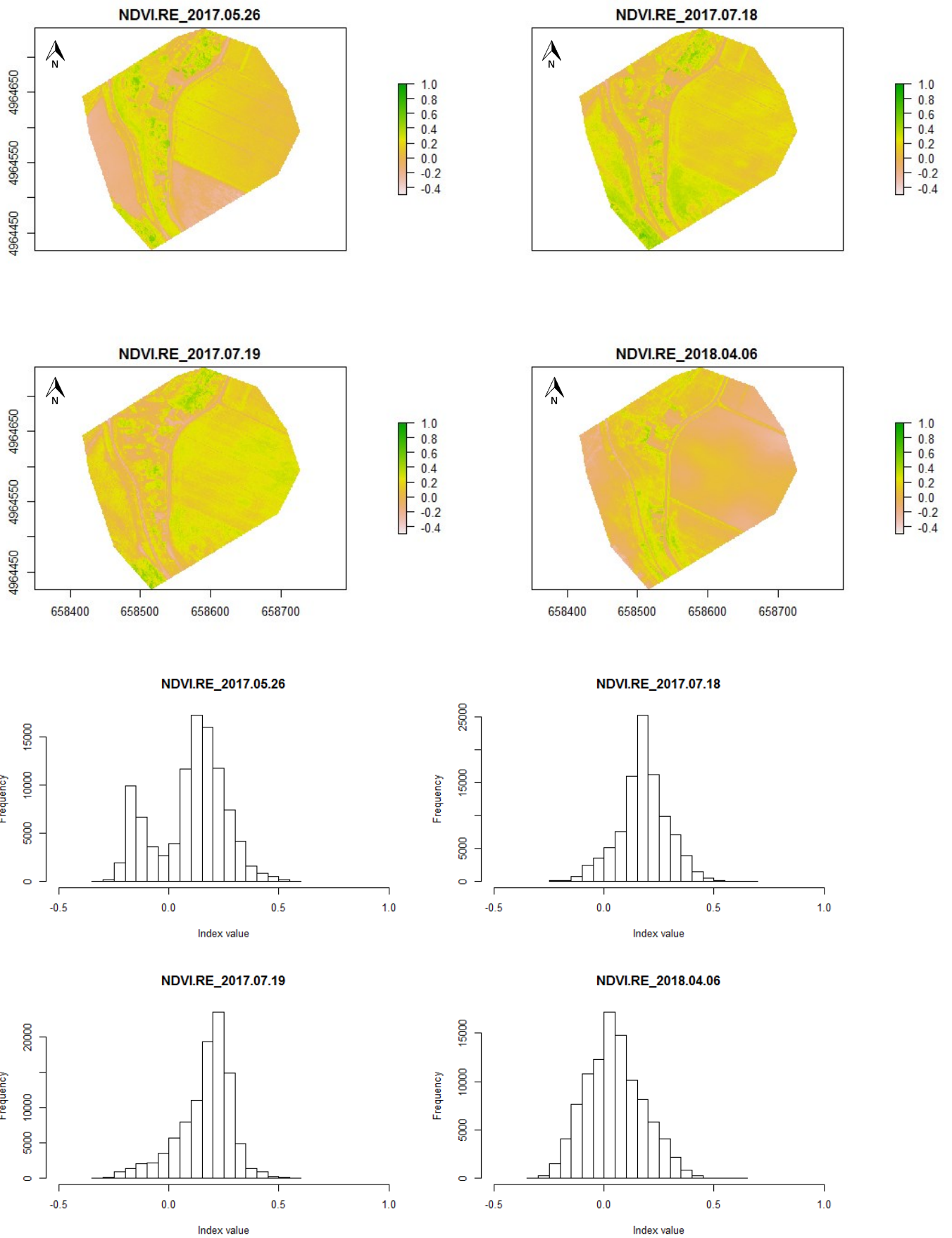


Figure 10.15. Maps and histograms of the four surveys expressed with NDVI-RE.

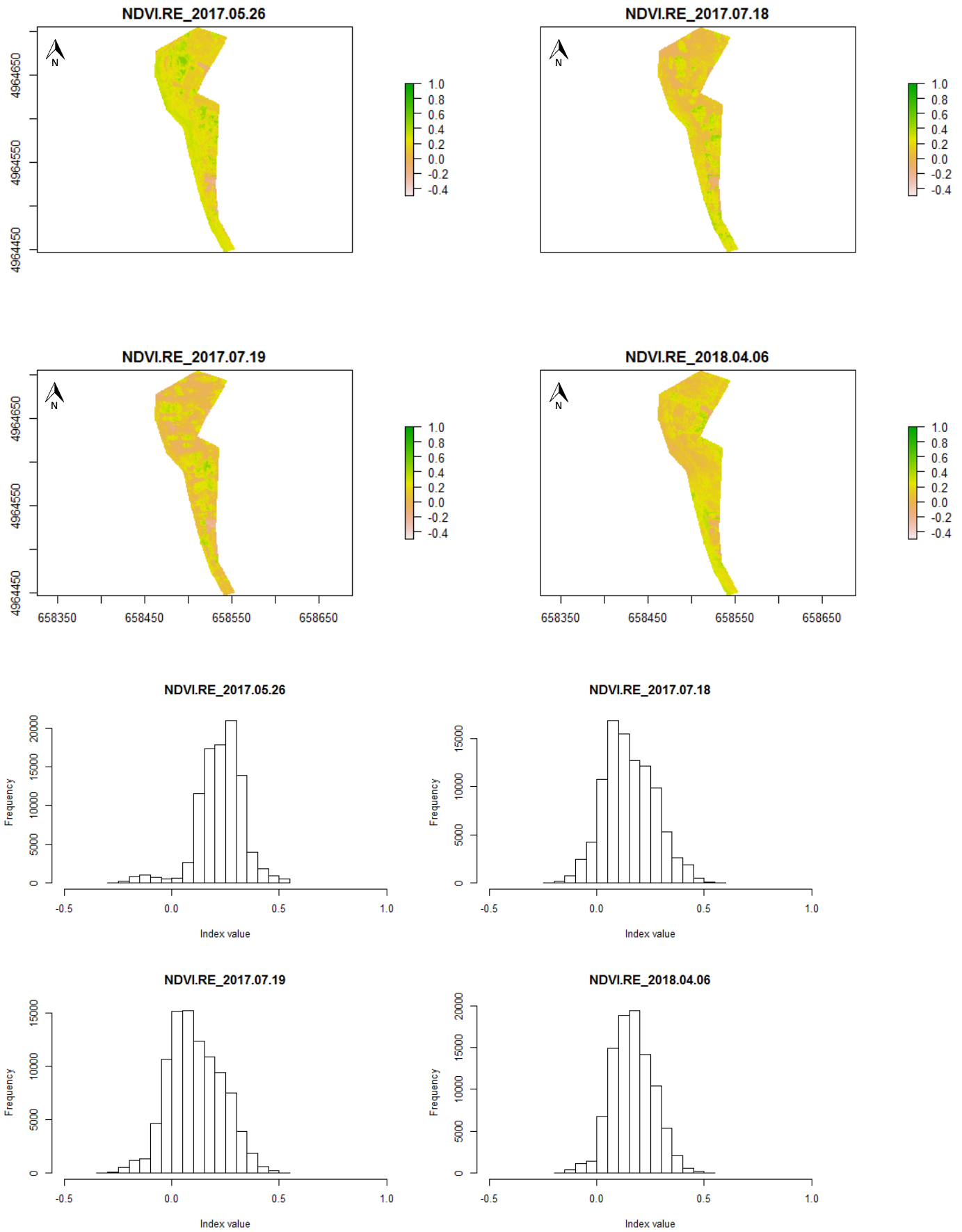


Figure 10.16. Maps and histograms of the four surveys expressed with NDVI-RE, ancient riverbed.

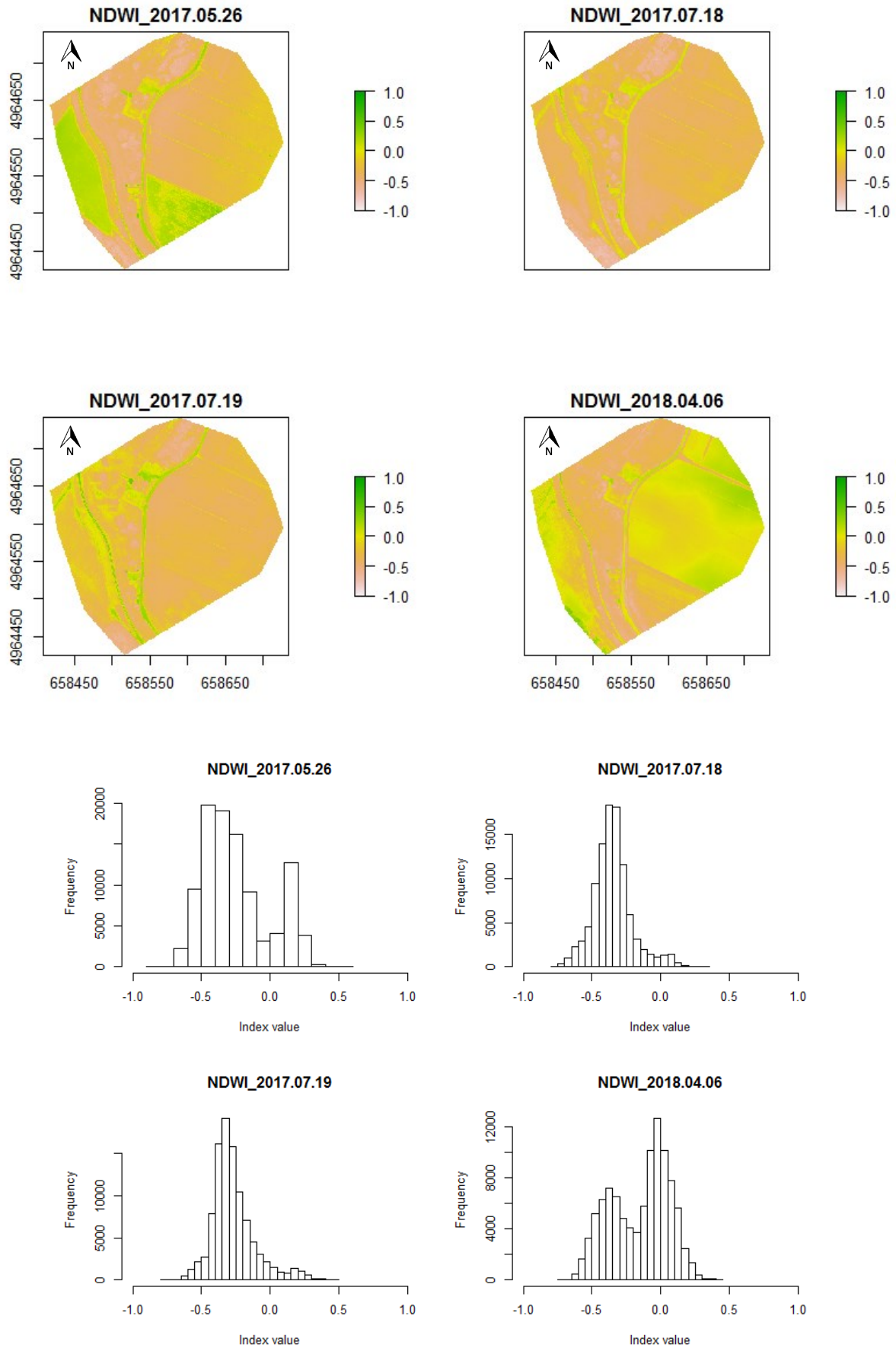


Figure 10.17. Maps and histograms of the four surveys expressed with NDWI.

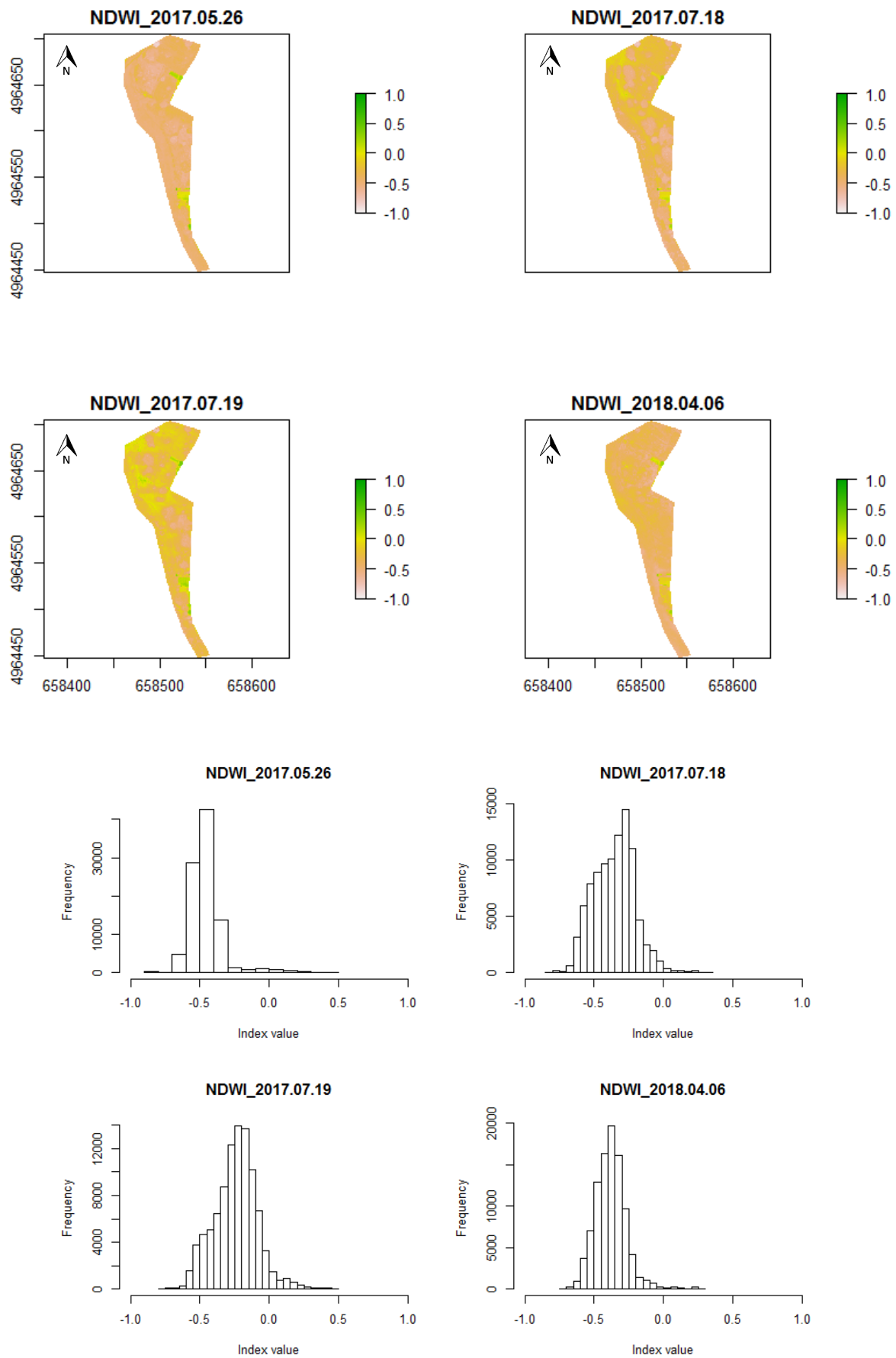


Figure 10.18. Maps and histograms of the four surveys expressed with NDWI, ancient riverbed.

The reason of using so many VIs is meant to compare them and try to understand which are the most suited for this type of analysis, since no established literature is available regarding the detection of water seepage paths with multispectral surveys.

The general trends of the maps are those of the season and the hour in which the survey has been performed. In fact, comparing the two surveys which have been done in July 2017, it can be noted how the values are generally higher for the survey taken at noon than those of the survey done in the morning (8 a.m.).

Regarding the seasons: May 2017 is late spring, in fact it has generally the highest values; in July 2017, although the month was arid (confirmed by the absence of green grass) the vegetative vigor of the crop on the east side of the maps was quite good. For this reason, the values of the indexes during summer are quite high in trend. For what it concerns April 2018, which is the month of reference, since a significant flood happened in March with two smaller flood peaks in the following weeks, the growth state of the vegetation (in particular the trees near the levee) is still poor and the sow of the crop wasn't done yet. It follows that the VIs are generally low, but with an increment when considering only the area of the ancient-riverbed mask.

In specific:

- **CI** (Figure 10.3, Figure 10.4): the index has a fairly similar behavior for the different maps. In the hourly comparison of July maps, it is noted that the 18th (h 12) the map has more areas with higher values, this is given by the greater reflectance when sunlight has higher incidence.

In the *ancient-riverbed*, the indices for July both decrease respect to the bigger mask, while for April 2018 they increase significantly. However, the highest values are obtained from the May 2017 vegetation, where the canopy of the trees has high indices. As normal for the dry season, in July the turf has a very low vigor.

- **CI-RE** (Figure 10.5, Figure 10.6): in the spring histograms (May 2017 and April 2018) it can be noted the presence of a high number of pixels with negative values. Physically this means that an abundant portion of vegetation has a greater red-edge reflectance than the NIR. By investigating with the "information element" tool of Qgis, it is noted that the values around -0.3 are common to the river, to the field inside the levee system and to the south-eastern field, external to the levee body and adjacent to the piezometers P1 and P2 (both lacking or with very poor vegetation), which could be evidence of wetlands. But these values are also common to built-up areas (roads, roofs). In all the maps are present low values for almost all the vegetation. (exception for a portion of the field outside the mask, in April 2018);

Within the *ancient riverbed* masks the negative values become almost nonexistent, values between 0 and 1 are maintained, corresponding to medium / low quantities of Chl.

- **GDI** (Figure 10.7, Figure 10.8): The values of the index show no difference to the trend of the other maps. However, in the map of April 2018, neglecting the green stain probably due to the presence of a cloud, it can be noted that in the north-western part of the map there a zone where the values of the index are much higher than the surroundings (the area is shown in the below Figure 10.19);



Figure 10.19. Detail of the GDI map of April 2018. Values in W/m^2 .

In the same [Figure 10.19](#), it can be noted that the highlighted greener zone is adjacent to a greener zone inside the levee system, which could be interpreted as path of the seepage of groundwater.

- **MSR** ([Figure 10.9](#), [Figure 10.10](#)): The high number of values close to 0 of the spring maps are representative of the fields not yet sown. In the comparison between summer maps, that of 8 o'clock (19th) has the peak of values centered around the value 1, while that of the 12 has the peak shifted to values between 1 and 1.5. In the map of May 2017 ([Figure 10.9](#)) the red-circled area has higher values, with respect to the surrounding area. This could be due to a higher soil moisture, but also to the proximity to the irrigation channel.

- **MSR-RE** ([Figure 10.11](#), [Figure 10.12](#)): This VI has not shown interesting trends that have not already been highlighted.

- **NDVI** ([Figure 10.13](#), [Figure 10.14](#)): the peak of the more numerous values is after 0.5 for all maps, because of the vegetative vigor of the crop, made exception for April 2018. What is more interesting, however, is the high number of negative values of this last map. In fact, according to the literature, negative values of NDVI indicate water surfaces. This could be indicative of high humidity areas.

As for the *ancient-riverbed* maps, April 2018 results the map with the highest indexes and even its average has tripled compared to that of the general mask ([Table 11](#)).

- **NDVI-RE** ([Figure 10.15](#), [Figure 10.16](#)): These maps reflected the trends of the other indices which used the red-edge band. Anyhow, an anomalous area, highlighted in red in [Figure 10.20](#), has

been found from a precision analysis of the map of April 2018, where a greener area has been located near to the levee, next to areas with values near to 0.

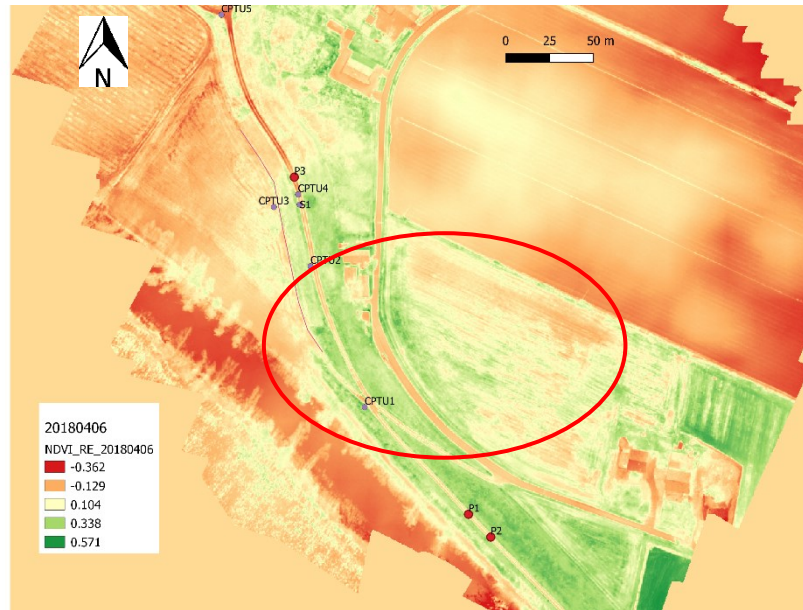


Figure 10.20. Excerpt from the NDVI-RE map of April 2018.

○ **NDWI** (Figure 10.17, Figure 10.18): in the summer the values above 0 are almost absent, since the month had absence of precipitations and also the Secchia River was characterized by minimum flow. While in spring the values above 0 are more numerous. No significant elements for the ancient-riverbed maps have been found.

Table 11. Mean values of the spectral maps.

	2017- 05-06		2017-07-18		2017-07-19		2018-04-06	
	Mean	A.R.* Mean	Mean	A.R. Mean	Mean	A.R. Mean	Mean	A.R. Mean
CI	0.933	1.832	1.230	1.287	0.857	0.768	0.540	1.332
CI-RE	0.286	0.631	0.481	0.406	0.445	0.290	0.138	0.427
GDI	37137	30269	42752	33659	33196	28674	31936	28760
MSR	0.987	1.350	1.000	0.792	0.803	0.701	0.420	1.057
MSR-RE	0.120	0.270	0.209	0.177	0.193	0.126	0.057	0.189
NDVI	0.473	0.648	0.541	0.446	0.477	0.415	0.241	0.584
NDVI-RE	0.098	0.226	0.178	0.151	0.166	0.108	0.046	0.165
NDWI	-0.247	-0.454	-0.349	-0.355	-0.269	-0.242	-0.151	-0.380

*A.R. stands for ancient-riverbed mask

In the comparison of the two summer surveys, the survey done in the 18th of July 2017 has shown better overall results and can be compared more efficiently with the other surveys in terms of reflectance (i.e. hour/sun incidence). Moreover, the presence of shadows in the map of the 19th, caused by the early hour, can affect the interpretation of the indexes. So, in the following sections, only the survey of 18/07/2017 will be considered.

10.1. *Analysis of the spring season conditions: May 2017 compared with April 2018*

The vegetation of April 2018 gets low index averages because the field on the right is bare, since sowing usually takes place in May. In spite of this, the ditch zones on the sides of the road have quite high levels of vigor.

As for the area affected by the passage of the paleo-river, there is a triplication of the averages compared to the mask including the fields. However, even in this case, the averages are lowered by the quantity of trees without a leaf mantle, due to the recently started spring season.

It might be interesting to note that in the NDVI map the negative values are much higher than those of the other surveys. According to the literature, negative NDVI values indicate the presence of water. Given the scarce precipitations (6.8 mm registered at Ponte Bacchello in 05/04/2018), this could be related to the presence of water ponding in the soil following the flood of March. In fact, the bare field at north-west (in [Figure 10.21](#)) has NDVI values that reach up to -0.4. Alongside this field there are the piezometers INP1 and P4. INP1 has registered, during the secondary flood of 5/4/2018, a small peak compared to its decreasing trend, reaching 27 m a.s.l ([Figure 6.3](#) in Section 6).

Also, P1 and P2 recorded high pore water pressure values in the flood of March 2018, reaching respectively 27 and 27.5 m a.s.l. as highest value. As a possible consequence of that, it can be noted that in the NDVI map, very high values are reached, close to 0.9, in the vicinity of the houses closest to the two piezometers, in the south-eastern part of the map. This might mean that groundwater has enhanced the growth of the vegetation in this area, without creating ponding. The other indices also assign very high values to these areas (NDVI-RE). However, these values cannot be compared with the other surveys, since the survey of 2018 covered a larger area. One can only assume that the ancient riverbed develops laterally up to that area. But there is no evidence to support this hypothesis, since no penetrometric tests have been performed in this part of the embankment.

In [Figure 10.22](#) the maps of the surveys of May 2017 (in blues) and April 2018 (in greens) with NDVI values higher than 0.65 are presented jointly, to have a better visualization of the areas that are characterized by a NDVI value typical of vigorous vegetation. It's possible to notice that the non-blank areas are mostly in the zone that have been masked with the "ancient riverbed" mask.

For what it concerns the eastern field, the NDVI values of the map of May 2017 get higher in proximity of the ancient riverbed mask. This might mean that the soil moisture deriving from the presence of the ancient riverbed has effects also on this part of the field. This aspect should be considered in future studies.

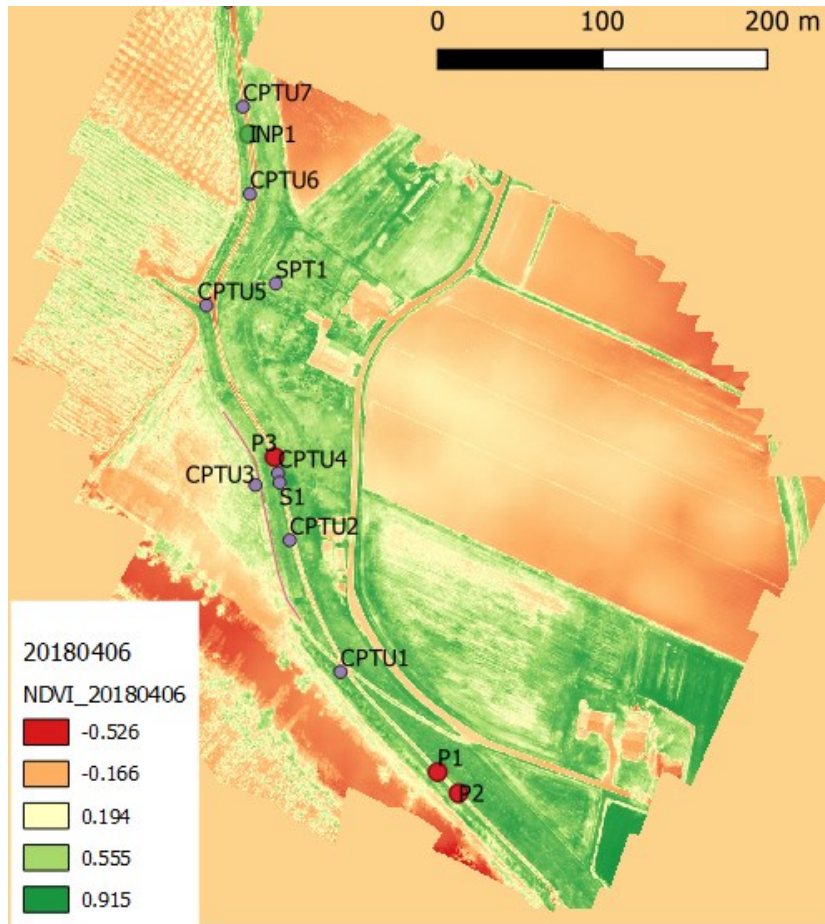


Figure 10.21. Complete NDVI map of the multispectral survey of April 2018.

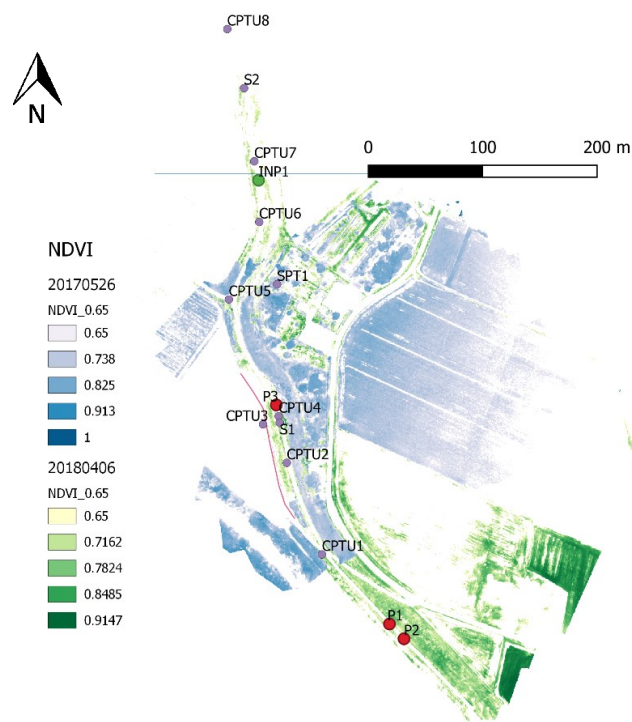


Figure 10.22. Superposition of NDVI values above 0.65 of the maps of May 2017 (blues) and April 2018 (greens).

11. NDVI from satellite Sentinel-2

In this chapter will be presented the results of the calculation of mean monthly NDVI over the MSIs from the European satellites Sentinel-2. In fact, since there were no clear evidences of correlation between VIs and pore pressure values, it seemed appropriate to extend the analysis to a larger area, on the eastern part of the Secchia River.

It's necessary to state that the resolution of the satellite images is far less precise than the orthophotos resulting from the survey with the RPV.

11.1. Overview of the Sentinel-2 satellite

The Sentinel-2 is part of a mission developed by the ESA (European Space Agency), part of the program Copernicus, which has been developed to monitor the green areas of the planet and aimed at preventing and managing natural disasters.

It is composed by two satellites, the Sentinel-2A, launched the 23rd of June 2015, and the Sentinel-2B, launched the 7th of March 2017.

Sentinel-2 has 12 spectral bands available, as shown in [Figure 11.1](#). Since this study is focusing on a small area, it has been decided to use only those bands with an acceptable spatial resolution. For this reason and for the quality of being worldwide used, only the index NDVI will be calculated, which needs in input the NIR and the red bands, respectively the 8th and the 4th band of the Sentinel-2, with a spatial resolution of 10 m.

Band Number	S2A		S2B		Spatial resolution (m)
	Central wavelength (nm)	Bandwidth (nm)	Central wavelength (nm)	Bandwidth (nm)	
1	442.7	21	442.2	21	60
2	492.4	66	492.1	66	10
3	559.8	36	559.0	36	10
4	664.6	31	664.9	31	10
5	704.1	15	703.8	16	20
6	740.5	15	739.1	15	20
7	782.8	20	779.7	20	20
8	832.8	106	832.9	106	10
8a	864.7	21	864.0	22	20
9	945.1	20	943.2	21	60
10	1373.5	31	1376.9	30	60
11	1613.7	91	1610.4	94	20
12	2202.4	175	2185.7	185	20

Figure 11.1. Characteristics of the spectral bands acquired by Sentinel-2.

11.2. NDVI maps of the extended area

The products available from the Sentinel-2 satellites are mainly two, the maps of type 1C and the type 2A/2Ap. Where the second type, which are the ones taken into consideration for the analysis, are images with corrected reflectance and irradiance, done through automatic algorithms, while the first type is not corrected. Unfortunately, this type of correction has been introduced only in the 2017, meaning that only a small number of the images, covering only two years, will be used to create a mean NDVI value for each month.

The major issue of the satellite images is the presence of clouds. In fact, each image with clouds over the area of interest was discarded. Moreover, before the satellite Sentinel-2B was launched, the number of available images was inferior, since there was only the satellite Sentinel-2A.

The list of the images taken into analysis is, sorted by month of acquisition, the following:

- *January*: 09, 19/01/2018; 04, 14/01/2019.
- *February*: 28/02/2018; 8, 13, 18/02/2019.
- *March*: none.
- *April*: 14, 19, 24/04/2018;
- *May*: 14, 24/05/2017, 19/05/2018.
- *June*: 03, 13, 23/06/2017; 03, 13, 23/06/2018.
- *July*: 03, 13, 23/07/2018; 08, 18, 23/07/2018.
- *August*: 02, 12/08/2017; 07, 17, 22, 27/08/2018.
- *September*: 01, 21/09/2017; 06, 11, 16, 21/09/2018.
- *October*: 11, 31/10/2017.
- *November*: none.
- *December*: 20/12/2017; 05, 15/12/2018.

In [Table 12](#) are presented the mean values obtained from the selected satellite images.

Table 12. Mean NDVI values of each month, calculated from the year 2017 to 2019.

Month	NDVI mean value
January	0.428
February	0.415
March	/
April	0.539
May	0.609
June	0.635
July	0.633
August	0.579
September	0.539
October	0.542
November	/
December	0.359

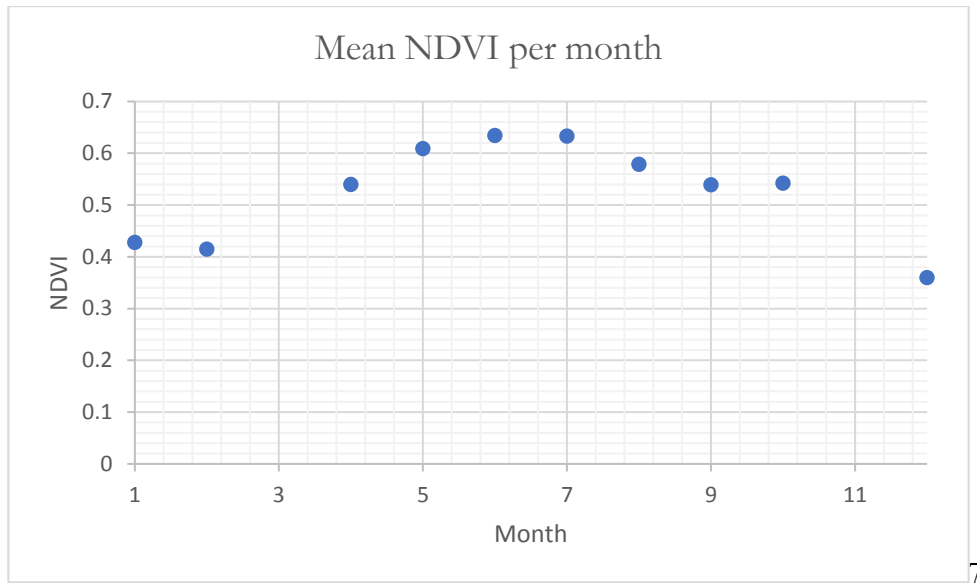
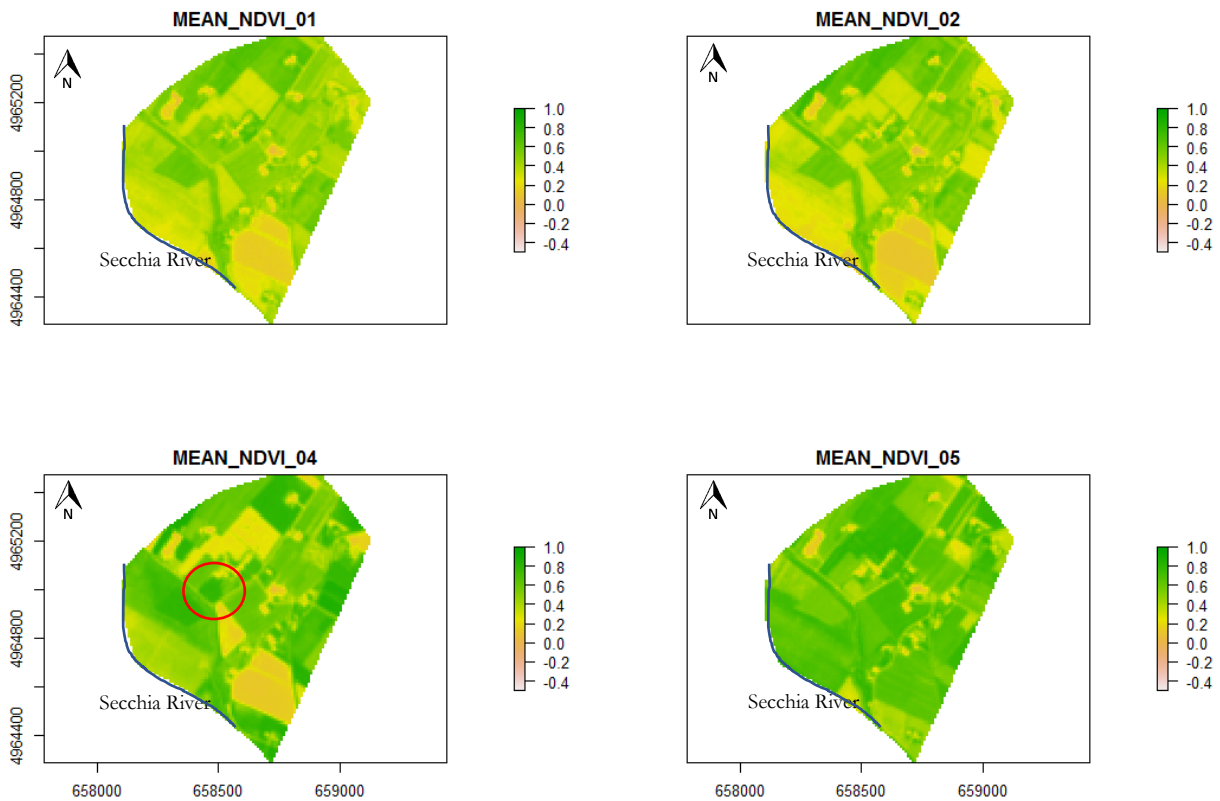
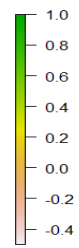
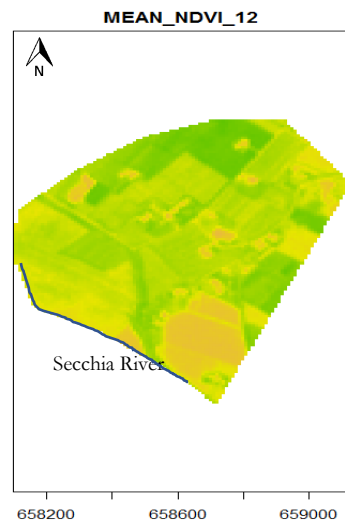
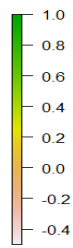
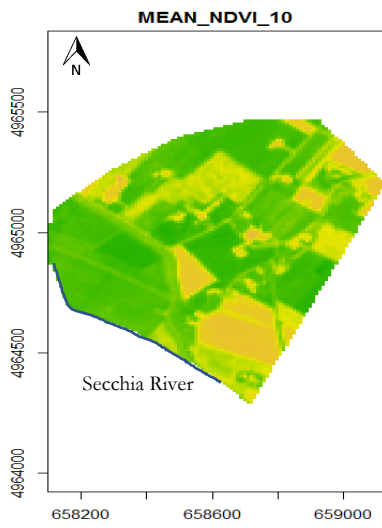
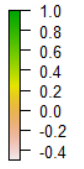
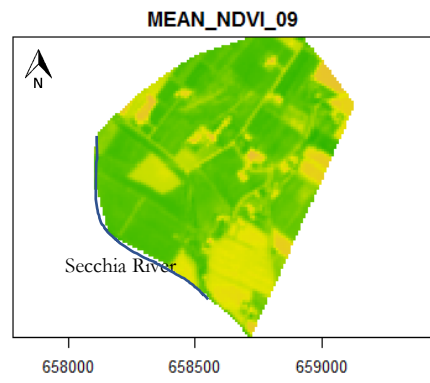
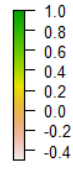
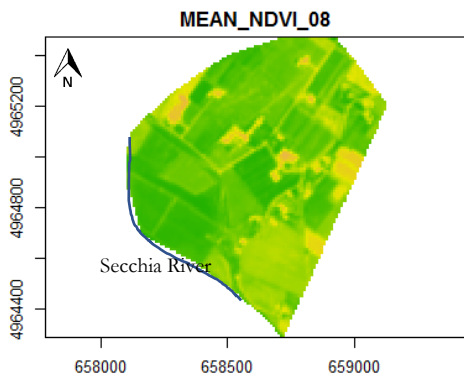
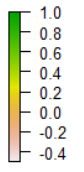
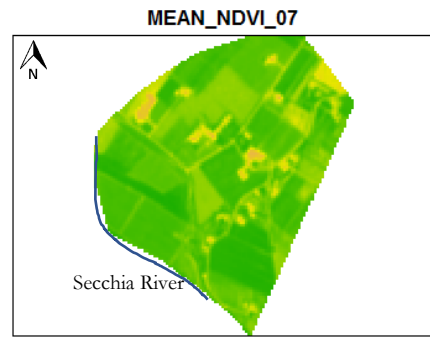
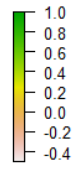
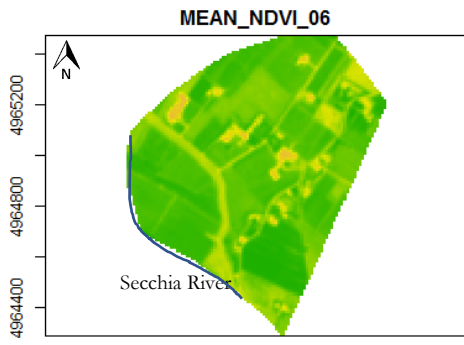


Figure 11.2. Mean NDVI trend from satellite images.

In Figure 11.2 it's clear the parabolic trend of the NDVI values over the monthly distribution. Anyway, the result cannot be interpreted univocally, since many images are missing, for example the whole March, and the values of April are only from the 2018.

In Figure 11.3 are presented the NDVI mean maps for each month, together with their relative histograms.





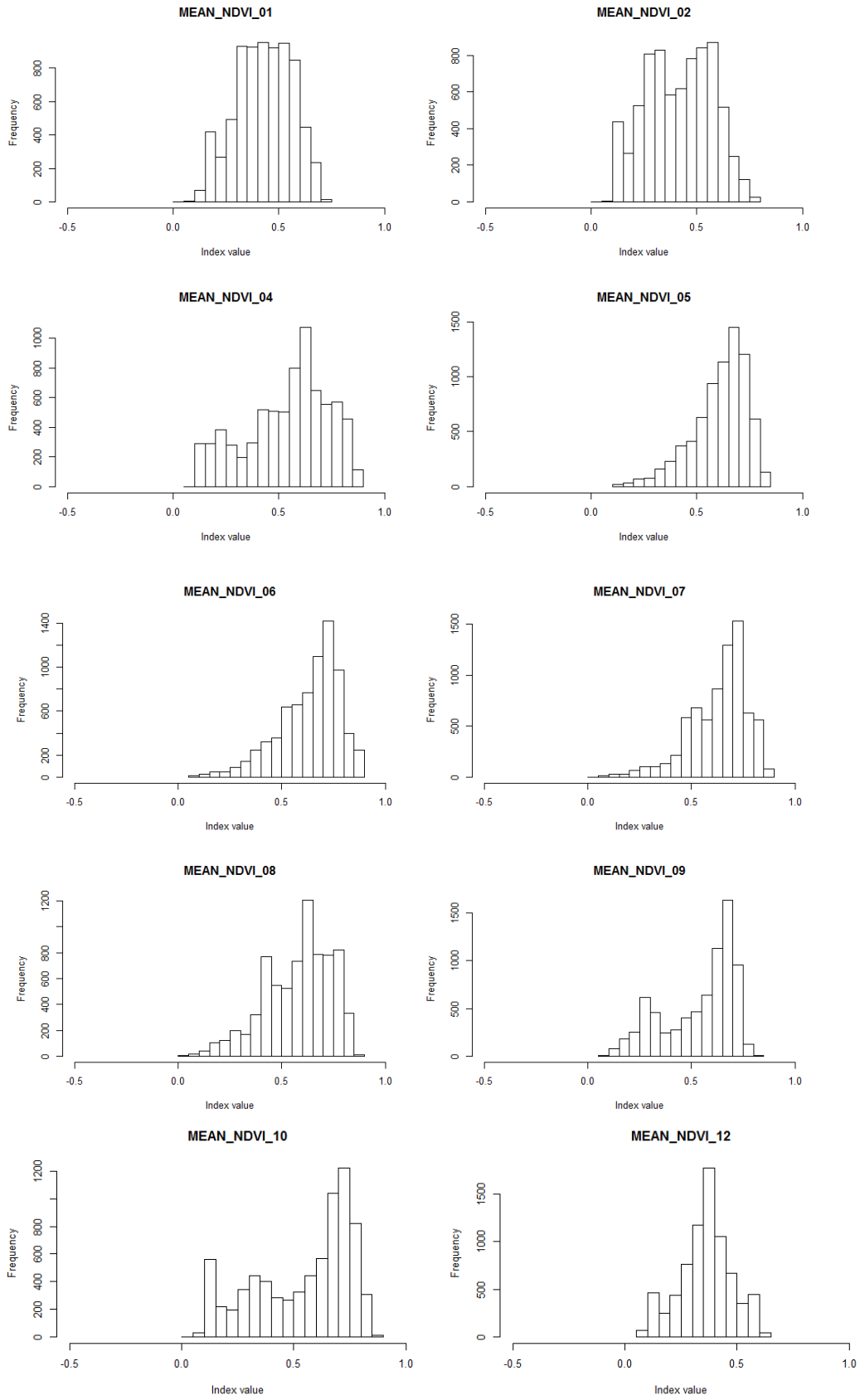


Figure 11.3. NDVI maps and histograms of the Sentinel-2 satellite images.

11.3. Results and analysis of the satellite maps

The use of historical data from the satellite imagery has the aim of obtaining a seasonal trend of the selected index, in this case NDVI, to have a better confront with the values obtained from the precision survey with the RPV.

In the analysis of the single satellite images, the presence of "greener" fields (based on the color palette used in this study) with exact contours cannot, in the opinion of the writer, be taken as an indication of the presence of seepages, in fact it is probably due to the irrigation of the fields. On the contrary, it will be necessary to look for areas with shaded contours and with increasing green indices towards a maximum point.

However, a long series of images can give an example of the areas that on average have higher vegetative indexes, and go to cross this information with the spectral reliefs with greater resolution.

An example is the area highlighted by the red circle in maps of April, in [Figure 11.3](#), which can be seen to have a higher NDVI value than the surrounding areas.

12. Discussion

After obtaining the month-to-month NDVI averages from the satellite images, it was possible to compare the NDVI averages obtained from the multispectral survey with RPV, weighted on the monthly averages (from [Table 12](#)), with the piezometric values. Considering that a change in pore water pressure in a certain day cannot be compared with the chlorophyll content in the vegetation on the same day, for the piezometric level was calculated the average piezometric level of two weeks. The multispectral survey of the 19th of July 2017 was not considered in this analysis, since the survey of the previous day (18/07/2017) has shown better results.

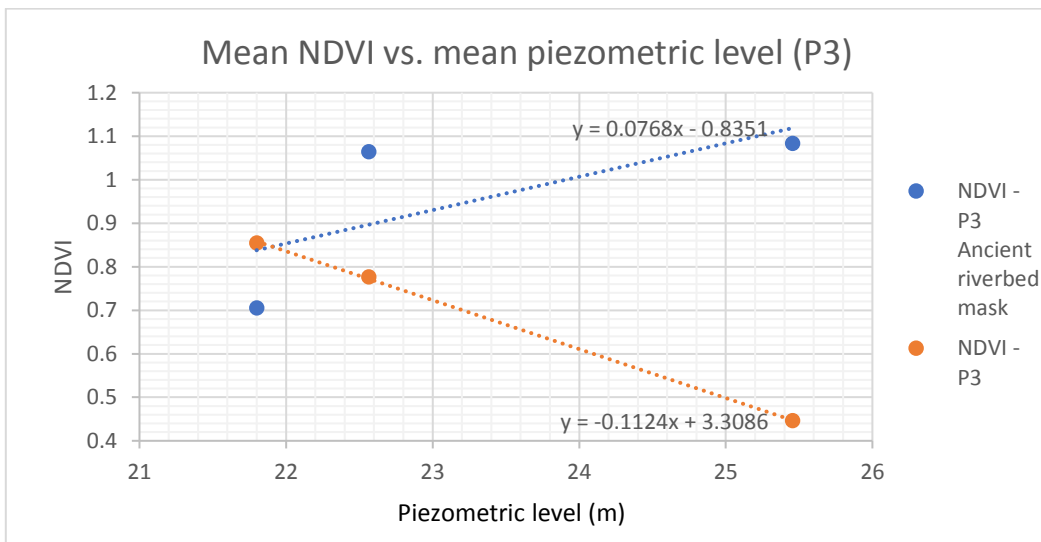
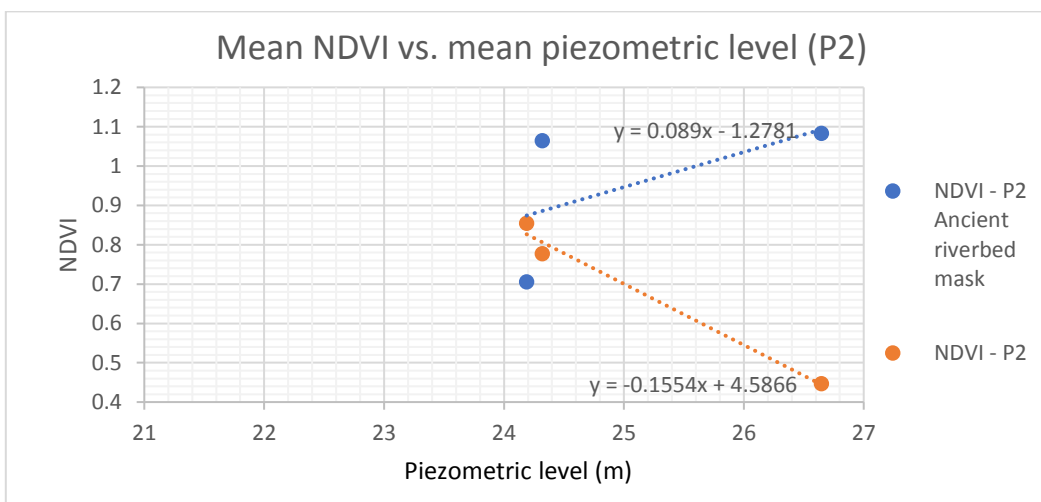
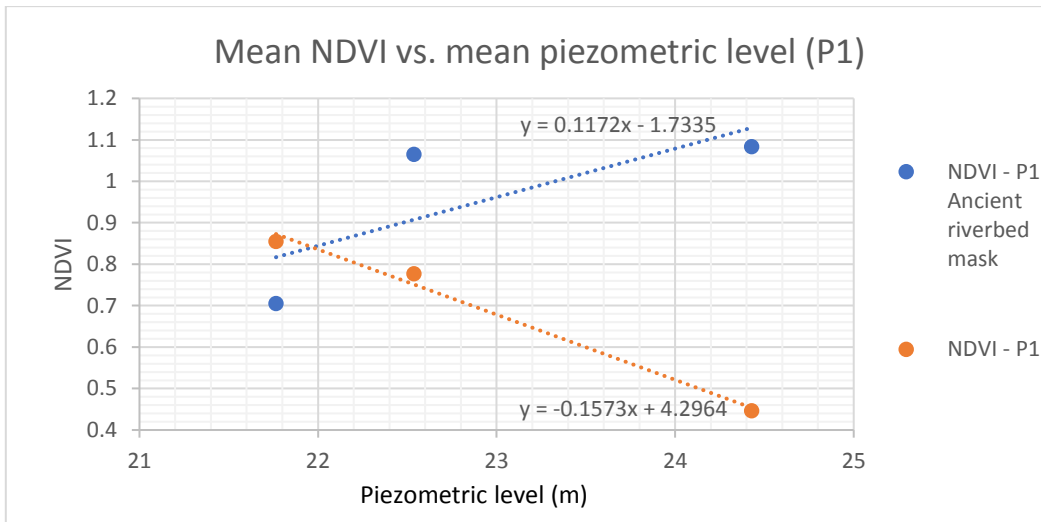
Table 13. Mean piezometric and hydrometric levels over two weeks.

	12 - 26/05/2017	3 - 18/07/2017	24/03/2018 - 06/04/2018
P1 [m]	22.537	21.660	24.428
P2 [m]	24.320	24.243	26.645
P3 [m]	22.564	21.799	25.454
INP1 [m]	23.573	22.991	25.853
Hydr. Level [m]	21.264	~21.3	26.276

Table 14. Weighted NDVI average.

Survey date	Mean NDVI	Mean NDVI (ancient riverbed)
26/05/2017	0.776	1.064
18/07/2017	0.855	0.705
06/04/2018	0.446	1.083

The NDVI values and the piezometric levels from [Table 13](#) and [Table 14](#) have been graphed, to obtain a linear correlation between the data. [Figure 12.1](#) shows the correlation for each piezometer. The dashed blue lines represent the linear correlation for the ancient riverbed maps, while the dashed orange lines represent the linear correlation for the whole maps.



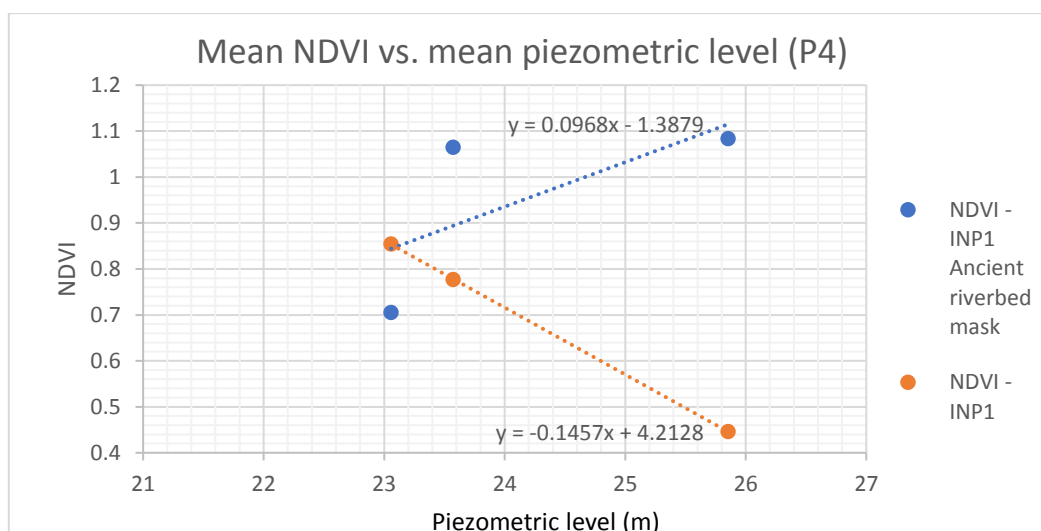


Figure 12.1. Linear correlation graphs between NDVI values and piezometric levels.

In the different graphs of [Figure 12.1](#) it's clear how the trend is positive when considering the ancient riverbed mask, while the trend becomes negative when considering the whole map. It means that the NDVI value increases when the mean piezometric level increases.

The negative trend when considering the whole map is, by the writer's side, caused both by the seasonality of the vegetation and by the farming schedule. In fact, even if in March 2018 the hydrometric level of the Secchia River increased significantly, together with the pore pressures measured by the piezometers, the vegetation available to absorb the increase of humidity of the soil was scarce or inexistent (e.g. fields not yet sown).

The positive trends shown in the different graphs of [Figure 12.1](#) seem to confirm the hypothesis of the position of the ancient riverbed and also the correlation between NDVI values and piezometric levels.

13. Conclusions

This study tried to obtain a possible procedure for the detection of water seepage in embankments through the collection of data that were already available.

In the first place, the multispectral orthophotos and the DEMs have been created using the software Photoscan. The orthophotos have been used in QGIS to interpret the reflectance behavior of vegetation, using different VI, with the aim of detecting areas with strong vegetative vigor, which could be related to a higher moisture content in the soil, that could be the consequence of water seepage. The high-precision DEMs have been useful to interpret the morphology of the area, in particular in the analysis of possible areas that could be affected by water ponding (due to convergent slopes) and in the creation of cross sections of the embankment, fundamental in the analysis of the aquifer behavior. In particular, the aquifer behavior has been interpreted using the DEM altitude values, the stratigraphy from previous geological studies of the embankment and the pore water pressure values recorded by the piezometers installed along the embankment.

Moreover, two masks have been created, applicable to all the surveys: one that covers the surveyed area where the ancient riverbed should be, and one comprehensive of the biggest area in common to the different surveys. This has been done to have a comparison of the mean values resulting from the different VI maps.

Afterwards, the maps deriving from the application of the VIs, NDVI in the specific, have been validated: This procedure has been carried out firstly by calculating a mean NDVI value for each month over the area of interest through satellite MSIs. Then, the NDVI deriving from the maps obtained from the high-precision surveys have been weighted with the aforementioned mean NDVI value of the corresponding month.

Finally, a linear correlation between the weighted NDVI value of each survey and the piezometric levels, averaged over two weeks before the date of the surveys, has been performed.

The whole analysis and the results obtained showed encouraging outcomes, especially in the interpretation of the groundwater flow and in the correlation between the ancient riverbed spectral maps and the piezometric values.

Despite this, the present research aims to introduce a complex problem that requires more detailed studies.

The suggestions for a possible extension of the research are the following:

- Find the existence of an empirical correlation between the increase of the pore pressure in the piezometers following flood events with the increase of humidity in the ground near the levee body, using both multispectral sensors and hygrometric sensors, these should be located at different depth. Specifically, verify if the pixels with negative values, as in the NDVI map of April 2018, correspond to areas with higher humidity or not;
- Obtain a more complete historical series (using images obtained by available satellites, considering that those with higher resolution are to be paid), better if divided by seasons, to obtain more effective comparisons with future surveys;

- For the specific case of the ancient riverbed: search for areas outside the levee body with coarse granulometry that may represent preferential seepage paths which will then be analyzed with more attention in the MSIs;
- Scientific literature has proved the value of hyperspectral techniques (Gao et al., 1996, Ceccato et al., 2002). Through the analysis of the middle-infrared and the thermic infrared bands, it is possible to better highlight the zone with higher humidity, while this is not possible with multispectral techniques;
- The use of multiple indexes, as in the present study, can give a more complete view of the problem.

Bibliography

- Agisoft, L. L. C. (2018). Agisoft PhotoScan user manual: professional edition, Version 1.4.
- Autorità di Bacino del Fiume Po (2004). Linee generali di assetto idrogeologico e quadro degli interventi. Bacino del Secchia. Parma, Technical Report.
- Autostrada Regionale Cispadana S.p.A, (2012). Realizzazione dell'Autostrada Regionale Cispadana dal casello di Reggiolo-Rolo sulla A22 al casello di Ferrara Sud sulla A13 – Asse autostradale (comprensivo degli interventi locali di collegamento viario al sistema autostradale). Relazione geologica, geomorfologica, idrogeologica.
- Baranoski, G. V. G., & Rokne, J. G. (2005). A practical approach for estimating the red edge position of plant leaf reflectance. *International Journal of Remote Sensing*, 26(3), 503-521.
- Cae (2016). Progetto sperimentale per il monitoraggio di un argine sul fiume Secchia in località Ponte Motta, Comune di Cavezzo (MO). AiPo, Progetto Esecutivo.
- Cannarozzo, R., Cucchiarini, L., Meschieri, W. (2012). Misure, rilievo, progetto. Zanichelli.
- Castaldini, D., Raimondi, S. (1985). Geomorfologia dell'area di Pianura Padana compresa fra Cento, Finale Emilia e S. Agostino. *Atti della Società dei Naturalisti e Matematici di Modena*, 116: 147-176.
- Castaldini, D. (1989). Evoluzione della rete idrografica centropadana in epoca protostorica e storica. In: *Convegno Nazionale di Studi "Insediamenti e viabilità nell'alto ferrarese dall'Età Romana al Medioevo"*. Italy. pp. 115-134.
- Ceccato, P., Gobron, N., Flasse, S., Pinty, B., & Tarantola, S. (2002). Designing a spectral index to estimate vegetation water content from remote sensing data: Part 1: Theoretical approach. *Remote sensing of environment*, 82(2-3), 188-197.
- Chen, J. M. (1996). Evaluation of vegetation indices and a modified simple ratio for boreal applications. *Canadian Journal of Remote Sensing*, 22(3), 229-242.
- D'Alpaos, L., Brath, A., Fioravante, V., Gottardi, G., Mignosa, P., & Orlandini, S. (2014). Relazione tecnico-scientifica sulle cause del collasso dell'argine del fiume Secchia avvenuto il giorno 19 gennaio 2014 presso la frazione San Matteo. Report of the Emilia-Romagna Region.
- De Martino, V. (2016). Definizione di procedure per la realizzazione di sistemi di monitoraggio finalizzati alla riduzione del rischio idrogeologico legato a collassi arginali. AiPo.

EASAC (2018). Trends in extreme weather events in Europe. Preparing for climate change adaptation: an update on EASAC's 2013 study.

Engeo srl Studio Geologico ed Idrogeologico (2014). Fiume Secchia: Lavori urgenti per il miglioramento delle condizioni di stabilità del corpo arginale nei confronti di fenomeni di filtrazione – Geological and seismic report. AiPo.

Hosgood, B., Jacquemoud, S., Andreoli, G., Verdebout, J., Pedrini, G., & Schmuck, G. (1995). Leaf optical properties experiment 93 (LOPEX93). Ispra Italy European Commission, Joint Research Centre Institute of Remote Sensing Applications.

Huete, A. R. (1988). A soil-adjusted vegetation index (SAVI). *Remote Sensing of Environment*, 25. pp. 53-70.

Huete, A. R., Didan, K., Miura, T., Rodriguez, E. P., Gao, X., & Ferreira, L. G. (2002). Overview of the radiometric and biophysical performance of the MODIS vegetation indices. *Remote sensing of environment*, 83.1-2: 195-213.

Gao, B. C. (1996). NDWI — A normalized difference water index for remote sensing of vegetation liquid water from space. *Remote sensing of environment*, 58(3), 257-266.

Gao, Z., Wang, Q., Cao, X., & Gao, W. (2014). The responses of vegetation water content (EWT) and assessment of drought monitoring along a coastal region using remote sensing. *GIScience & remote sensing*, 51.1: 1-16.

Gitelson, A. A., Gritz, Y., & Merzlyak, M. N. (2003). Relationships between leaf chlorophyll content and spectral reflectance and algorithms for non-destructive chlorophyll assessment in higher plant leaves. *Journal of plant physiology*, 160(3), 271-282.

Gitelson, A., & Merzlyak, M. N. (1994). Spectral reflectance changes associated with autumn senescence of *Aesculus hippocastanum* L. and *Acer platanoides* L. leaves. Spectral features and relation to chlorophyll estimation. *Journal of Plant Physiology*, 143(3), 286-292.

Gong, P., Pu, R., Li, Z., Scarborough, J., Clinton, N., & Levien, L. M. (2006). An integrated approach to wildland fire mapping of California, USA using NOAA/AVHRR data. *Photogrammetric Engineering & Remote Sensing*, 72.2: 139-150.

Horler, D. N. H., Dockray, M., & Barber, J. (1983). The red edge of plant leaf reflectance. *International Journal of Remote Sensing*, 4(2), 273-288.

Jensen, J. R. (2009). Remote sensing of the environment: An earth resource perspective. Second Edition, Pearson Education India. pp. 357-415.

Jordan, C. F. (1969). Derivation of Leaf-Area Index from Quality of Light on the Forest Floor. *Ecology*, Vol. 50, No. 4. Pp. 663-666.

Khalifa, A. Z., Alwan, I. A. K., & Jameel, A. (2013). Establishment of 3D Model With Digital Non-Metric Camera in Close Range Photogrammetry. *Engineering and Technology Journal*, 31(8 Part (A) Engineering), 1601-1611.

Lillesand, T.; Kiefer, R. W.; Chipman, J. (2012). Remote sensing and image interpretation. John Wiley & Sons.

Linder, W. (2016). Digital photogrammetry – A practical course. Springer, Fourth Edition.

Martelli, L. (2011). Quadro sismotettonico dell'Appennino emiliano-romagnolo e della Pianura Padana centrale. Servizio Geologico, Sismico e dei Suoli, Regione Emilia-Romagna.

McFeeters, S. K. (2013). Using the normalized difference water index (NDWI) within a geographic information system to detect swimming pools for mosquito abatement: A practical approach. *Remote Sensing*, 5.7: 3544-3561.

Papale, D., Belli, C., Gioli, B., Miglietta, F., Ronchi, C., Vaccari, F. P., & Valentini, R. (2008). ASPIS, a flexible multispectral system for airborne remote sensing environmental applications. *Sensors*, 8.5: 3240-3256.

Reichmuth, A.; Oczipka, M.; Pinnel, N. (2013). Detection of forest parameters using imaging spectroscopy. University of Applied Sciences Dresden.

Rouse Jr, J. W., Haas, R. H., Schell, J. A., & Deering, D. W. (1974). Monitoring vegetation systems in the Great Plains with ERTS. *Proceedings, 3rd Earth Resource Technology Satellite (ERTS) Symposium*, vol. 1, p. 48-62.

Saltini, G., Tosatti, G. (1989). Hydrological balance of the drainage basins of the rivers Secchia and Panaro. *International Congress on Geoengineering Vol I*, Torino.

Schiereck, G. J. (1998). Fundamentals on water defences. TAW-ENW report.

Siegfried, J., Longchamps, L., & Khosla, R. (2019). Multispectral satellite imagery to quantify in-field soil moisture variability. *Journal of Soil and Water Conservation*, 74(1), 33-40.

Sims, D. A., & Gamon, J. A. (2002). Relationships between leaf pigment content and spectral reflectance across a wide range of species, leaf structures and developmental stages. *Remote sensing of environment*, 81(2-3), 337-354.

Tagle, X. (2017). Workflow Agisoft Photoscan for Micasense Rededge Images. Technical report.

Vescovo, L., Gianelle, D. (2006). Mapping the green herbage ratio of grasslands using both aerial and satellite-derived spectral reflectance. *Agriculture, ecosystems & environment*, 115(1-4), 141-149.

Wu, C., Niu, Z., Tang, Q., & Huang, W. (2008). Estimating chlorophyll content from hyperspectral vegetation indices: Modeling and validation. *Agricultural and forest meteorology*, 148(8-9), 1230-1241.

Xu, H. (2006). Modification of normalised difference water index (NDWI) to enhance open water features in remotely sensed imagery. *International journal of remote sensing*, 27(14), 3025-3033.

Zambrini, R., Martinucci, D. (2018). Sperimentazione con sistemi di telerilevamento multispettrali per il controllo e monitoraggio di argini fluviali. AiPo, Relazione tecnica.

Sitography

<https://3dmetrica.it/>. Last visit 29/01/2019.

<http://www.markelowitz.com/Hyperspectral.html>. Last visit 17-09-2018.

<https://scihub.copernicus.eu/> Last visit 16/02/2019.